CONSTRAINING THE P PROCESS: CROSS SECTION MEASUREMENT OF $^{84}Kr(p,\gamma)^{85}Rb$

By

Alicia R Palmisano

A DISSERTATION

Submitted to
Michigan State University
in partial fulfillment of the requirements
for the degree of

Physics - Doctor of Philosophy

2021

ABSTRACT

CONSTRAINING THE P PROCESS: CROSS SECTION MEASUREMENT OF $^{84}Kr(p,\gamma)^{85}Rb$

By

Alicia R Palmisano

One of the biggest questions in nuclear astrophysics is understanding where the elements come from and how they are made. Everything around us, from our pets to our food to our computers, was made from material originally created in a star. There are so many aspects to consider when trying to answer these questions: "What astrophysical events make what elements?", "How many elements are made?", "How much of each element is made?" and more. The first step in answering these questions is running simulations of these astrophysical events. However, in order to get the correct final abundances of the elements from these events huge amounts of nuclear data is required that has never been measured. This work focuses on the p process and the elements created in this process known as the p nuclei. The p process is responsible for making the stable isotopes on the proton rich side of stability and is thought to occur in core collapse or Type Ia supernova. Currently scientists rely heavily on theory to define parameters in astrophysical and nuclear reaction codes. In addition, experiments are being performed to slowly measure more nuclear data to add constraints to theory for the p process reaction networks.

The focus of this thesis was an experiment that was performed with the Summing Sodium Iodide (NaI) (SuN) detector at the National Superconducting Cyclotron Facility (NSCL) at Michigan State University (MSU) using the ReAccelerator (ReA) facility. A new reaction gas target was designed and fabricated as well as a new analysis technique for background subtraction and efficiency calculations of the detector. The ^{84}Kr(p,γ)^{85}Rb cross section

was measured, which is on a stable isotope important for the astrophysical p process and the production of the p-nucleus, ^{78}Kr. Running with a stable beam was also important for developing the techniques for radioactive beams. In the future, this experimental setup will be used for radioactive beam experiments which are of interest for astrophysics applications. The cross section measurement of the ^{84}Kr(p,γ)^{85}Rb reaction and more details will be discussed.

For my grandma, Flo Baer August 12, 1928 - August 17, 2019, the first female to receive a STEM degree in mathematics in the family in 1950. A wonderful and kind woman who is dearly loved and greatly missed.

ACKNOWLEDGMENTS

I have many people to thank for my achievements throughout my graduate career! First, my undergraduate advisor, Sharon Stephenson, for encouraging me to go to graduate school. Her guidance helped me find a career I didn't even know I wanted yet. Second, my wonderful and supportive graduate advisor, Artemis Spyrou, who has helped me these last few years. She has kept me motivated and provided so many opportunities for me to grow as a scientist and as a person. Thank you so much for helping and believing in me through this process!

Next I want to thank the SuN and Beta groups at the lab! The sense of camaraderie between our groups and its members helped to make all those late nights and long days at the lab an adventure. Everyone was so kind and helpful whenever I had questions and I always felt welcome in any office for work questions, chatting or job advice. Thank you Alex, Mallory, Stephanie, Andrea, Caley, Becky, Katie, Lauren and anyone I have forgotten for being wonderful friends and mentors. I love you all dearly and will miss you so much!

There are many other scientists at the lab that deserve thanks! Big thanks to my committee, Sean Liddick, Vladimir Zelevinsky, Chris Wrede and Steve Zepf for their guidance and direction. A big shoutout to the ReA operators who worked tirelessly during my thesis experiment. John Yurkon and Marco Cortesi for all of their help making the gas cells along with Jorge Pereira and Remco Zegers for the assistance with the gas handling system. I feel like there are more people than this so I apologize if I miss anyone!

My family and friends outside of the lab have been instrumental in helping me. Thanks to my mom and dad for helping and supporting me in my accomplishments and to Matt for keeping me motivated and sane during quarantine! Without you guys none of this would have been possible and I am truly grateful.

TABLE OF CONTENTS

LIST OF TABLES

LIST OF FIGURES

Chapter 1

Introduction

How and where are the elements formed in the universe? The origin of the elements is an evolving and prominent question for the nuclear astrophysics community and is the motivation of this thesis work. It may seem like a simple question but it involves multiple fields and becomes complex quickly. Scientists have a good general picture but there are still many unanswered questions.

Seconds after the Big Bang, all of the hydrogen and helium, and small amounts of lithium, in the universe were created. But then where do all the heavier elements come from? The first step in answering this question is looking closer at stars. They are fascinating objects encompassing numerous types of physics including nuclear physics, fluid dynamics, quantum mechanics, statistical mechanics and more. During star formation, a cloud of gas, or a nebula, will slowly condense into a ball and slowly collapse onto itself until a star is born. Figure 1.1 shows the Butterfly Nebula where one can see the gas from a previous star. After formation, stars will fuse hydrogen together to make helium and other elements up to iron with non-explosive processes. It isn't until its death that the heavy elements, elements heavier than iron, get created and are blown back into the universe. These elements float through the interstellar medium and form new nebulae where the process begins again. Through this cycle, heavier elements are made in stars and ejected back into the stellar medium through star death to make objects on the Earth.

Figure 1.1: The Butterfly Nebula with a wingspan of approximately three light years. [1]

This thesis will focus on the origin of a specific subset of elements known as the p nuclei which will be discussed in great detail in later sections. Where these elements are thought to form and how having accurate nuclear data is very important to calculate the astrophysics observables. The new experimental and analysis techniques developed at the NSCL with this work will help measure cross sections in future radioactive beam experiments. This thesis outlines the direct cross section measurements of the ^{84}Kr(p,γ)^{85}Rb reactions.

1.1 The Elements

Stable elements do not undergo decay whereas the unstable elements will emit particles or *gamma*-rays until they reach a stable state. An element is built up of atoms with each atom having a unique nucleus at the center of a negatively charged electron cloud. The nucleus is much smaller than the total size of the atom and is made up of positively charged protons and neutral neutrons bound tightly together. The number of protons in the nucleus defines the element but each element can have multiple isotopes. There are 118 stable isotopes in the universe that have been observed. An isotope has the same number of protons, so the element remains the same, but the number of neutrons in the nucleus is changing. For example, one proton and one neutron is deuterium and one proton and two neutrons is still hydrogen but also an isotope of hydrogen commonly called tritium. Figure 1.2 shows the Chart of the Nuclei which is a convenient way to organize the known elements and their isotopes. The x axis represents increasing number of neutrons, so each box is a different isotope as you move horizontally, and the y axis represents increasing number of protons, so each row is a different element as you move vertically. Each box represents one of approximate 3,000 stable and radioactive isotopes that have been seen naturally or in the lab [2].

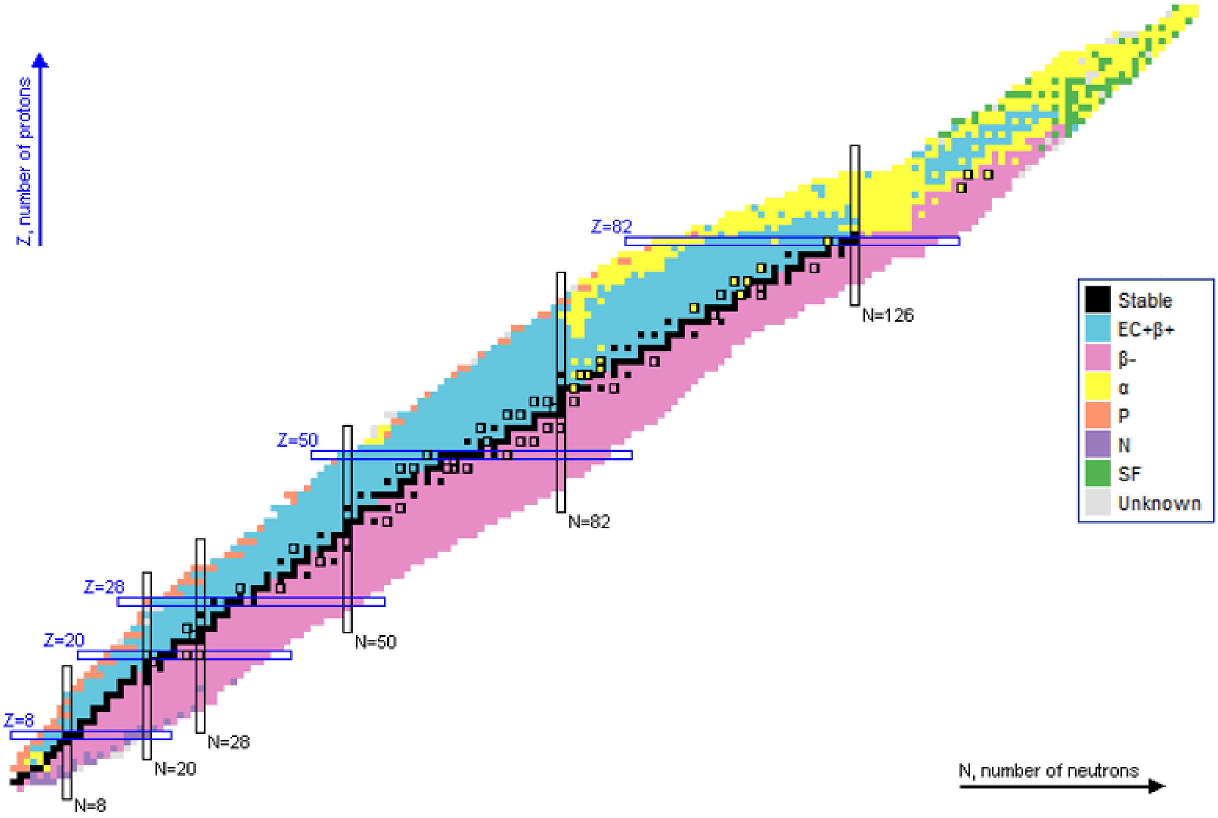

Figure 1.2: Chart of the Nuclei with increasing neutrons on the x axis and increasing protons on the y axis. The black isotopes are stable and the various other colors are decay modes listed in the legend. [3]

The black boxes in Figure 1.2 are the stable isotopes. The other isotopes are radioactive and their colors correspond to their decay mode displayed in the legend. When radioactive isotopes are created they will want to decay towards the valley of stability. For example, if an isotope is created on the neutron rich side of stability it will undergo β^- decay back towards stability.

The dark blue rectangles are proton and neutron "magic" numbers where the nuclear structure makes these isotopes more stable than their neighbors. Therefore, it takes more energy to remove or add protons or neutrons to these nuclei. The magic numbers and their repercussions were theoretically proposed in 1949 and this phenomenon is similar to how electrons fill in orbitals around the nucleus in an atom [4]. Protons and neutrons fill energy shells in the nucleus instead of orbitals like the electrons and these "magic" numbers correspond to closed shells. When the energy shell is completely filled with protons or neutrons it reaches a more stable configuration for a nucleus and is considered a closed shell.

The notation for writing out a specific nucleus is as follows: ${}^{A}_{Z}X_N$ where X is the element, Z is the number of protons, N is the number of neutrons and A is the mass number or Z+N. With this notation we can write deuterium and tritium from the previous example as ${}^{2}_{1}H_1$ and ${}^{3}_{1}H_2$. However, it is more common to drop the neutron and proton number as each isotope can be uniquely labelled with only the element and mass number. Recall that the number of protons is also defined as the element and is thus redundant. Using this notation with the same examples we have hydrogen and tritium written as ${}^{1}H$ and ${}^{3}H$. This notation will be used for the remainder of this work.

1.1.1 Solar System Abundances

The elemental solar system abundances are the relative amounts of each element present in our solar system. These abundances serve as the main astrophysical observable scientists use to compare to theory when running simulations. Measurements of the solar system abundances are taken with two main methods: measuring the solar photosphere and looking at specific types of meteorites [5]. Measuring these abundances gives scientists a metric for our solar system's elemental abundance during its formation as a collapsing nebula as the overall composition has not been drastically altered. The isotopic abundances are calculated from the elemental abundances using the terrestrial isotopic ratios [6]. Figure 1.3 shows the elemental abundances as a function of mass number from the data presented by Lodders [7].

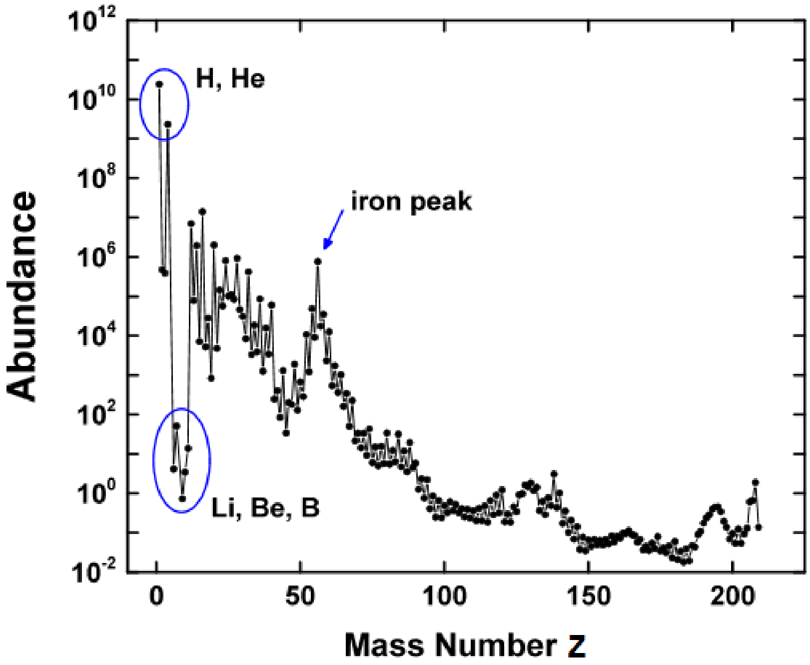

Figure 1.3: The total solar system elemental abundances as a function of mass number normalized to 10^6 Si atoms. Interesting features of the abundance pattern are highlighted in blue and will be discussed. [7]

During the Big Bang hydrogen, helium and some lithium were created and are still the most abundant elements. However, there is a deficit of lithium, beryllium and boron because they are highly reactive elements with large cross sections. These elements are thought to be created through spallation events and interaction with galactic cosmic rays [8]. Moving up in mass, there is a general decrease in abundances until the iron peak. The elements in this mass region are formed through charged particle nuclear reactions in stars and the general decrease in abundance is due to the increasing Coulomb repulsion as the mass increases [5]. The iron peak arises because these elements are the most energetically stable. The elements with masses higher than iron are created in various explosive processes in stars, like neutron capture and γ induced processes, which will be discussed later.

1.2 Nucleosynthesis

Nucleosynthesis is the creation of the elements in the universe. This can happen in multiple different types of astrophysical environments such as star evolution, supernovae, neutron star mergers and more. Some of the founding nuclesynthesis papers were by Burbidge, Burbidge, Fowler, and Hoyle (B2FH) [9] and Cameron [10] in 1957. They stated that heavy element nucleosynthesis occurred in stars as opposed to all the elements being created via Big Bang nucleosynthesis. These publications are still considered to be a solid foundation for stellar nucleosynthesis and have been built upon as the scientific understanding evolves. Since their release, more astrophysical simulations, nuclear data experiments for masses and cross sections, astrophysical observations and galactic chemical evolution simulations are being incorporated to continue our understanding of nucleosynthesis.

Sections 1.2.1 and 1.2.2 will discuss the nuclesynthesis of elements lighter in mass than iron. For elements heavier than iron there are four main processes: the s process, r process, i process and p process which will be discussed in Sections 1.2.3 and 1.3.1. Figure 1.4 shows a cartoon layout of the processes responsible for creating various sections of the Chart of the Nuclei. Stellar burning for masses less than iron and the s process, r process and p process for masses above iron. While this is a simplified picture, as there are other processes that can create these isotopes, this thesis will only discuss these and the i process. Figure 1.5 shows the relative abundances of the s, r and p processes nuclei normalized to 10^6 Si atoms [11]. From Figure 1.5 it is clear that most of the elements are made through the s process and r process. However, even though the p process isotopes are much lower in total abundances, they are still very important and generally cannot be made through the s process, r process or i process.

For a more complete overview of the nucleosynthesis landscape, the rest of this chapter is dedicated to an overview of the processes listed in Figure 1.5 along with some extra processes relevant to this work. This dissertation work is focused on the creation of the p nuclei and Section 1.3 will go into more detail about processes that create these isotopes.

1.2.1 Big Bang Nucleosynthesis

During the Big Bang, there was a massive amount of energy released creating the building blocks for the universe. Some of the original ideas behind Big Bang nucleosynthesis came as early as 1937 by Weizsäcker [12]. He hypothesized that the universe stayed hot after the initial bang and the universe heated all the elements into the abundance patterns we see today. It wasn't until a few years later that Gamow and colleagues introduced the idea of the fast expansion and cooling of the universe after the Big Bang [13]. Once this cooling

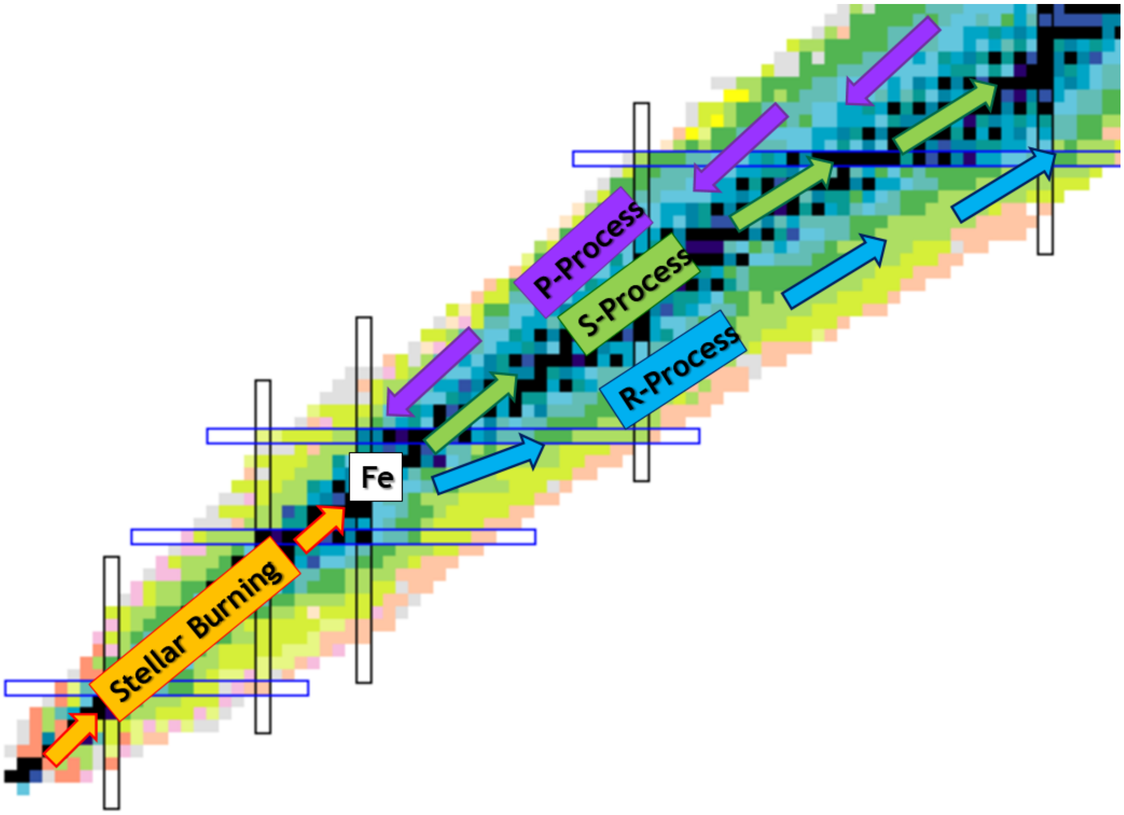

Figure 1.4: Shows the Chart of the Nuclei with increasing neutrons on the x axis and increasing protons on the y axis. Shows what stellar burning creates, where the iron (Fe) peak lies, what elements are made from the s process, r process and p process, and the magic number rectangles.

took place, free protons and neutrons combined making ^1H, ^2H, ^3He and ^4He. These initial abundances are still seen in Figure 1.3. Trace amounts of lithium and beryllium were also made in this process but the majority are thought to be made through spallation reactions in the interstellar medium [5].

However, no heavier mass elements were made during the Big Bang. Since there are no stable isotopes of mass five and eight they proved to be barriers to heavier element creation [14]. Once ^4He was created, if a single proton or neutron was captured the isotope was unstable and would decay back to ^4He. A proton and neutron had to simultaneously capture onto a ^4He to create ^6Li to bridge this gap. This was less probable than capturing

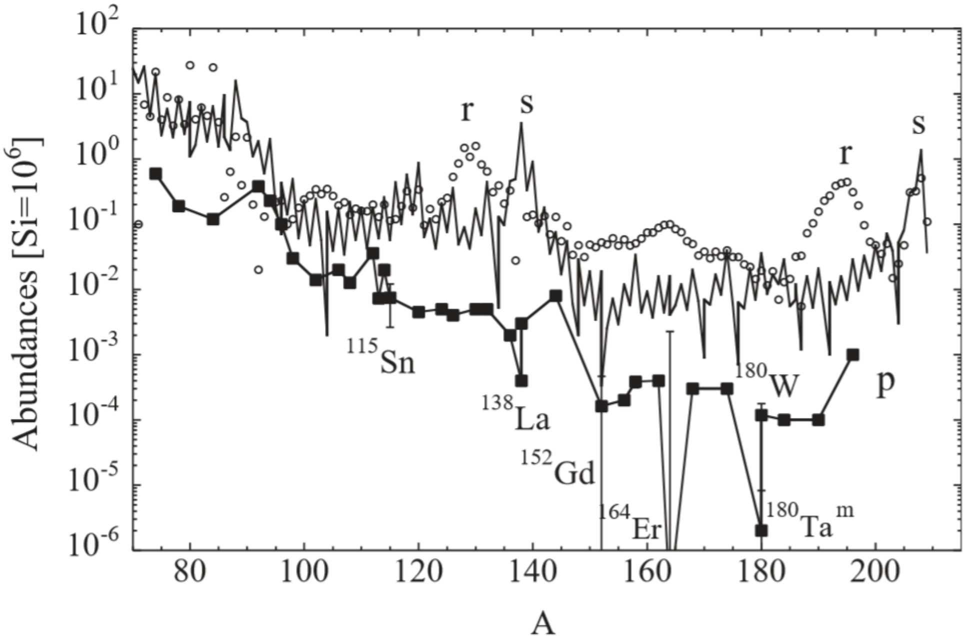

Figure 1.5: This plot shows the relative abundances of the elements from the s process, r process and p process normalized to 10^6 Si atoms. S process is the solid line, r process are the open circles and p process are the filled in squares. [11]

one at a time resulting in less ^6Li from the Big Bang. Similarly, there are no stable isotopes with mass eight making it nearly impossible to create any heavier mass elements. The rest of the elements were therefore made through various other processes that will be discussed in the rest of the chapter.

1.2.2 Stellar Burning

After the Big Bang, millions of years went by while the universe expanded and continued to cool. Clouds of hydrogen and helium gas began to slowly condense into large clumps forming the first nebula. As the gas continued to collapse under its own gravitational force, the temperature and pressure at the center of the cloud became high enough to ignite hydrogen fusion. The gravitational pressure that was collapsing the gas and the energy released from the fusion reactions at the center counteracted each other and formed an equilibrium.

In this way, a star was born with its core stably burning hydrogen into helium. This period in a star's life is called main sequence burning. Stars live most of their lives on the main sequence burning hydrogen as the majority of a star's mass is made of hydrogen.

During the main sequence, hydrogen is fused either with pp chain or CNO cycle burning. Stars with lower initial masses, $M < 1.5M_{\odot}$, will generate energy via the pp chains in the core and stars with larger initial masses, $M > 1.5M_{\odot}$, will undergo the CNO cycle in the core [5]. The three pp chains, or the proton-proton chains, are various reaction chains that convert four protons into one α particle or a ^4He isotope. They all begin with the same two reaction, as other light nuclei reactions are less probable, and end with the creation of an α particle [15]. Heavier mass stars will undergo the CNO cycles instead of the pp chains. These stars will typically contain more nuclei other than hydrogen and helium such as carbon (C), nitrogen (N) and oxygen (O) which are required for the CNO cycles. Like the pp chains these cycles convert four protons into one α particle and have multiple reaction chains that could occur with the same end result [5]. The C, N, and O in these reactions simply act as a mechanism for the burning and are not consumed or created during the processes.

Similarly to how the initial mass of the star dictates which hydrogen burning will occur, the initial mass of the star also decides the star's evolutionary path. Only massive stars, over approximately eleven solar masses, will be able to undergo fusion all the way through silicon burning and hit the iron peak elements. A brief outline of the life cycle of a massive star of $25M_{\odot}$ will follow. First, the star undergoes hydrogen burning on the main sequence converting its hydrogen into helium. Eventually, the star will run out of hydrogen in its core as it is replaced by inert helium. Hydrogen will continue to burn in the outer shell and add mass to the helium core. It takes higher temperatures to ignite helium burning and the core is no longer producing energy through fusion. Therefore, the inert helium core begins to shrink causing the temperature and pressure to increase until the helium ignites. Once helium ignites in the core the star expands as the outer hydrogen layer gets heated and the star becomes a super-giant [16].

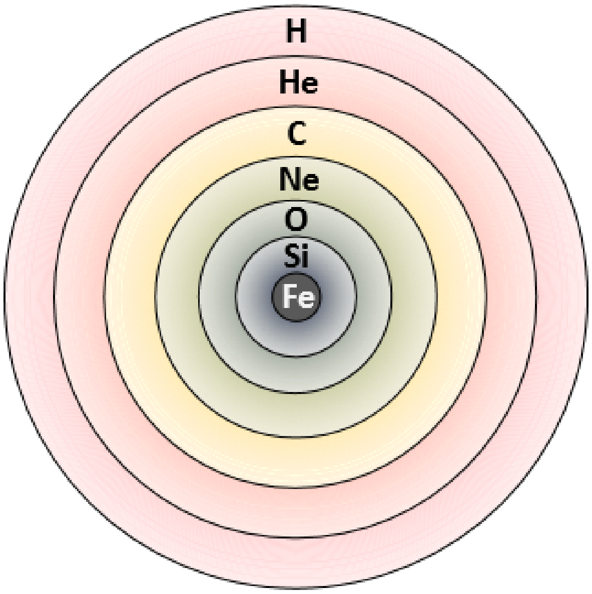

Figure 1.6: Shows the onion-like structure of a $25M_{\odot}$ after undergoing fusion from hydrogen through silicon burning leaving an inert iron core before core collapse [17].

Now the star is fusing helium into carbon in its core and some of the s process elements are synthesized. It will slowly replace its core with inert carbon and create a new layer of helium burning beneath the hydrogen burning. When it runs out of helium in the core it will shrink again until the temperatures are hot enough to ignite carbon burning. This process repeats with carbon burning, neon burning, oxygen burning and silicon burning until the star is left with an onion-like structure as shown in Figure 1.6. However, once the star completes silicon burning it can no longer create enough energy in its core to counteract its gravitational force. Iron burning is no longer energetically favorable; all the previous cycles are exothermic whereas iron burning is endothermic and energy will not be released. Consequently, the stable nuclei in the core at this stage are mostly the iron peak nuclei.

Once a star of this mass ignites silicon burning it is guaranteed to undergo a core collapse supernova; whether or not it leaves behind a black hole or a neutron star is unclear [5]. Core collapse supernovae of this kind are also known as Type II, Ib and Ic supernova with the differing classifications based on their spectral lines. Once the star has the structure shown in Figure 1.6, the iron core will expand until it reaches the Chandrasekhar limit of $1.4M_{\odot}$ at which point the core will collapse as it can no longer counteract its gravity. The core collapses in free fall until the densities reach a nuclear density of $\approx 10^{14} g/cm^3$ at which point the nuclear force begins to act like a spring, storing energy. The nuclear potential stores energy before releasing this energy outward causing the inward falling core to rebound. This creates a shock wave which proceeds back out through the core of the star [16]. It is still unclear how the shock wave is fueled as it moves through the core and through the outer layers of the star but neutrons are thought to fuel the shock wave. When the shock wave passes through the oxygen and neon layer (O/Ne) of the star, it is theorized that the correct temperatures are met for the p process and as the shock wave passes through the deeper layers of the star it is hypothesized that conditions for the r process are also met.

1.2.3 Neutron Capture Processes

This section will go over three different neutron capture processes differentiated by the neutron densities in their astrophysical environment: the s process, r process and i process. The s process is also known as the slow neutron capture process and is responsible for making a large number of the heavy isotopes as shown in Figure 1.5 [18]. The s process occurs during the asymptotic giant branch (AGB) phase of a star's lifetime. While a star undergoes helium and carbon burning there are enough free neutrons created to allow for neutron captures on the stable seed nuclei. The neutron density must be approximately 10^8 neutrons per cm^3 for the s process [16].

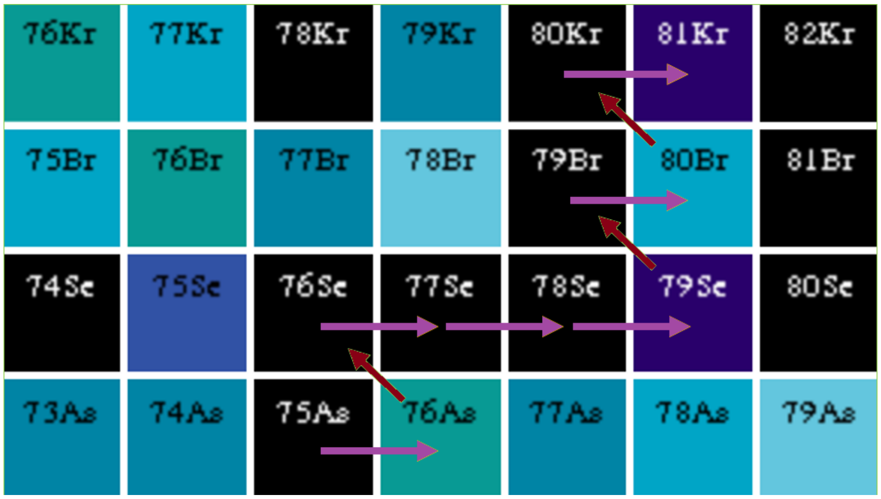

Figure 1.7: Shows an example of an s process path following a series of stable isotopes and undergoing neutron captures. The black isotopes are stable and the other colors are various lifetimes with darker colors having longer lifetimes. The purple arrows are the neutron captures and the red arrows are the beta decays.

Beginning with stable seed nuclei already present in the star, neutrons will capture on a stable isotope through a series of (n, γ) reactions. This notation means the initial isotope is capturing a neutron and the resulting isotope is giving off a gamma ray. This can also be written with the isotopes for specific reactions, for example the reaction on the bottom in Figure 1.7: $^{75}\mathrm{As}(n, \gamma)^{76}\mathrm{As}$. The yellow arrows in Figure 1.7 represent the (n, γ) reactions and the green arrows represent the beta decays. For the s process, there is a balance between the cross section of the neutron capture and the β decay lifetime. The cross section referring to how probable it is to capture a neutron and the lifetime referring to how long it takes the unstable nucleus to decay. The s process generally moves along the stable isotopes as shown in Figure 1.7 and isotopes like ^{80}Se will be produced instead by the r process.

The r process is the rapid neutron capture process [19]. Similar to the s process, isotopes undergo a series of (n, γ) reactions before β decaying back to stability. However, unlike the

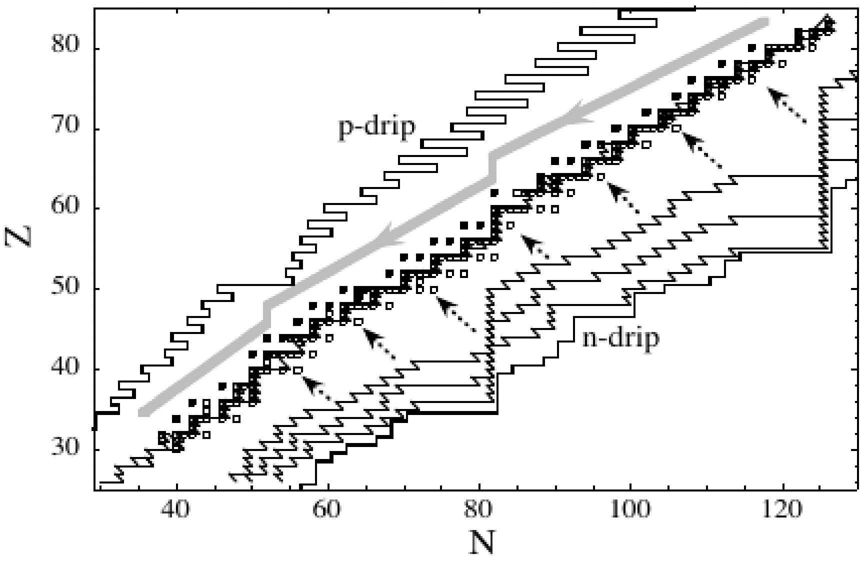

Figure 1.8: The Chart of the Nuclei showing example s process, r process and p process paths. The thicker light grey shows the p process, the black lines along stability show the s process and the lines coming from the neutron drip line show the r process. [19]

s process, the neutron fluxes for the r process are much higher, approximately 10^{21} neutrons per cm^3 [5]. With such a high neutron flux, neutron rich isotopes along the elemental chain are made before undergoing beta decays. Figure 1.8 shows the pathways of the s process, r process and p process from M. Arnould et. al. [19]. The light grey downward arrow shows the pathway of the p process, the black line shows the s process path and the arrows pointing down from the neutron rich side show the r process decays. The r process is thought to occur in core collapse supernova and/or neutron star mergers. Recently a neutron star merger was observed where r process signatures were detected [20]. This is an exciting confirmation that neutron star mergers are an r process site.

The i process is the intermediate neutron capture process [21]. Again this process is a series of (n, γ) reactions with a different neutron density. This process is thought to occur in stars when there is mixing between the hydrogen and helium burning layers. With sufficient mixing there are neutron densities of approximately 10^{16} neutrons per cm^3. There have been astrophysical observations that could not be explained by a combination of s process and r process which indicated a need for a new neutron capture process.

The s process, r process and i process are all a series of (n, γ) reactions. However there are a handful of nuclei that are shielded by the valley of stability on the proton rich side that cannot be made through neutron capture reactions. Figure 1.7 shows two examples ^{74}Se and ^{78}Kr. These two nuclei are a subset of nuclei known as the p nuclei which will be discussed in the next section.

1.3 p Nuclei

The p nuclei are a series of nuclei that cannot be made through neutron capture processes like the s process and r process. There are 35 p nuclei on the proton rich side of the valley of stability that range in mass from ^{74}Se to ^{196}Hg as shown in Figure 1.9. They are approximately 100 times less abundant than the s-process and r-process elements except for molybdenum (Mo) and rubidium (Ru) [5]. Trying to figure out where the p nuclei are made has been an ongoing challenge in the nuclear astrophysics field and is still not well understood. The two prevalent sites are Type Ia supernova [22] and Type II core collapse supernova in the O/Ne layer [23] [24]. Core collapse supernova were discussed in Section 1.2.2. Once a star has an inert iron core, the core will collapse from its own gravitational force. It then emits a shock wave out from the core and through the layers of the star. When this shock wave passes the O/Ne layer, the correct temperatures are met for the p process to tale place. Type Ia supernova are in binary systems with a white dwarf and a companion star accreting mass on to the white dwarf. Once the white dwarf gains enough mass to ignite a thermonuclear runaway and explodes.

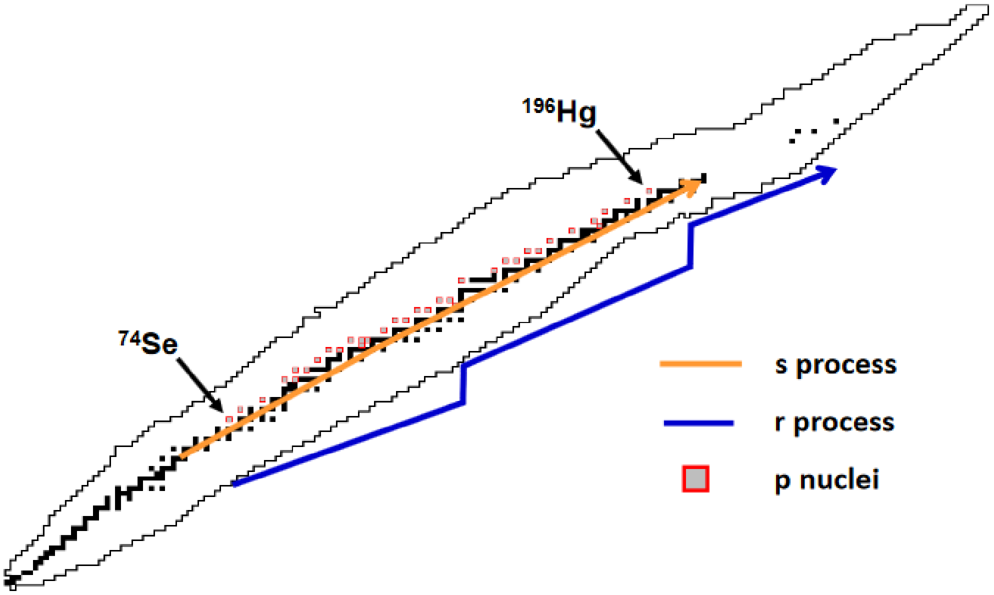

Figure 1.9: The p nuclei are shown in the red boxes on the proton rich side of stability. Also shown is the s process and r process paths. [17]

1.3.1 p Process

The p process was originally believed to be the fast proton capture process [9] and was later determined to be a series of photodisintegration reactions. Sometimes the p process is also referred to as the γ process as it involves a series of (γ, n), (γ, p) and (γ, α) reactions on the s-process seed nuclei. Figure 1.10 shows an example of different reactions that could appear in a p-process reaction network. The red boxes are p nuclei, the green arrows are (γ, n) and (n, γ) reactions, the yellow arrows are (γ, p) reactions and the purple arrows are (γ, α) reactions. The dominant reaction flow for the more neutron rich nuclei during these photodisintegration reactions are (γ, n) reactions. For example, in Figure 1.10 starting from ^{84}Sr the reactions travel to the left through (γ, n) reactions. Eventually the flow reaches branching points where certain isotopes will have other competing reactions, either (γ, p) or (γ, α).

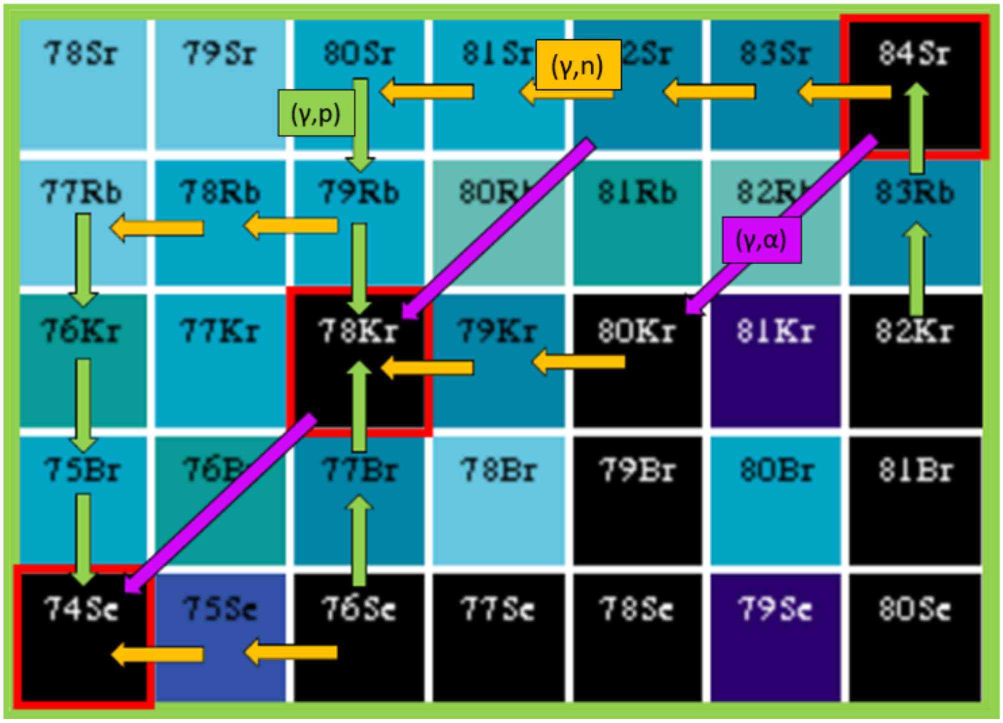

Figure 1.10: Examples for the p process reaction network with a series of (γ, n), (γ, p) and (γ, α) reactions. The red boxes are the p nuclei.

The p process is highly dependent on the temperature of the stellar environment and only occurs in a given temperature range [5]. If the temperatures are too high in the environment the nuclei burn up through photodisintegrations back to the iron peak and if they are too low the photodisintegrations will not occur. The temperatures will be discussed in more detail later in this chapter.

1.3.2 Uncertainties

In order to see where the elements are made, scientists run simulations and compare those outputs to the observed abundances. Running these simulations is a complicated multi step process. First, astrophysics simulations are run to simulate whatever environment is being considered. Second, these outputs are run through post processing codes that take nuclear data into account such as reaction cross sections, decay properties and masses. Finally, to test the validity of these simulations the outputs are compared to the elemental or isotopic solar system abundances. Improving the accuracy of the simulations involves developing the theory (both astrophysics and nuclear) and performing measurements which are used in the simulations. Each portion of the simulation process holds uncertainty: astrophysical sites and theory, nuclear theory and nuclear data. There are numerous astrophysical uncertainties including s-process seed abundances, initial star mass and metallicity, and temperatures. These p-process reaction networks are very complex requiring approximately 2000 nuclei and 20,000 reactions all of which require nuclear data [11]. Constraining the nuclear data through experimental measurements is the best way to help constrain these theories and reduce the overall uncertainty in these calculations.

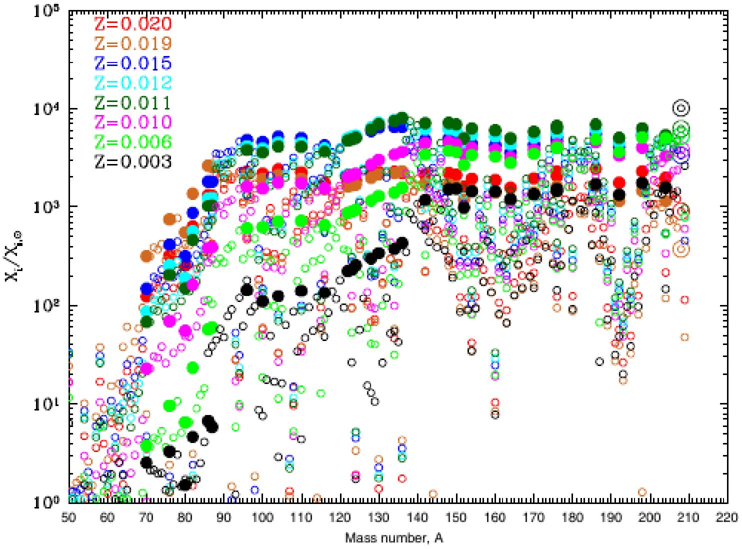

Figure 1.11: Figure from Ref. [25] showing the s seed nuclei abundances after helium burning from varying the initial metallicity of the star from Z = 0.003 to 0.01. The solid dots are nuclei made only from the s process.

1.3.2.1 s-process Seeds

Before the p-nuclei abundances can be calculated, the s-seed nuclei abundances need to be calculated. Correct calculations rely on galactic chemical evolution calculations, astrophysics simulations and nuclear data inputs all of which carry uncertainties. Figure 1.11 shows an example of uncertainties from the s-seed nuclei at the end of helium burning when varying the initial metallicity of the star [25]. The metallicity is how many heavier elements, such as C, O, N, are present in the initial composition of the star. There is up to two orders of magnitude uncertainty in the s-seed abundances when varying the metallicities. Since the p-process abundances begun with the s-process seed nuclei abundances, this large variance will carry through the simulations to the p nuclei.

1.3.2.2 Initial Masses

Varying the initial mass of the star in astrophysical simulations also carries uncertainties. Figure 1.12 shows the normalized over production factors for the p nuclei post a supernova explosion with various initial solar masses [26]. If the points land on the centered dashed line labelled one the simulation would be creating the correct amount of each element. Anything above is over produced and anything below is under produced. The uncertainties from the initial mass are slightly smaller than the uncertainties seen from varying the metallicities and the s-process seed abundances. Most of these isotopes vary within an order of magnitude whereas the s-process seed abundances carried closer to two orders of magnitude uncertainties.

1.3.2.3 Temperature and Density Profiles

Along with uncertainties in the s seed nuclei there are uncertainties in the temperature and density profiles of the stars during supernova which will greatly affect the final abundances of the p nuclei. As mentioned previously, the photodisintegrations rates are highly temperature dependent and as the temperature of the layer changes, the final abundances

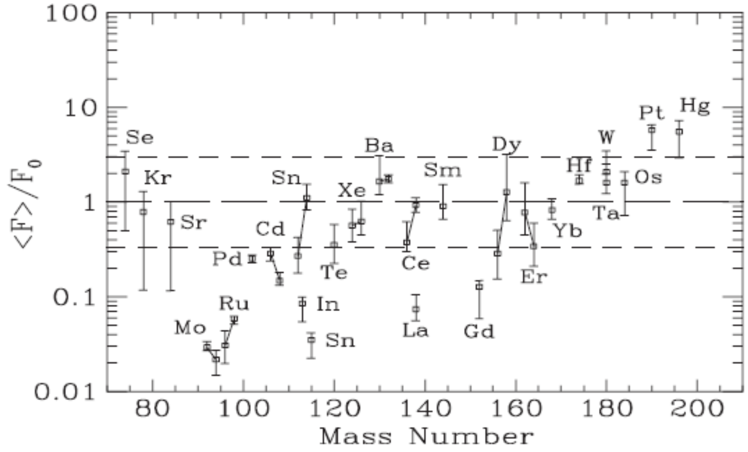

Figure 1.12: Figure from Ref [26] showing the overproduction factor for the p-nuclei in a supernova explosion calculation of a 13-25 $M_{\odot}$ star. The error bars refer to the same calculations done with various initial solar masses.

change drastically. Figure 1.13 shows this clearly with the overproduction factors of selected p nuclei as a function of maximum temperature in the O/Ne layer of the star. For example, looking at ^{184}Os shows the final abundance can change by a factor of 100 by varying the peak temperature by only 0.2GK. This is the same order of magnitude in uncertainty as varying the initial s-seed abundances and the metallicites. The observed solar abundances are a mixture of stars with various initial masses, metalicities and temperature-density profiles which all produce different p nuclei abundances. In order to match the solar abundances there needs to be the correct combination for all these astrophysical properties which currently have uncertainties up to a factor of 100 in magnitude.

1.3.2.4 Reaction Rates

The previous sections discussed the astrophysical uncertainties but there are still uncertainties in the nuclear data which also change the final abundances of the p nuclei. The experimental measurement performed in this thesis can help constrain the nuclear theory uncertainties in the reaction rates. Most of the 20,000 reactions in the p process reaction

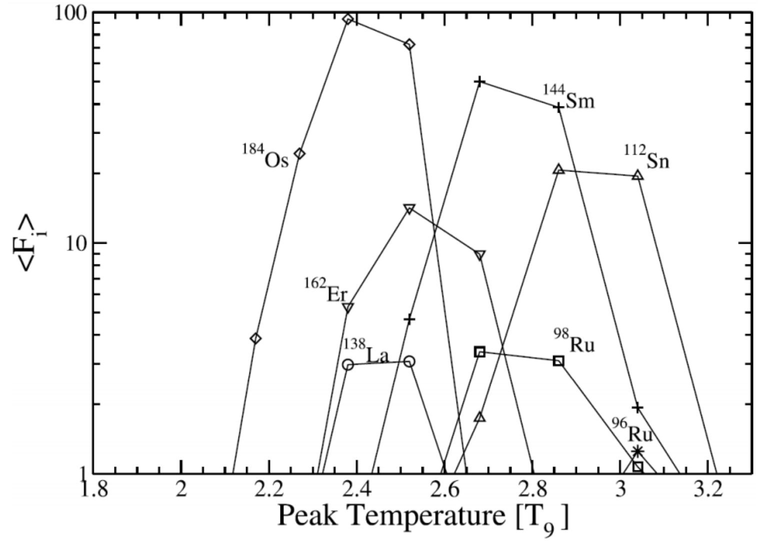

Figure 1.13: Figure from Ref. [27] showing the overproduction factor of selected p nuclei with varying temperatures in the O/Ne layer during a supernova.

networks are on radioactive isotopes which rely heavily on theory and have no experimental constraints. Figure 1.14 shows how varying the reaction rates up and down by a factor of 3 for the (a) (p, γ) and (γ, p) reactions and the (b) (α, γ) and (γ, α) reactions affects the final p nuclei abundances [27]. The (p, γ) reaction variations predominantly change the abundances of the lighter mass p nuclei and the (α, γ) reactions variations change the heavier mass p nuclei.

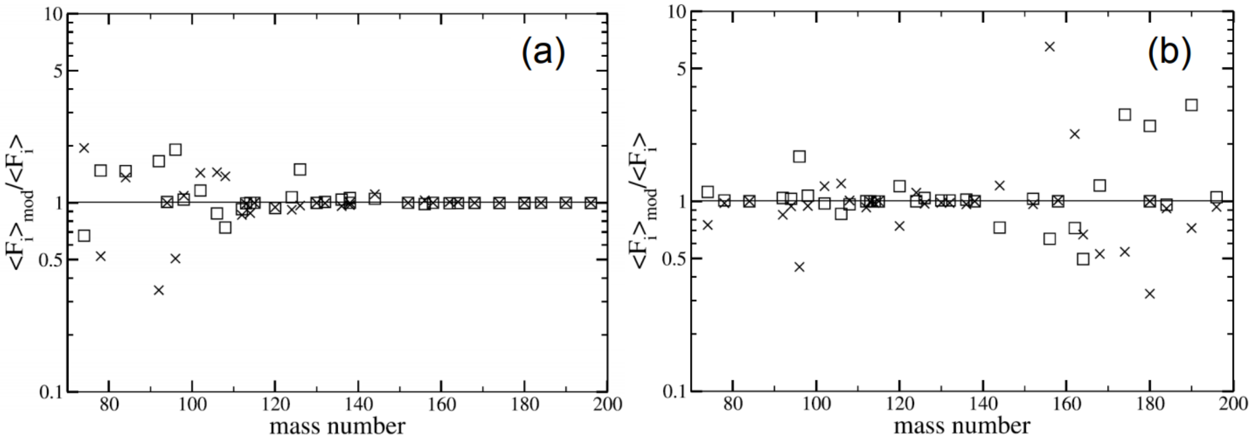

Figure 1.14: Figure from Ref. [27] showing the over production factors when varying the reactions rates by a factor of three up and down for (a) (p, γ) and (γ, p) reactions and (b) (α, γ) and (γ, α) reactions.

The variations in final abundances due solely to the nuclear reaction rates is much smaller than the average uncertainties due to the astrophysical inputs. However, it is still important to lower these uncertainties which are still up to a factor of 5 in magnitude. The future of the experimental nuclear astrophysics field for the p process is to help set experimental constraints on these reaction rates to reduce the uncertainties in the models. This work focuses on developing and validating an experimental and analysis technique which can be used in future radioactive experiments to measure more of these relevant reaction rates. Even the measurement made on the stable ^{82,84}Kr nuclei can help to constrain these theoretical uncertainties.

1.3.2.5 Sensitivity Studies

Because these p-process reaction networks are so large it is impossible to measure everything experimentally. In order to choose the most important nuclei to measure sensitivity studies are performed to identify which reactions vary the final abundances the most when altered.

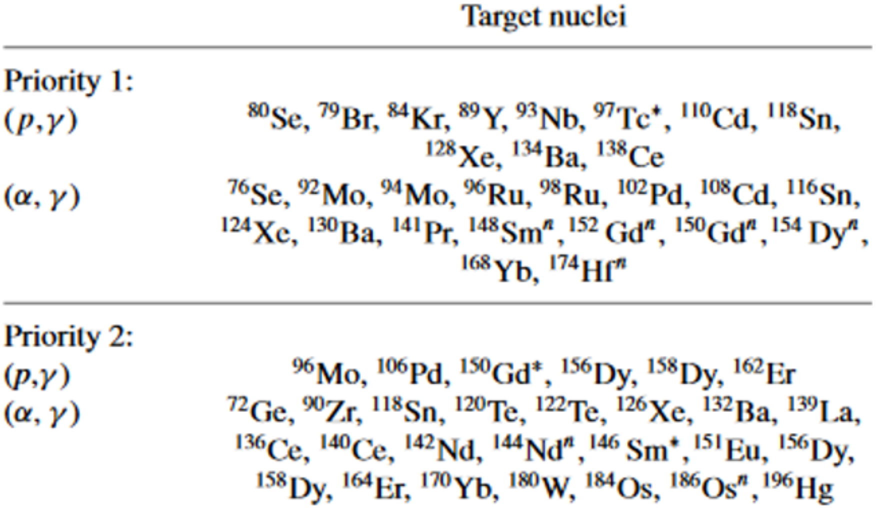

	Target nuclei
Priority 1:	
(p,γ)	^{80}Se, ^{79}Br, ^{84}Kr, ^{89}Y, ^{93}Nb, ^{97}Tc*, ^{110}Cd, ^{118}Sn, ^{128}Xe, ^{134}Ba, ^{138}Ce
(α,γ)	^{76}Se, ^{92}Mo, ^{94}Mo, ^{96}Ru, ^{98}Ru, ^{102}Pd, ^{108}Cd, ^{116}Sn, ^{124}Xe, ^{130}Ba, ^{141}Pr, ^{148}Sm^{n}, ^{152}Gd^{n}, ^{150}Gd^{n}, ^{154}Dy^{n}, ^{168}Yb, ^{174}Hf^{n}
Priority 2:	
(p,γ)	^{96}Mo, ^{106}Pd, ^{150}Gd*, ^{156}Dy, ^{158}Dy, ^{162}Er
(α,γ)	^{72}Ge, ^{90}Zr, ^{118}Sn, ^{120}Te, ^{122}Te, ^{126}Xe, ^{132}Ba, ^{139}La, ^{136}Ce, ^{140}Ce, ^{142}Nd, ^{144}Nd^{n}, ^{146}Sm*, ^{151}Eu, ^{156}Dy, ^{158}Dy, ^{164}Er, ^{170}Yb, ^{180}W, ^{184}Os, ^{186}Os^{n}, ^{196}Hg

Figure 1.15: Figure from Ref. [28] showing key branching point nuclei from a model independent sensitivity study performed by Rauscher.

In Figure 1.15 there are two sets of isotopes, priority 1 and 2, listed that have been highlighted in a model independent sensitivity study. They are important branching point nuclei that can vary the reaction flow within the p-process reaction network. Priority 1 reactions are sensitive branching points and priority 2 could become new branching points in their rate is measured higher than its current theoretically accepted value [28]. The ^{84}Kr(p, γ) reaction is listed as a priority 1 and therefore is a branching point between the dominant (n, γ) and (p, γ) reaction flow. This reaction was chosen for its importance in determining the reaction flow of the p process in this region. If the measured value for the cross section is lower than the accepted theoretical value, the reaction network will favor the (n, γ) reaction and if it is higher it will favor the (p, γ) reaction.

Chapter 2

Theoretical Considerations

2.1 Nuclear Properties

One of the most fundamental quantities of a nucleus is its mass. However, early measurements of the total mass of a nucleus showed it is not simply the sum of its parts and is instead less [29]. The mass of a nucleus can then be written as

$$m_{nuc} = Zm_p + Nm_n - \Delta m \tag{2.1}$$

where m_{nuc} is the mass of the nucleus, m_p is the proton mass, m_n is the neutron mass and Δm is the missing mass. The missing mass, or mass defect, can be written as an energy which was originally proposed by Einstein [30]. This energy corresponds to the amount of energy required to break the nucleus into free nucleons or the amount of energy released when the given nucleus is assembled. This energy is also known as the binding energy and can be written as

$$B.E. = (Zm_p + Nm_n - m_{nuc})c^2 \tag{2.2}$$

where the notation follows Equation 2.1 and c is the speed of light.

Shown in Figure 2.2 is the binding energy per nucleon as a function of mass [5]. The general trend of (a) has an exponential increase in binding energies until it peaks in the iron

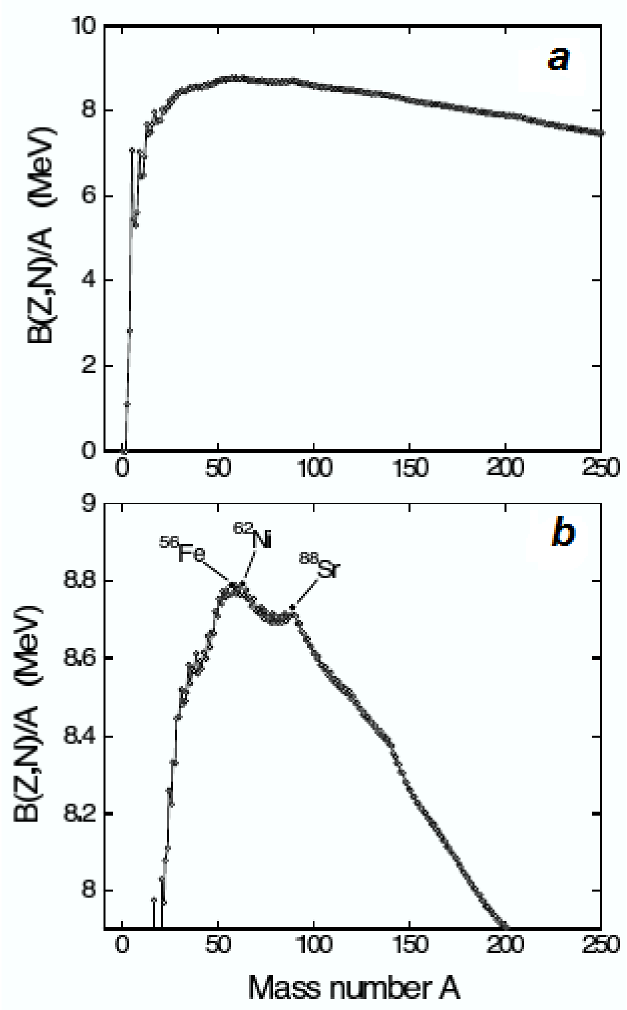

Figure 2.1: (a) Shows the binding energy per nucleon as a function of mass taken from Illiadis with data from the Atomic Mass Evaluation [5] [31]. (b) Zooms into the iron peak region and shows the isotopes with the largest binding energies per nucleon: ^{62}Ni, ^{58}Fe and ^{56}Fe.

region and then slowly decreases again. Most binding energies are around 7-9 MeV/u. Part (b) zooms into the peak shown in part (a) showing the most tightly bound nuclei ^{62}Ni, ^{58}Fe and ^{56}Fe that have binding energies around 8.7 MeV/u [31]. The binding energies of the nuclei both heavier and lighter in mass are all lower and they are less tightly bound.

The trend shown in part (a) of Figure 2.2 also helps to explain the nucleosynthesis landscape. Nuclear energy is released when the reacting nuclei have a lower binding energy than the products of a reaction. Therefore for a star to generate energy it can either undergo fusion until reaching the iron peak or undergo fission past the iron peak, although the later is not generally applicable.

The energetics of a nuclear reaction can also be quantified from the masses of the nuclei in the reaction. For a nuclear reaction written as A + a = B + b and because mass and energy are related, the energy difference, or Q value, of this reaction can be written as

$$Q = (m_{initial} - m_{final})c^2 = (m_A + m_a)c^2 - (m_B + m_b)c^2 \tag{2.3}$$

where m is the corresponding mass of each reactant. Reactions with positive Q values are exothermic and release energy and reactions with negative Q values are endothermic and require energy.

2.2 Cross Sections

This thesis is a direct measurement of a reaction cross section for two different reactions at different energies. A cross section can be thought of as the probability of a reaction taking place. To approach this concept, consider a game of archery where arrows are shot at a target that looks like Figure 2.2. Points are only awarded if an arrow lands within one of the smaller circles labeled "50 points". Assuming the arrow always lands within the larger circle, the probability of hitting an inner circle and getting points is a ratio of the areas.

If the total area of the circle is A and the area of the smaller circles is A_{50} then the probability to hit a 50 point circle is

$$P_{50} = \frac{N_{50}A_{50}}{A} = \frac{N_{50}\pi r^2}{A} = \frac{N_{50}\sigma}{A} \tag{2.4}$$

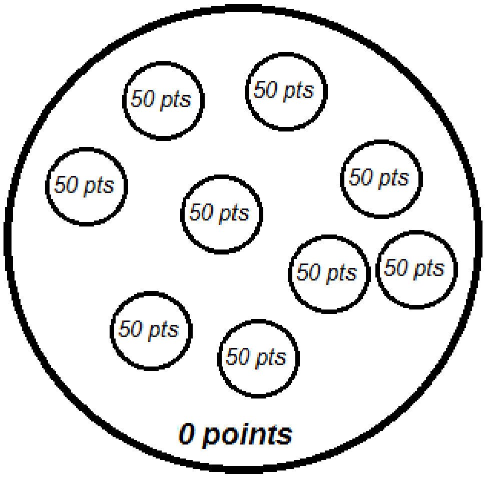

Figure 2.2: A cartoon view of an archery target where points are only awarded if a smaller 50 point circle is hit synonymous to target nuclei with incoming beam particles.

where N_{50} is the number of smaller 50 point circles, r is the radius of the 50 point circles and σ is the cross-sectional area of the 50 point circles. Notice that the cross section, σ, has units of area. If a large number of arrows, N_a, are shot then the number of times a 50 point circle, N_c, is hit can be written as

$$N_c = N_a P_{50} = N_a \frac{N_{50}\sigma}{A}. \tag{2.5}$$

Now we can rearrange and solve for σ to find the cross section of the 50 point circles from the example by writing

$$\sigma = \frac{N_c}{N_a(N_{50}/A)}. \tag{2.6}$$

The (N_{50}/A) term is left in this notation because it is the areal density of the 50 point circles. If the terms from Equation 2.6 are now written in relevant physics terms we have

$$\sigma = \frac{N_c}{N_a(N_{50}/A)} = \frac{N_{reactions}}{N_{beam}(N_{targets}/A)} = \frac{(I/\epsilon)}{N_{beam}(N_A\xi/m_t)} \tag{2.7}$$

where I is the number of recorded events, in this case successfully hitting a 50 point circle, ϵ is the detection efficiency, N_{beam} is the number of beam particles, N_A is Avogadro's number, ξ is the target thickness in units of g/cm^2 and m_t is the target mass. Equation 2.7 is how the cross section will be calculated for the entirety of this thesis.

The substitutions were made so it is easy to track which physical aspects relate to $N_{reactions}$, N_{beam} and $(N_{targets}/A)$. For instance, the I/ϵ term corresponds to $N_{reactions}$ and the $(N_A\xi/m_t)$ term corresponds to $(N_{targets}/A)$. The number of good events seen in a detector corrected for its efficiency will give the final number of times the reaction occurred in the target. The target's areal density will then be given by the target thickness. In order to accurately measure a cross section of a reaction the incoming beam particles, number of reactions within the detector, the target thickness and the detector efficiency must be accurately measured throughout the entire experiment.

It is important to note that the cross section is directly related to a probability but has units of area. In the above example the cross section of hitting one 50 point circle is the area of a single 50 point circle from Figure 2.2. In a nuclear physics experiment that is equivalent to the area of a target nucleus which is on the order of $10^{-24}cm^2$. This value has also been defined as 1 barn or 1 b. The cross sections in this thesis work are even smaller on the order of 1 mb or $10^{-3}b$.

The above approach is still using a classical foundation and there are quantum mechanical effects to be considered. The substitution of $\sigma = \pi r^2$ is a classical substitution. To take quantum mechanics into consideration the more appropriate substitution is

$$\sigma \approx \pi\lambda^2 = \pi\frac{\hbar^2}{2\mu E} \tag{2.8}$$

where λ is the reduced de Broglie wavelength, $\hbar$ is the reduced Planck constant, μ is the reduced mass, and E is the center of mass energy of the beam and target system. The inverse energy dependence is one of the reasons that astrophysically relevant cross section measurements are difficult to measure as the relevant energies are very low. The cross section expression used in this work is

$$\sigma = \frac{A}{N\xi}\frac{1}{N_b}\frac{I}{\epsilon} \tag{2.9}$$

where A is the target mass, N is Avogadro's number, ξ is the target thickness, N_b are the beam particles, I is the number of times the reaction occurs and ϵ is the detector efficiency.

2.3 Stellar Reaction Rates

In order for a star to generate energy there always needs to be a positive amount of nuclear energy released from a reaction. Therefore, knowing the rate of nuclear reactions is imperative for understanding the energy and element generation within a star. For each reaction it is important to know how much nuclear energy is liberated within a stellar volume. This depends on the nuclear cross section of the particles, the velocity distribution of the particles within the stellar plasma and the abundance of each type of interacting particle. Beginning from Equation 2.5 denoting the number of successful attempts to hit a 50 pt circle, the reaction rate per unit volume per time, $\frac{N_R}{Vt}$, can then be written as

$$N_R = N_1\frac{N_2}{A}\sigma \longrightarrow \frac{N_R}{Vt} = \sigma\frac{N_1}{V}\frac{N_2}{Ax}\frac{x}{t} \tag{2.10}$$

where N_1/V and N_2/Ax are the number densities of the interacting particles and x/t represents the relative velocity [5]. The right side of the equation has been multiplied by 1 in the form of $\frac{x}{x}$ to get the velocity and second number density. The number densities can be rewritten as $\frac{N_i}{V_i} = n_i$. Looking back to the previous section, the cross section is also energy dependent. Since the reaction rate is already dependent on velocity the cross section can be written as a function of velocity. Taking all this into account the reaction rate from Equation 2.10 can then be written as

$$r_{12} = n_1 n_2 \sigma(v) v. \tag{2.11}$$

In a stellar environment the relative velocities between the particles are not always the same. Instead they have a velocity distribution defined as a probability function, $P(v)$ where $\int_0^\infty P(v) dv = 1$. Now adding this expression into Equation 2.11 we get

$$r_{12} = \frac{n_1 n_2}{1 + \delta_{12}} \int_0^\infty P(v) \sigma(v) v dv \tag{2.12}$$

where δ_{12} is the Kronecker delta. In a reaction between the same nuclei it is 0 and for a reaction between different nuclei it is 1. Equation 2.12 can be further reduced to the reaction rate per pair, $\langle \sigma v \rangle$, written as

$$\langle \sigma v \rangle = \int_0^\infty P(v) \sigma(v) v dv. \tag{2.13}$$

Now we need an expression for the relative velocities of the particles within the stellar plasma. Nuclei in a stellar environment are nonrelativistic and nondegenerate particles. Therefore the velocities can be written with the Maxwell-Boltzmann distribution seen below where k is the Boltzmann constant and T is the temperature of the stellar plasma.

$$P(v) = 4\pi v^2 \left(\frac{\mu}{2\pi k T} \right)^{3/2} e^{\frac{-\mu v^2}{2kT}} \tag{2.14}$$

With the substitution $E = \mu v^2/2$ and $dE/dv = \mu v$ to perform a change of variables from velocity to energy and adding the Maxwell-Boltzmann distribution into Equations 2.13, we can write the reaction rate per particle pair as a function of energy as;

$$\langle \sigma v \rangle = \sqrt{\frac{8}{\pi\mu(kT)^3}} \int_0^\infty E\sigma(E)e^{-E/kT}dE. \tag{2.15}$$

2.4 Gamow Window

For a specific astrophysical temperature it is possible to calculate the energy with the highest importance for these reaction rates. This energy range is called the Gamow peak which appears within the integral of the reaction rate given in Equation 2.15. This Gamow peak arises from the competition between the Gamow factor introduced in Equation 2.23 and the Maxwell-Boltzmann distribution used in Equation 2.15. For a specific temperature in the stellar environment, there is a corresponding energy range where the reactions can occur. Plugging the cross section written in terms of the astrophysical S factor, Equation 2.23, into the reaction rate per particle pair in Equation 2.15 we can write the reaction rate as

$$\langle \sigma v \rangle = \sqrt{\frac{8}{\pi\mu(kT)^3}} \int_0^\infty e^{-2\pi\eta}e^{-E/kT}S(E)dE \tag{2.16}$$

where T is the temperature, E is the energy, and $\eta = Z_1Z_2e^2/\hbar v$ and is also called the Sommerfeld parameter. Using the velocity and energy relation, $E = \mu v^2/2$, rewriting the Sommerfeld parameter as a function of energy and some algebra we get

$$\langle \sigma v \rangle = \sqrt{\frac{8}{\pi\mu(kT)^3}} \int_0^\infty e^{\frac{Z_1Z_2e^2\pi}{\hbar}\left(\sqrt{\frac{2\mu}{E}}\right)}e^{-E/kT}S(E)dE \tag{2.17}$$

where Z_i are the charges of the interacting particles and μ is the reduced mass in atomic mass units. This can be further simplified by introducing a constant term, $E_G = \frac{\pi}{\hbar} Z_1 Z_2 e^2 \sqrt{2\mu}$. Inserting this into Eq. 2.17 it becomes easier to see the competing energy dependencies for the Maxwell and Coulomb terms. With this substitution we have

$$\langle \sigma v \rangle = \sqrt{\frac{8}{\pi \mu (kT)^3}} \int_0^\infty e^{-\left(\sqrt{\frac{E_G}{E}}\right)} e^{-E/kT} S(E) dE. \tag{2.18}$$

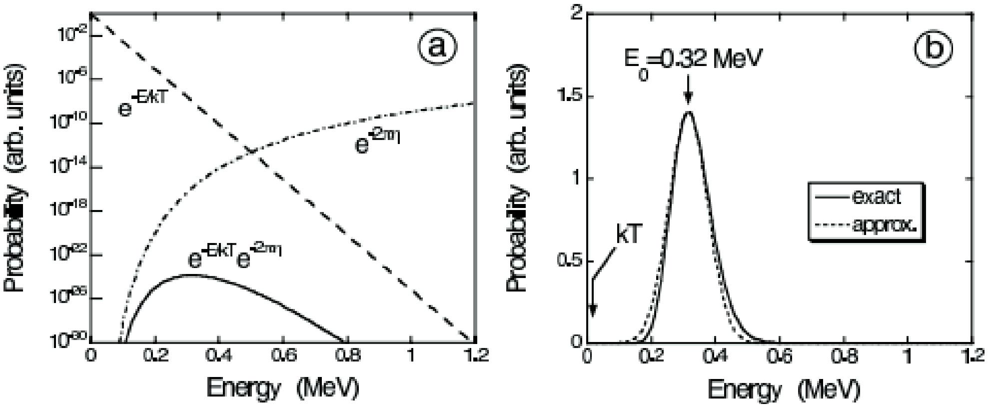

Figure 2.3: Figure taken from Illiadis [5]. (a) shows the Maxwell-Boltzmann distribution, dashed line, and the Gamow factor, dotted-dashed line and their product in a solid line. (b) shows the same Gamow peak for the $^{12}C(\alpha,\gamma)^{16}O$ reaction in a linear scale.

The Gamow factor term will go to zero as the energy goes to zero whereas the Maxwell-Boltzmann factor goes to zero as the energy increases. While the integral depends on the astrophysical S factor, it has a small effect on the peak location as it has a weak energy dependence. Both terms are drawn in Figure 2.3 taken from Illiadis [5]. Part (a) shows the Maxwell-Boltzmann distribution (dashed line), the Gamow factor (dotted-dashed line), and their product (solid line) for the $^{12}C(\alpha,\gamma)^{16}O$ reaction. The product is the known as the Gamow peak. Part (b) of Figure 2.3 also shows the Gamow peak on a linear scale with the dotted line showing a Gaussian approximation. The Gamow peak is an energy range for specific stellar temperatures, also known as the Gamow window, where the majority of nuclear reactions are taking place in a stellar environment. For measurements to be relevant for astrophysics the experimental energies must be within this energy window.

The peak energy will differ for each reaction and can be solved by taking the derivative of the integrand of Equation 2.17 and setting it to zero. Because S(E) is a smooth varying function with respect to energy, it is approximated as a constant and removed from the integral. Taking the derivative gives the Gamow peak energy as

$$E_{peak} = \left(\frac{E_G kT}{2}\right)^{2/3} \tag{2.19}$$

with a width of

$$\Delta E = 4\sqrt{\frac{E_{peak} kT}{3}}. \tag{2.20}$$

Peak Energy (MeV)	Energy Width (MeV)	Energy Range (MeV)	Temperature (GK)
0.745	0.827	0.331 - 1.159	2
0.864	0.997	0.366 - 1.363	2.5
0.976	1.160	0.396 - 1.556	3
1.082	1.319	0.422 - 1.741	3.5

Table 2.1: Shows the various calculated Gamow energies and their widths at different temperatures for the $^{16}O(p,\gamma)^{17}F$ reaction shown in Figure 2.23 [5].

Peak Energy (MeV)	Energy Width (MeV)	Energy Range (MeV)	Temperature (GK)
2.103	1.390	1.408 - 2.798	2
2.440	1.675	1.603 - 3.278	2.5
2.756	1.949	1.781 - 3.731	3
3.054	2.217	1.946 - 4.162	3.5

Table 2.2: Shows the various calculated Gamow energies and their widths at different temperatures for the $^{84}Kr(p,\gamma)^{85}Rb$ reaction.

Tables 2.1 and 2.2 show the peak energy, E_{peak}, the energy width and the corresponding energy ranges for the $^{16}O(p,\gamma)^{17}F$ and $^{84}Kr(p,\gamma)^{85}Rb$ reactions at various temperatures. Notice that both the peak energy and the width are dependent on the particle charges and the stellar temperature. For higher charges and higher temperatures the Gamow peak is shifted higher in energy which can be seen in Tables 2.1 and 2.2. The lower charge nucleus, Oxygen, has a lower Gamow window then the higher charged nucleus, Krypton, whose peak energies are almost 1.5 MeV higher in energy. The experimental work in this thesis was run at such low energies to ensure the measurements were astrophysically relevant within the Gamow window for the $^{84}Kr(p,\gamma)^{85}Rb$ reaction.

2.5 Astrophysical S Factor

Cross sections can be very difficult if not impossible to measure experimentally at astrophysically relevant energies. The nuclear reactions taking place in stellar environments occur at low energies where the cross sections are significantly lower and drop off exponentially as a function of energy due to the Coulomb barrier. The Coulomb barrier is repulsive for particles of the same charge. The Coulomb potential can be written as

$$V_C = \frac{Z_1 Z_2 e^2}{r} \tag{2.21}$$

where Z_1 and Z_2 are the charges of the particles. However, particles also attract through the nuclear force and can still undergo quantum tunnelling through the Coulomb potential at low energies. This tunnelling probability is

$$P_t = e^{-2\pi \frac{Z_1 Z_2 e^2}{\hbar v}} = e^{-2\pi\eta} \tag{2.22}$$

where $\eta = Z_1 Z_2 e^2/\hbar v$. The cross section can then be rewritten in terms of this probability and the astrophysical S factor as

$$\sigma(E) = \frac{1}{E} e^{-2\pi\eta} S(E). \tag{2.23}$$

The exponential factor, $e^{-2\pi\eta}$, is also known as the Gamow factor which approximates the transmission probability for energies much lower than the Coulomb barrier. The Gamow factor removes most of the energy dependence from the $\sigma(E)$ and leaves the smooth function in Figure 2.4 [32] [5].

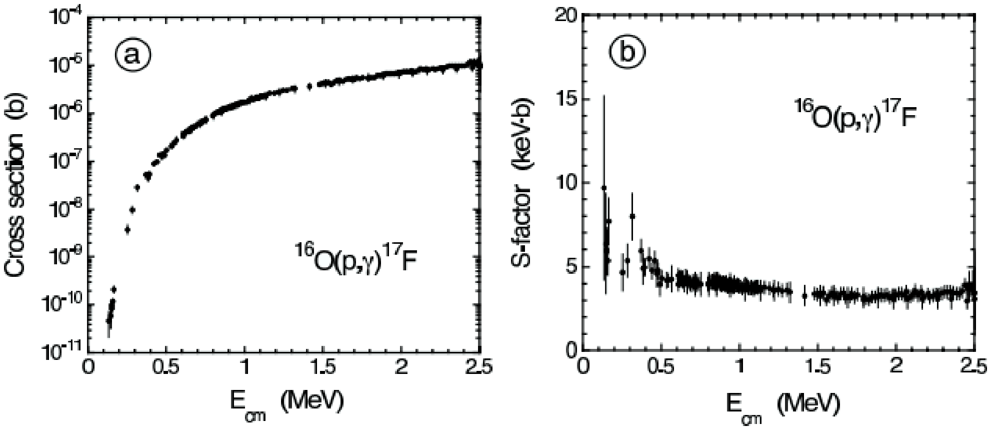

Figure 2.4: Figure taken from Illiadis with data from Angulo 1999 [32] [5]. (a) shows the cross section as a function of energy for the $^{16}\mathrm{O}(p,\gamma)^{17}\mathrm{F}$ reaction. At low energies there is an exponential drop off whereas in (b) it shows S(E) which is smooth at low energies.

Because the S(E) function changes less drastically at lower energies it is also more useful for extrapolating the cross section at low energies that are of astrophysical relevance. Figure 2.4 shows both the (a) cross section and the (b) astrophysical S factor, S(E), for the $^{16}\mathrm{O}(p,\gamma)^{17}\mathrm{F}$ reaction. This comparison highlights the differences and the usefulness of the astrophysical S factor. S(E) is much smoother at low energies than the cross section which drops off exponentially making S(E) more useful for extrapolation.

2.6 Nuclear Statistical Model

During a nuclear reaction, nuclei collide to form a new nucleus that is typically in an excited state. All nuclei have excited states; at low energies their excited states are discrete beginning at the lowest ground state energy and increasing. At higher excitation energies the energy levels become closer together until they must be treated as a continuum of excited states instead of discrete levels. These excited states typically have short lifetimes, $\approx 10^{-15}s$, before deexciting through a γ-ray emission back to the ground state or nucleon emission to another nucleus. Higher lying states do not have to deexcite straight to the ground state and can go through multiple energy levels before finally reaching the ground state. Some excited states can also live much longer and are called metastable or isomeric states.

A generic nuclear reaction can be written as $A + a \rightarrow B + b$ where A and a are the entrance channel nuclei and B and b are the exit channel nuclei. Each excited state, as well as the entrance and exit channels, have energy fluctuations about a mean energy. This fluctuation is known as the energy width, Γ. The energy widths of these states are related to the state lifetime, τ, through the Heisenberg uncertainty principle: $\Gamma = \hbar/\tau$. The energy widths of the entrance and exit channel represent the energies for which the reaction can occur, like an energy window, and are called partial widths, Γ_i. Summing over the partial widths gives the total energy width of the nuclear reaction. Taking the ratio of the partial width for a specific channel and the total energy width, Γ_1/Γ, gives the probability that the nuclear reaction will decay through that specific reaction channel and is called the branching ratio.

A compound nucleus is an intermediate state formed by the combination of a target and incident particle nucleus before decaying to stability. In some cases, the energies of

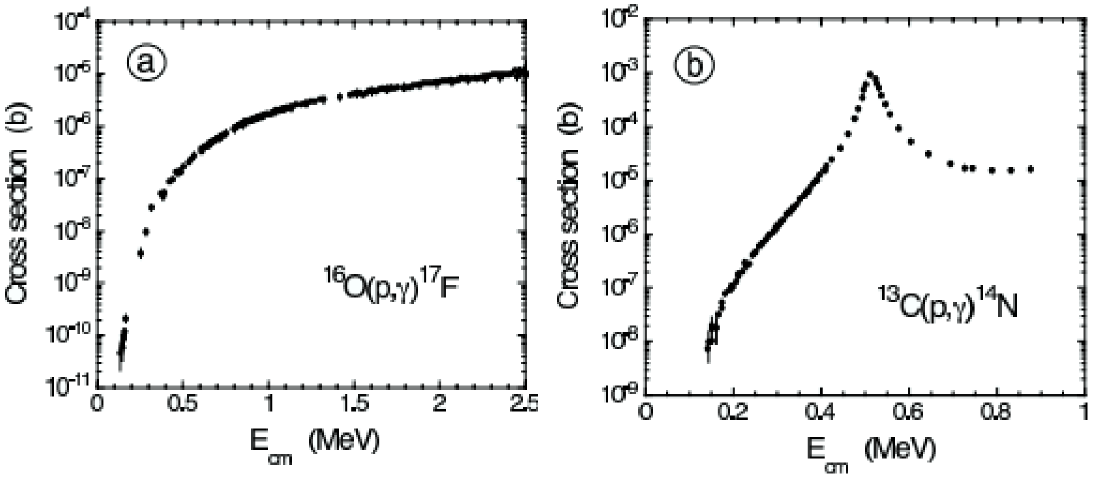

Figure 2.5: Figure taken from Illiadis [5] and (a) shows the ^{16}O(p,γ)^{17}F non-resonant cross section. Notice the cross section is smooth throughout the energies shown whereas (b) shows the ^{13}C(p,γ)^{14}N resonant cross section whose cross section has a peak around 0.55 MeV showing the resonance.

the nuclear reaction and the excited state of the compound nucleus will match and create a resonance. The resonance energy is the energy for which the probability is enhanced due to this phenomenon. There are also non-resonant reactions which do not have this property and instead are smoothly varying cross sections with respect to energy because the resulting nucleus has no energy levels in the corresponding energy range. Both can be seen in Figure 2.5 from Illiadis which (a) shows the ^{16}O(p,γ)^{17}F non-resonant cross section and (b) shows the ^{13}C(p,γ)^{14}N resonant cross section [5]. (a) is a smoothly varying cross section whereas (b) has an obvious peak or resonance in the cross section around 0.55 MeV. This thesis work will focus primarily on resonant reactions as the reactions discussed are resonant however their cross sections are not the same shape as shown in Figure 2.5 (b).

At lower excitation energies a resonant cross section will look similar to (b) in Figure 2.5 because there are a discrete number of excited states in the compound nucleus. However, as the energy increases the number of resonances and excited states will increase and begin to overlap. Imagine taking the single peak from (b) in Figure 2.5 and adding another to the cross

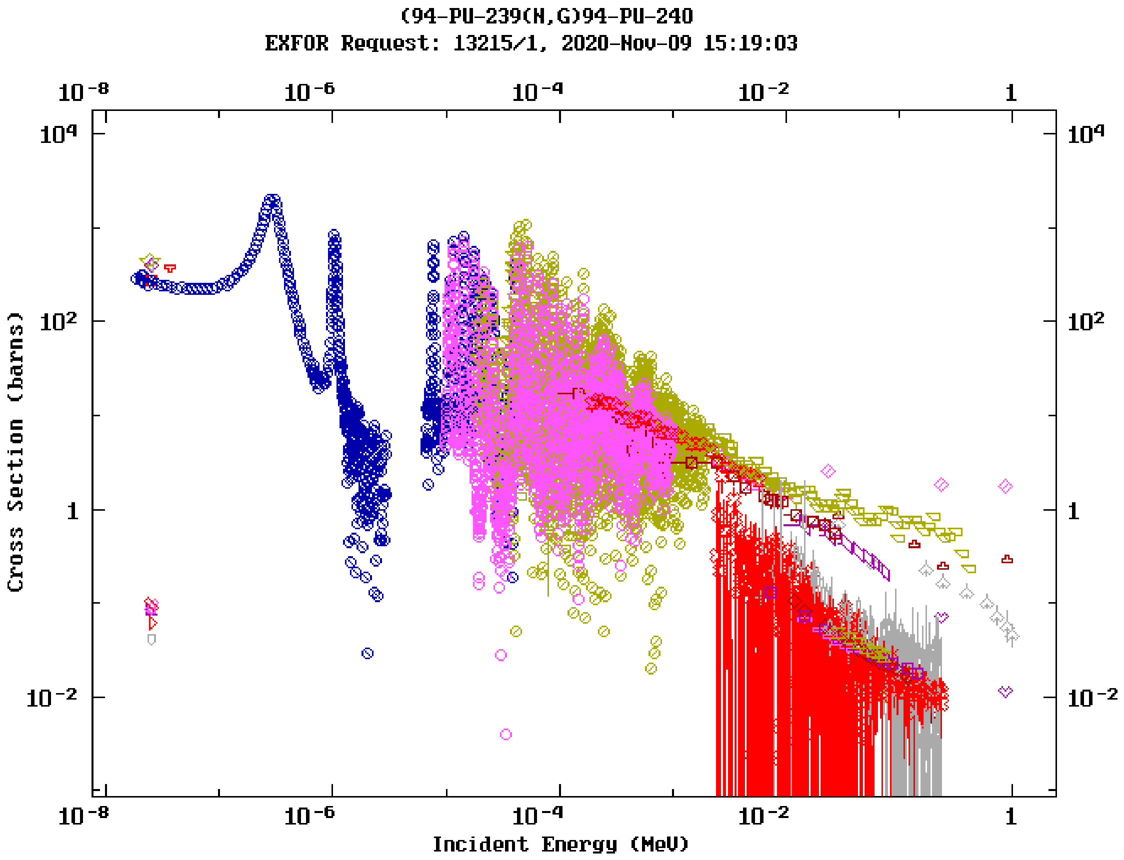

Figure 2.6: Shows the experimental cross sections for Plutonium-239. While the total cross section looks smooth as a function of energy it is actually made up of multiple resonant peaks.

section for each new energy level in the compound nucleus. Eventually the resonant cross section will begin to look the same as (a) from Figure 2.5 as more and more peaks are added since there are so many resonances. For example, the cross section of ^{239}Pu(n,γ)^{240}Pu is plotted in Figure 2.6. On the left side of the plot, there are discrete peaks from the discrete energy levels in the compound nucleus but as the energy increases the peaks increase in number and make the cross section appear smooth.

The theoretical cross section for the ^{84}Kr(p,γ)^{85}Rb reaction is shown in Figure 2.7. This cross section is also a resonant cross section similar to the cross section shown in Figure 2.6. Even though it appears smooth it is made up of multiple resonances. The slight dip

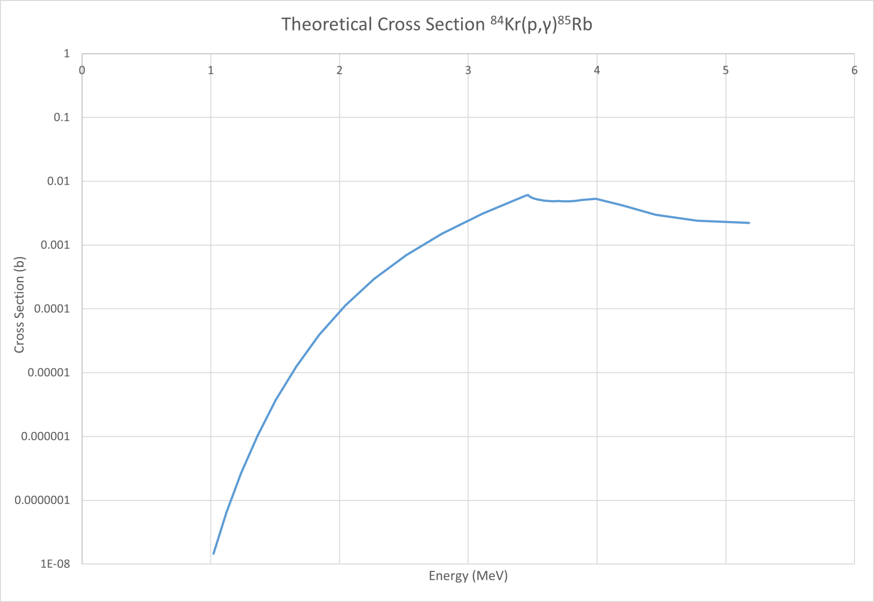

Figure 2.7: Shows the NON-SMOKER theoretical cross section for the ^{84}Kr(p,γ)^{85}Rb reaction. Notice that it has a smooth cross section but it is still a resonant cross section [33].

in the cross section around 3.4 MeV corresponds to the neutron channel opening which will decrease the cross section of the (p, γ) reaction occurring.

The resonant reaction cross section can be written with the Breit-Wigner equation

$$\sigma(E) = \frac{\omega\lambda^2}{4\pi}\frac{\Gamma_1\Gamma_2}{(E - E_r)^2 + (\Gamma/2)^2} \tag{2.24}$$

where ω is given by

$$\omega = \frac{2J_r + 1}{(2J_1 + 1)(2J_2 + 1)}, \tag{2.25}$$

λ is the de Broglie wavelength, Γ is the resonance width, E_r is the resonance energy, Γ_i are the partial widths of the entrance and exit channels and J_i are the respective angular momenta. Notice in Figure 2.8, that these Breit-Wigner resonances are quite narrow. These resonances are also dependent on the angular momenta of the excited states and will follow quantum selection rules which are accounted for with the expression for ω.

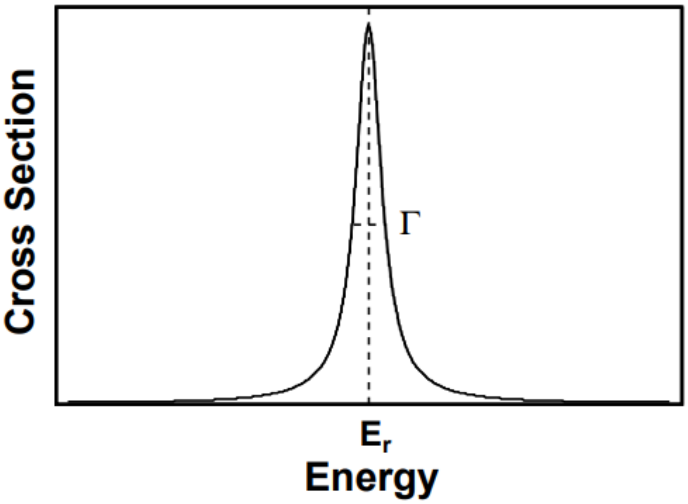

Figure 2.8: Shows the shape of a Breit-Wigner resonance with energy E_r and width Γ.

To see the effect of the resonances on the reaction rates, the cross section from Equation 2.24 is plugged into the derived reaction rate from Equation 2.15. Before writing the expression, note that the resonances will act like a delta function within the integral since they are so sharp. Therefore, the resonances can be removed from the integral and replaced simply by the energy of the resonance, E_r. The substitution $\lambda^2/4\pi = \pi\hbar^2/(2\mu E)$ is also made and the reaction rate can then be written as

$$\langle\sigma v\rangle = \sqrt{\frac{2\pi}{(\mu kT)^3}}\hbar^2\omega\Gamma_1\Gamma_2 e^{-E_r/kT}\int_0^\infty \frac{1}{(E-E_r)^2+(\Gamma/2)^2}dE \tag{2.26}$$

where the integral simplifies to

$$\int_0^\infty \frac{1}{(E-E_r)^2+(\Gamma/2)^2}dE = \frac{2\pi}{\Gamma}. \tag{2.27}$$

Plugging this into Equation 2.26, the reaction rate is

$$\langle\sigma v\rangle = \omega\gamma\left(\frac{2\pi}{\mu kT}\right)^{3/2}\hbar^2 e^{-E_r/kT} \tag{2.28}$$

where $\omega\gamma$ is defined as the resonance strength

$$\omega\gamma = \frac{2J_r + 1}{(2J_1 + 1)(2J_2 + 1)} \frac{\Gamma_1 \Gamma_2}{\Gamma}. \tag{2.29}$$

These resonant reaction rates are then dependent on the resonance strength ($\omega\gamma$), the resonant energy (E_r) and the temperature of the stellar environment.

At lower energies the excitation energies of the nucleus are discrete and well spaced. As the excitation energy, related to the beam energy for an experiment as well as the temperature within the star, increase, these levels become more numerous and begin to overlap. It becomes imprudent to treat the levels separately and instead to treat the levels statistically and average over the resonances. As the energy levels become more numerous and closer together the cross section will appear to look smooth because of the quantity of overlapping resonances. Consider an energy range, ΔE, at a high excitation energy where there are multiple overlapping Breit-Wigner resonances that correspond to energy levels in a compound nucleus. The average over this region can be calculated starting with Equation 2.24 and integrating over the energy region while simultaneously summing over the energy levels present by writing

$$\langle \sigma_{12}(E) \rangle = \frac{1}{\Delta E} \int_{E-\Delta E}^{E} \sum_i \frac{\omega \lambda^2}{4\pi} \frac{\Gamma_1 \Gamma_2}{(E' - E_r)^2 + (\Gamma/2)^2} dE' \tag{2.30}$$

where ω is given by Equation 2.25 and depends on the angular momentum, J and parity, and the sum is over the Breit-Wigner resonances. For a complete solution the angular momentum dependence must also be taken into account and summed which will be added in later steps of the derivation. Recall ω is energy independent as well as the sum which is simply the number of Breit-Wigner resonances within the energy range, n_{res}, and both can be removed from the integral. The previous expression is now

$$\langle \sigma_{12}(E) \rangle = \frac{\omega \lambda^2}{4\pi} \frac{n_{res}}{\Delta E} \int_{E-\Delta E}^{E} \frac{\Gamma_1 \Gamma_2}{(E' - E_r)^2 + (\Gamma/2)^2} dE'. \tag{2.31}$$

The expression $n_{res}/\Delta E$ can be simplified as $\rho(E)$ where $\rho(E)$ is the average level spacing or the level density as a function of energy. The average level spacing is much smaller than the energy range of interest and thus the integral can be taken from zero to infinity. With these limits of integration the results of Equation 2.27 can be plugged into the previous expression and simplified to

$$\langle \sigma_{12}(E) \rangle = \frac{\lambda^2}{2\pi} \omega \rho \left\langle \frac{\Gamma_1 \Gamma_2}{\Gamma} \right\rangle. \tag{2.32}$$

It is also important to note that the quantity $\langle \Gamma_1 \Gamma_2 / \Gamma \rangle$ can be rewritten such that the energy widths are independent of each other by introducing a width fluctuation correction that is spin and parity dependent. This idea was originally proposed by Niels Bohr in 1936 [34] when he hypothesized that a projectile nucleus that forms a compound excited system with the target will deexcite independently of its formation and "forget" the entrance channel used to populate the compound nucleus. This is known as the independence hypothesis. Thus the substitution

$$\left\langle \frac{\Gamma_1 \Gamma_2}{\Gamma} \right\rangle = W_{12}(J, \Pi) \frac{\langle \Gamma_1 \rangle \langle \Gamma_2 \rangle}{\langle \Gamma \rangle} \tag{2.33}$$

can be made where $\langle \Gamma \rangle = \sum_i \langle \Gamma_i \rangle$ [35]. Now Equation 2.32 can be rewritten with the angular momentum and spins added and the substitution from Equation 2.33 for a final form of the cross section as

$$\langle\sigma_{12}(E)\rangle = \sum_{J,\Pi} \frac{\lambda^2}{2\pi}\omega_J \rho(E,J,\Pi)\frac{\langle\Gamma_{1,J,\Pi}\rangle\langle\Gamma_{2,J,\Pi}\rangle}{\langle\Gamma_{J,\Pi}\rangle}W(E,J,\Pi). \tag{2.34}$$

The total cross section can be written by summing over all the exit channels, $\sum_i \Gamma_i = \Gamma$, and if we consider a case where the projectile and target have J=0 this expression is

$$\langle\sigma_1^{tot}(E)\rangle = \frac{\rho\lambda^2}{2\pi}(2l+1)\langle\Gamma_1\rangle. \tag{2.35}$$

where l is the orbital angular momentum of the resonance. This $\langle\Gamma_1\rangle$ expression can be thought of as a transmission coefficient and notice how in Equation 2.34 they are all independent of each other. The energy widths are related to the transmission coefficients through this relationship

$$T = 2\pi\rho(E)\langle\Gamma\rangle \tag{2.36}$$

and it holds true for all of the widths, Γ, Γ_1 and Γ_2 [35]. Using this relationship and plugging back into Equation 2.34, the average cross section can be rewritten as the Hauser-Feshbach equation

$$\langle\sigma_{12}(E)\rangle = \frac{\lambda^2}{4\pi}\sum_{J,\Pi} W_{12}\omega\frac{T_{1,J,\Pi}T_{2,J,\Pi}}{T_{J,\Pi}}. \tag{2.37}$$

where W_{12} is the width fluctuation parameter and T_i are the transmission coefficients with their spin and parity dependence J, Π [36]. The width fluctuation describes the non-statistical relationship between the entrance and exit channels and are generally of importance only at channel openings. At higher excitation energies when the statistical region for Hauser-Feshbach is reached, the fluctuation is typically one.

The Hauser-Feshbach model is an extension of the Bohr independence hypothesis built on the fact that the entrance and exit channels for a compound nucleus are independent. The projectile and target nuclei will interact by scattering or absorption into an excited state that shares energy between the nucleons. Because the energy is shared the lifetimes of the compound nucleus are long enough that the compound nucleus decays independently of its formation channel and "forgets" its formation.

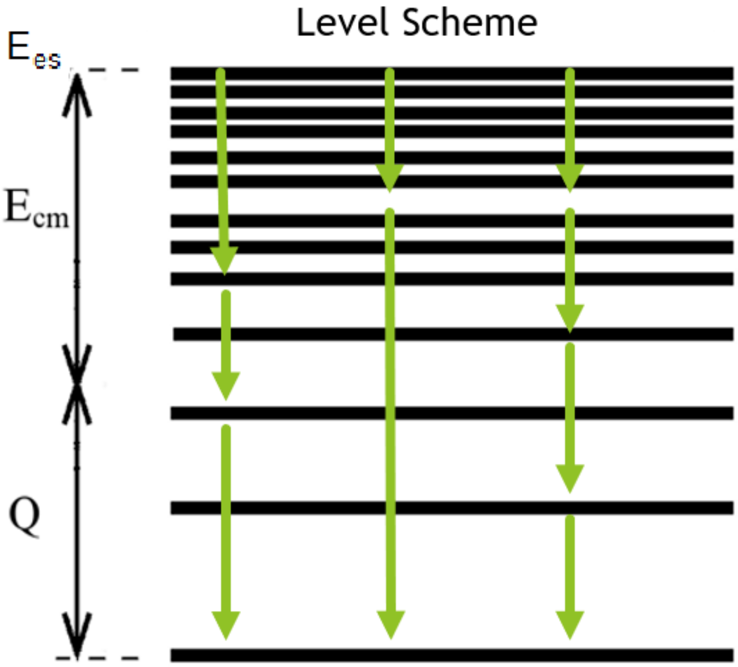

Figure 2.9: Shows an example of a level scheme beginning with discrete levels and increasing in energy and levels to a statistical region with overlapping energy states. There are example γ-ray cascades from an initial entry state energy, E_{es}.

The transmission coefficients can be expressed through the level density as shown by the relationship in Equation 2.36. When at higher energies decaying from the continuum the total transmission coefficient is given by

$$T = \sum_{i}^{cut} T_i + \sum_{j} \int_{E^{cut}}^{E^{max}} = T_j(E')\rho_j(E', J, \Pi)dE' \tag{2.38}$$

where ”cut” refers to the cutoff of experimentally known energy levels. For the discrete levels the transmission coefficient is simply T and in the continuum it depends on the level density, ρ, up to a maximum allowed energy state. Having the correct theoretical model for the level density is very important as it can drastically change the simulated cross sections. Figure 2.9 shows an example of a level scheme for an excited nucleus. The level density increases as the energy increases going from discrete to statistical with overlapping levels. These transmission coefficients are calculated by solving the Schrödinger equation with the correct potentials. For particles it is imperative to find the correct optical model potential. The optical model potential dictates how the nucleons interact with one another when creating the compound nucleus. For γ rays the Schrödinger equation is solved with various radiative strength functions, or γ-ray strength functions. The γ-ray strength function gives the probability for each γ-ray in a cascade and defines how a compound nucleus should statistically decay. The transmission coefficients for γ rays is

$$T_{\chi\lambda}(E_\gamma) = 2\pi f_{\chi\lambda}(E_\gamma) E_\gamma^{2\lambda+1} \tag{2.39}$$

where χ denotes whether it is an electric or magnetic transition, E or M, respectively and γ denotes the transition multipolarity or the angular momentum of the γ ray. As with the level densities, the specific γ-ray strength function models used are very important and can have a large effect on the final cross section. Of course there are more nuclear properties than the level densities and γ-ray strength functions required as inputs into the Hauser-Feshbach formulism such as masses, half-lives, and radii. For this work, the level densities and the γ-ray strength functions were the most important parts of using the Hauser-Feshbach formulism since the other nuclear properties involved are mostly experimentally known. The simulations done for this work with the statistical model code RAINIER and will be discussed further in Chapter 5.

2.7 Reciprocity Theorem

The p process is a series of photodisintegration reactions, (γ,n), (γ,p), (γ,α), which have previously been measured directly with γ beams [37]. However, it is generally beneficial to measure the inverse for astrophysical reactions: (n,γ), (p,γ), (α,γ). This thesis work directly measured the inverse reactions, ^{84}Kr(p,γ)^{85}Rb, even though the reactions taking place in the stellar environment are ^{83,85}Rb(γ, p)^{82,84}Kr. Fortunately, the two reactions can be related through the reciprocity theorem also known as the detailed balance theorem [38].

Let us consider an arbitrary nuclear reaction, $A+a \rightarrow B+b$. At a given energy the cross sections between this and its inverse reaction, $B+b \rightarrow A+a$, can be denoted with respect to the available exit states for each channel. The states available with respect to momentum between the left and right sides of the reaction for each process is proportional to p^2 [39]. Therefore we can write

$$\sigma_{Aa\rightarrow Bb} \sim p^2_{Bb} \tag{2.40}$$

and

$$\sigma_{Bb\rightarrow Aa} \sim p^2_{Aa} \tag{2.41}$$

where p is the momentum. The momentum can be rewritten in terms of the de Broglie wavelength, $\lambda = h/p$, but λ can also be written in terms of the wave number, k, as $\lambda = 2\pi/k$. Equating these two expressions gives the relationship $p = \hbar k$ and then Equations 2.40 and

2.41 can be written as

$$\frac{k_{Aa}^2 \sigma_{Aa\to Bb}}{(1+\delta_{Aa})} = \frac{k_{Bb}^2 \sigma_{Bb\to Aa}}{(1+\delta_{Bb})}. \tag{2.42}$$

The Kronecker delta terms account for the differences between cross sections with identical and different particles in the entrance channel and will go to zero when the particles are not the same. This means identical particle cross section are twice those for different particles. In order to account for particles with spin, Equation 2.42 must be modified. There are $(2J_i+1)$ spin states available for the particles. This factor goes to two for photons as photons only have two different polarization states. Taking spin into account and assuming A, a, B and b are not photons, we get

$$\frac{k_{Aa}^2 (2J_A+1)(2J_a+1)\sigma_{Aa\to Bb}}{(1+\delta_{Aa})} = \frac{k_{Bb}^2 (2J_B+1)(2J_b+1)\sigma_{Bb\to Aa}}{(1+\delta_{Bb})} \tag{2.43}$$

which can be solved for the cross section ratio

$$\frac{\sigma_{Bb\to Aa}}{\sigma_{Aa\to Bb}} = \frac{k_{Aa}^2 (2J_A+1)(2J_a+1)(1+\delta_{Aa})}{k_{Bb}^2 (2J_B+1)(2J_b+1)(1+\delta_{Bb})} \tag{2.44}$$

which gives us the reciprocity theorem [38].

The experimental cross section in the laboratory, where both the target and projectile are in the ground state, was derived giving Equation 2.15. However, in a stellar environment the particles may be in low-lying excited states instead of the ground state. The probability of a nucleus being in an excited state i is given by the ratio of the number densities as was used in Section 2.2 to derive Equation 2.7. The ratio of the number density of a particle in excited state i, N_i, and the total number density, N, then gives the probability of a particle being in excited state i. The probability is given by the Boltzmann distribution

$$P_i = \frac{N_i}{N} = \frac{g_i e^{-E_i/kT}}{\sum\limits_i g_i e^{-E_i/kT}} = \frac{g_i e^{-E_i/kT}}{G} \tag{2.45}$$

where $g_i \equiv (2J_i + 1)$ is the statistical weight from spin, J_i is the spin and E_i is the excitation energy of the state, i [40]. k is the Boltzmann constant, T is the energy of the stellar plasma and G is the partition function that is the sum over i including the ground state. The reaction rate for ground state nuclei, and what is measured in the lab, can therefore be written as

$$\langle \sigma v \rangle_{Aa \to Bb} = \sum_j \langle \sigma v \rangle_{Aa \to Bb}^{g.s. \to j} \tag{2.46}$$

where j is the energy state in nucleus b.

As mentioned previously, in a stellar environment the reaction rates for excited nuclei, $\langle \sigma v \rangle^*$, are of primary importance over nuclei in the ground state, $\langle \sigma v \rangle$. Going back to our arbitrary reaction, $A + a \to B + b$, the reaction rate with excited nuclei is denoted by summing over all acceptable transitions from nuclei A and a into the excited states of nuclei B and b with the correct averaging of excited state combinations in nuclei A and a. This is given as

$$\langle \sigma v \rangle_{Aa \to Bb}^* = \sum_i P_{Ai} \sum_j \langle \sigma v \rangle_{Aa \to Bb}^{i \to j} = \frac{\sum_i g_{Ai} e^{-E_{Ai}/kT} \sum_j \langle \sigma v \rangle_{Aa \to Bb}^{i \to j}}{\sum_i g_{Ai} e^{-E_{Ai}/kT}} \tag{2.47}$$

where i is the energy state in nucleus A and j is the energy state in nucleus b. These two expressions for the reaction rates have the same general form for the inverse reactions as well.

Using Equation 2.45, stellar reaction rates can be calculated from the ground state reaction rates measured in a lab through statistical model theories [33]. This ratio of reaction rates is called the stellar enhancement factor

$$f^* = \frac{\langle \sigma v \rangle^*}{\langle \sigma v \rangle^{g.s.}}. \tag{2.48}$$

Combining this definition, the expressions for the reaction rates, Equations 2.46 and 2.47, and the expression for the probability from Equation 2.45 we get the final expression for the ratios of the stellar reaction rate and its inverse [5].

$$\frac{\langle \sigma v \rangle^*_{Bb \to Aa}}{\langle \sigma v \rangle^*_{Aa \to Bb}} = \frac{g_A g_a (1 + \delta_{Bb}) G^n_A G^n_a}{g_B g_b (1 + \delta_{Aa}) G^n_B G^n_b} \left(\frac{M_A M_a}{M_B M_b} \right)^{3/2} e^{-Q/kT} \tag{2.49}$$

where M is mass, Q is the Q-value of the reaction, and G^n is the normalized partition function. It is normalized to the ground state spin: $G^n = \sum (2J^{g.s.} + 1) e^{-E/kT} / (2J^{g.s.} + 1)$.

This thesis reaction and the p-process reactions typically involve a photon in the entrance or exit channel; therefore, let us rewrite Equation 2.49 with a photon. Now instead of the reverse reaction we have the decay constant, λ_γ. Thus the relationship between the photodisintegration reaction and its inverse capture reaction is

$$\frac{\lambda^*_{Bb \to Aa}}{\langle \sigma v \rangle^*_{Aa \to Bb}} = \frac{g_A g_a G^n_A G^n_a}{g_B (1 + \delta_{Aa}) G^n_B} \left(\frac{M_A M_a}{M_B} \right)^{3/2} \left(\frac{\mu_{Aa} kT}{2\pi \hbar^2} \right)^{3/2} e^{-Q/kT} \tag{2.50}$$

where μ_{Aa} is the reduced mass of nuclei A and a [41].

Cross section measurements in the lab are not measuring the same cross section that occurs in a stellar environment. However, the reverse and forward relationship between cross sections provides the ability to go between the two values with the stellar enhancement

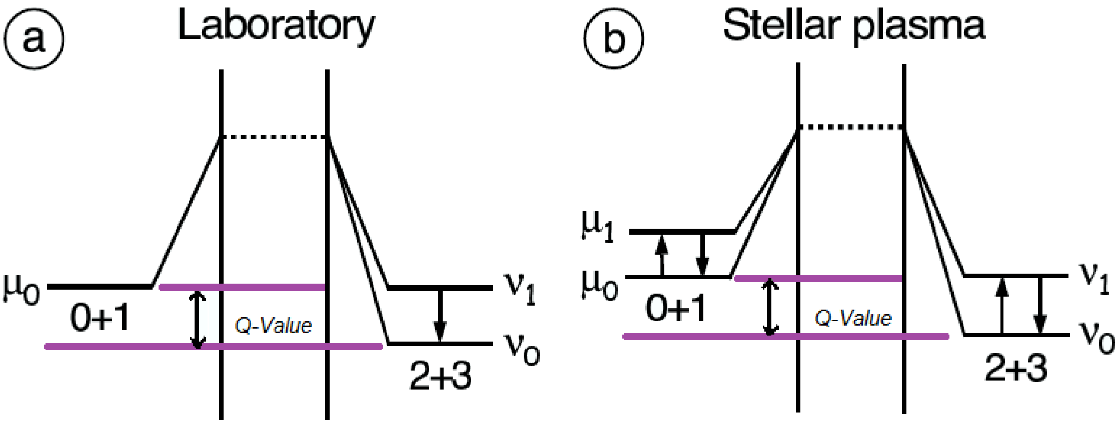

Figure 2.10: Figure taken from Illiadis and shows a cartoon example of a capture reaction, $1+2 \to 3+4$, in the (a) lab and (b) a stellar plasma. The reaction has initial energy levels, μ, and final energy levels, ν [5].

factor. Figure 2.10 shows a cartoon example of a reaction, $0+1 \to 2+3$, in the lab and in a stellar environment taken from Illiadis [5]. In part (a) the initial nucleus, 0, has a ground state energy of μ_0 and the final nucleus, 3, has energy levels ν_i. Part (b) shows how within the stellar plasma the starting nucleus, 0, can also start with higher energy levels μ_i. The ground states, marked with purple lines, in both cases are offset by the Q value of the reaction which allows for higher energy states to be populated in the resulting nucleus, in this case $2+3$. For reactions with a positive Q value, the ground state contribution to the stellar reaction rate is the largest which makes measurements in the lab on ground state nuclei advantageous. For p-process reactions, the capture reactions generally have a positive Q value; for example, the reactions measured in this thesis work has a Q-value of 7MeV. After the lab measurements from the ground state are completed they can be converted into the stellar reaction rates with Equation 2.50. These capture reaction measurements are a better representation of the stellar reaction rates than the photodisintegration reaction measurements.

Chapter 3

Experimental Techniques

3.1 Experimental Set Up: Overview

This experiment was run at the National Superconducting Cyclotron Laboratory (NSCL) with the ReAccelerator (ReA) facility at Michigan State University (MSU). For the ^{84}Kr(p,γ)^{85}Rb cross section measurements, a stable Kr beam was injected into the cooler-buncher and accelerated to the experimental setup installed on the multi purpose beam line of the ReA experimental area. While this reaction was on a stable nucleus, future experiments with re-accelerated radioactive beams from the Facility for Rare Isotope Beams (FRIB), the A1900 and the gas stopper will be used with this technique to directly measure cross sections on radioactive isotopes and will be described in more detail in Section 3.1.1.

This setup uses a new gas cell target which was designed, built, tested and placed in the center of the Summing NaI (SuN) detector which will be discussed further in section 3.1.2 [42]. The Scintillating Cosmic Ray Eliminating ENsemble (SuNSCREEN) [43] was placed above the SuN detector to help eliminate the cosmic ray background as a veto detector. Eliminating the cosmic ray background is very important for these types of experiments as it dominates the energy spectra in the sum peak region. In order to measure these cross sections, thorough background subtraction techniques must be implemented. The background subtraction methods used in this work will be discussed in Section 4.3. Figure

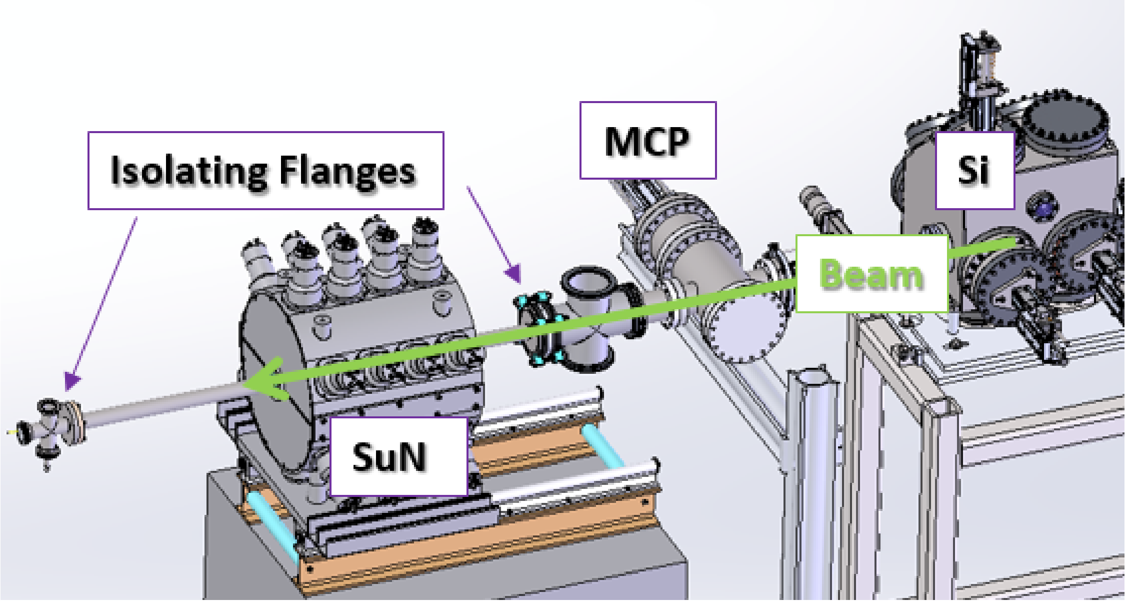

Figure 3.1: A close up of the experimental setup. The beam went from right to left following the green arrow. The positions of the Si and MCP detectors are shown. The SuNSCREEN detector is not pictured here but was sitting above SuN and the gas target was at the center of the SuN detector.

3.1 shows the experimental end station without SuNSCREEN which sat directly above SuN. The silicon (Si) and micro channel plate (MCP) detectors were tested for future radioactive beam experiments where the beam rates and currents are too low to be measured directly off the beam pipe. For this work, the beam currents were measured with isolating flanges off the beam pipe which were used as a Faraday cup. The ^{82,84}Kr beam moved from right to left along the green arrow in Figure 3.1 and the gas cell sat in the center of SuN. At the end of the beam pipe on the left gas was fed into the gas inlet tube to fill and empty the gas cell with hydrogen gas.

The ^{84}Kr(p,γ)^{85}Rb reaction cross sections were measured at four beam energies within the Gamow Window: 3.7, 3.4, 3.1 and 2.8 MeV/u. Data was taken with the gas target empty and full of hydrogen gas in order to isolate and subtract beam induced background. To isolate the room background the beam was delivered in 100 μs pulses with 200 ms of dead time and the room background was subtracted from the final spectra which will be discussed in Section 4.3.

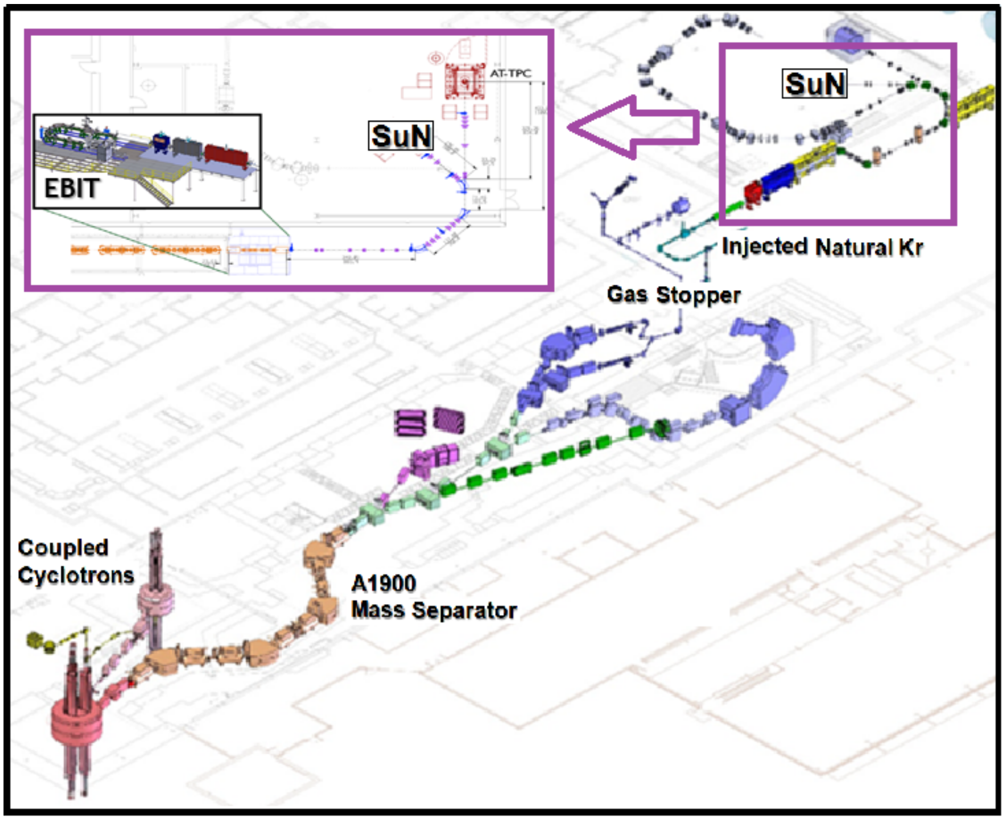

Figure 3.2: An outline of the NSCL and ReA facilities. Our beam began with injecting an ^{84}Kr beam into the cooler-buncher before EBIT and was then accelerated to our experimental end station shown in Figure 3.1.

3.1.1 NSCL and ReA

This experiment was performed at the ReA facility at MSU. ReA has the ability to re-accelerate stopped radioactive beams from the NSCL and to accelerate stable beams from its own surface ion source [44]. These beams can be accelerated from energies of approximately 300 keV/u to 6 MeV/u. For this work, a stable ^{84}Kr beam was produced from the surface ion source and then extracted into the electron-beam ion trap (EBIT). The EBIT converted the ^{84}Kr beam into a higher charge state, 27+, by stripping electrons. Once the electrons are stripped, the beam is accelerated through a radiofrequency quadrupole (RFQ) and linear accelerator (LINAC) to an energy of 3.7, 3.4, 3.1, and 2.8 MeV/u into our setup. The NSCL and ReA facilities are shown in Figure 3.2. ReA beams are delivered into one of three beam lines shown in the top right corner of the figure. On the left side there is a close up of the EBIT, RFQ and LINAC that lead into the three lower energy beam lines. The experimental end station was installed on the multi purpose beam line in the low energy area shown in Figure 3.2. The EBIT can also provide pulsed beams into the setup which was essential for background subtraction in the present experiment.

3.1.2 Experimental End Station

The experimental end station for this experiment consisted of four main components: SuN, SuNSCREEN, the gas cell target and detectors to measure the beam current. This setup was installed on the ReA multi purpose beam line as shown in Figure 3.2. This section will go through each of these in greater detail starting with the SuN detector.

SuN is a total absorption γ-ray detector used for measuring (p, γ) and (α, γ) reaction cross sections with the γ-summing technique [42]. This technique will be discussed in greater detail in Section 3.2. SuN is a NaI(TI) barrel that is 16 inches in height and 16 inches in diameter with a 1.7 inch borehole along its central axis as shown in Figure 3.3. This provides a nearly 4π coverage for γ-rays being emitted at its center. SuN is ideal for high efficiency measurements however, it has a lower energy resolution than other types of γ-detectors, like germanium, which have higher resolution but lower efficiency.

There are eight optically isolated crystals in SuN and each has three photomultiplier tubes (PMTs). The isolation of the crystals allows single segment analysis simultaneously to the summing analysis. In this way, SuN can be used to see both the individual γ-ray

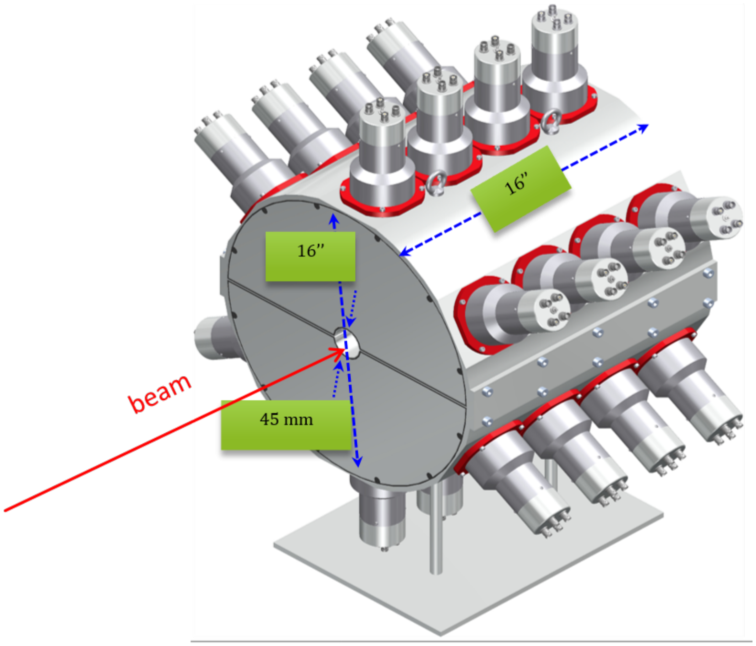

Figure 3.3: A schematic of the SuN detector. SuN is a segmented total absorption γ-ray detector made of sodium iodide. [42]

energies of a cascade and the energy of the levels. SuN has previously been used for froward and inverse kinematics reaction measurements [45] [46] [47] [48] [49] [50]. The previous inverse kinematics experiments had results with good agreement to previous measurements and inverse kinematics is used in this work as well [48]. This technique will be discussed in greater detail in Section 3.3.

For astrophysics reactions, the energy range of interest contains a large amount of cosmic ray background. Low cross sections in the Gamow window lead to sum peaks with fewer counts compared to the cosmic background. Sum peaks will be discussed in greater detail in Section 4.2. Background subtraction becomes very important for the measurements and especially for radioactive beams with lower rates than those seen in this work. For this work two methods were used for background subtraction: SuNSCREEN and the beam timing. More details about the beam timing will be discussed in Section 4.3.

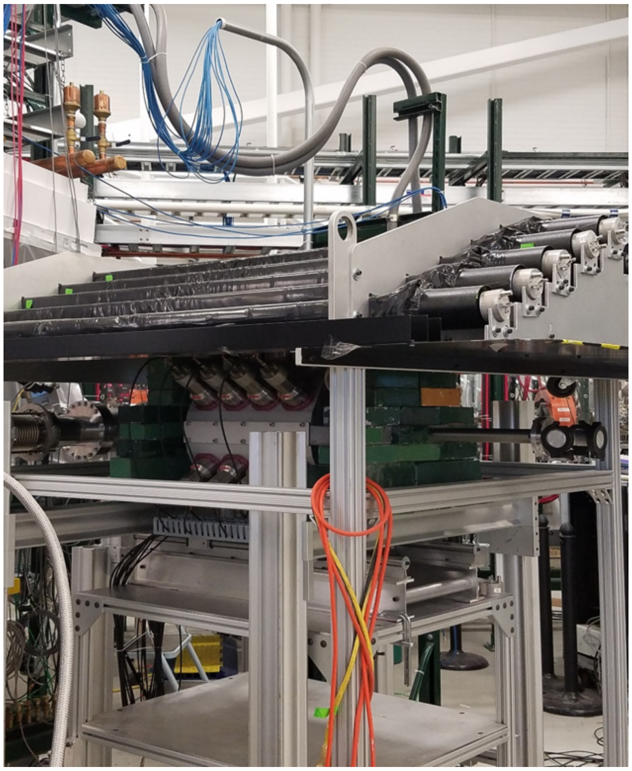

Figure 3.4: The SuNSCREEN detector sitting above the SuN detector from the experiment measuring the $^{84}Kr(p,\gamma)^{85}Rb$ cross section. The green bricks are lead bricks to help reduce background. The beam went through the center of SuN from left to right.

SuNSCREEN is a set of nine plastic scintillating bars placed above SuN as shown in Figure 3.4 [43]. This detector was used to veto cosmic events that would show up in SuN and create background counts in the energy area of interest. The PMTs are labelled 1-9 from right to left as seen in 3.4. Each bar is a 5 in x 2 in x 60 in rectangular box wrapped with a thickness of 5.08 cm in a layer of teflon tape, aluminum foil and two layers of 0.01 in black opaque plastic [43]. The bars overlap their neighboring bars by 0.75 in to form a roof above SuN for optimal angular rejection cover. The front PMTs are up stream and the back PMTs are down stream towards the right side of the picture. In order to reduce background noise from the PMTs, a coincidence is required between the front and back PMT in the same bar. γ-rays from the reactions of interest within SuN will not make it into SuNSCREEN. The events in SuNSCREEN are then cosmic or room background events and but this background will enter SuNSCREEN and then enter SuN. Thus, on an event by event basis anything in SuN coming in coincidence with a good signal from SuNSCREEN was rejected as cosmic-ray background. In tandem with SuNSCREEN, a pulsed beam from EBIT was used to eliminate most of the remaining background. More details about this process will be discussed in Section 4.3.

The last important piece of this experiment was the hydrogen gas cell target. The cell is shown in Figure 3.5 which shows both a front view, (a), and a side view, (b). The gas cell is made of two plastic halves that are glued together and was designed at Hope College. The foil on the front face of the cell in Figure 3.5.a is made of tantalum. The inside of the gas cell is also lined with the same tantalum foil in order to shield the beam from the plastic walls of the cell which would induce background through fusion-evaporation reactions. The inner foil is a thin 2 μm molybdenum foil chosen for being strong enough to hold the 650 Torr pressure but a heavy enough nucleus to minimize background from reactions with the beam. While the gas cell introduced more complications with the analysis, it was used in order to have a pure target. With low cross sections and low beam intensities, it is important that every beam particle that makes it into the setup interacts with hydrogen instead of other impurities which would be present in a solid hydrogen target. The use of the gas cell introduced new analysis difficulties from the energy straggling through the gas cell window and the gas. The energy straggling also changed the shape of the sum peak and the overall summing efficiency of the SuN detector. Simulations were performed with previous SuN data for the ^{90}Zr$(p,\gamma)^{91}$Nb reaction in order to create and validate a new analysis technique to extract SuN's efficiency. These efficiency calculations will be discussed in detail in Chapter 5.

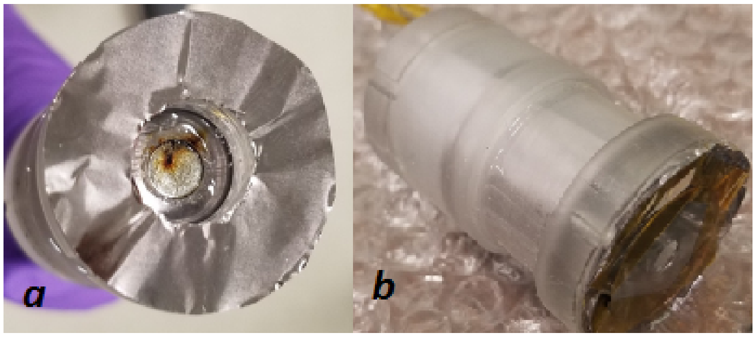

Figure 3.5: Two different views of the gas cell target that was filled with hydrogen gas at the center of SuN. (a) shows the front face of the cell and (b) shows the side of the cell.

In order to isolate the beam induced background from the cell, measurements were taken with the cell empty and full of hydrogen gas. The statistics for each beam energy were summed for the full cell and empty cell runs. Once summed the runs were scaled based on the beam current deposited into the beam pipe and then subtracted. This ensured that whatever background made from the beam interacting with the cell itself was removed from the final spectra.

For this experiment there was a gas handling system used in order to fill and empty the cell of hydrogen gas safely. Figure 3.6 shows (a) a schematic overview of the gas handling system for the SuN hydrogen gas target, (b) the upper panel and (c) lower panel of the gas handling system. The gas handling system comprises of a hydrogen gas bottle, a hydrogen reservoir, the beam line holding the cell and the gas cell target. The hydrogen bottle is always isolated from the rest of the system to ensure that hydrogen does not leak into the beam line or the cell. A smaller reservoir is filled with hydrogen gas from the bottle that is used to fill the cell with 650 Torr of hydrogen gas to make the setup ”beam ready”.

The lower panel, (c) in Figure 3.6, had all the valves responsible for emptying and filling the beam line and cell. The beam line has to be vented and pumped down simultaneously to the gas cell to ensure that the pressure difference is never large enough to break the cell

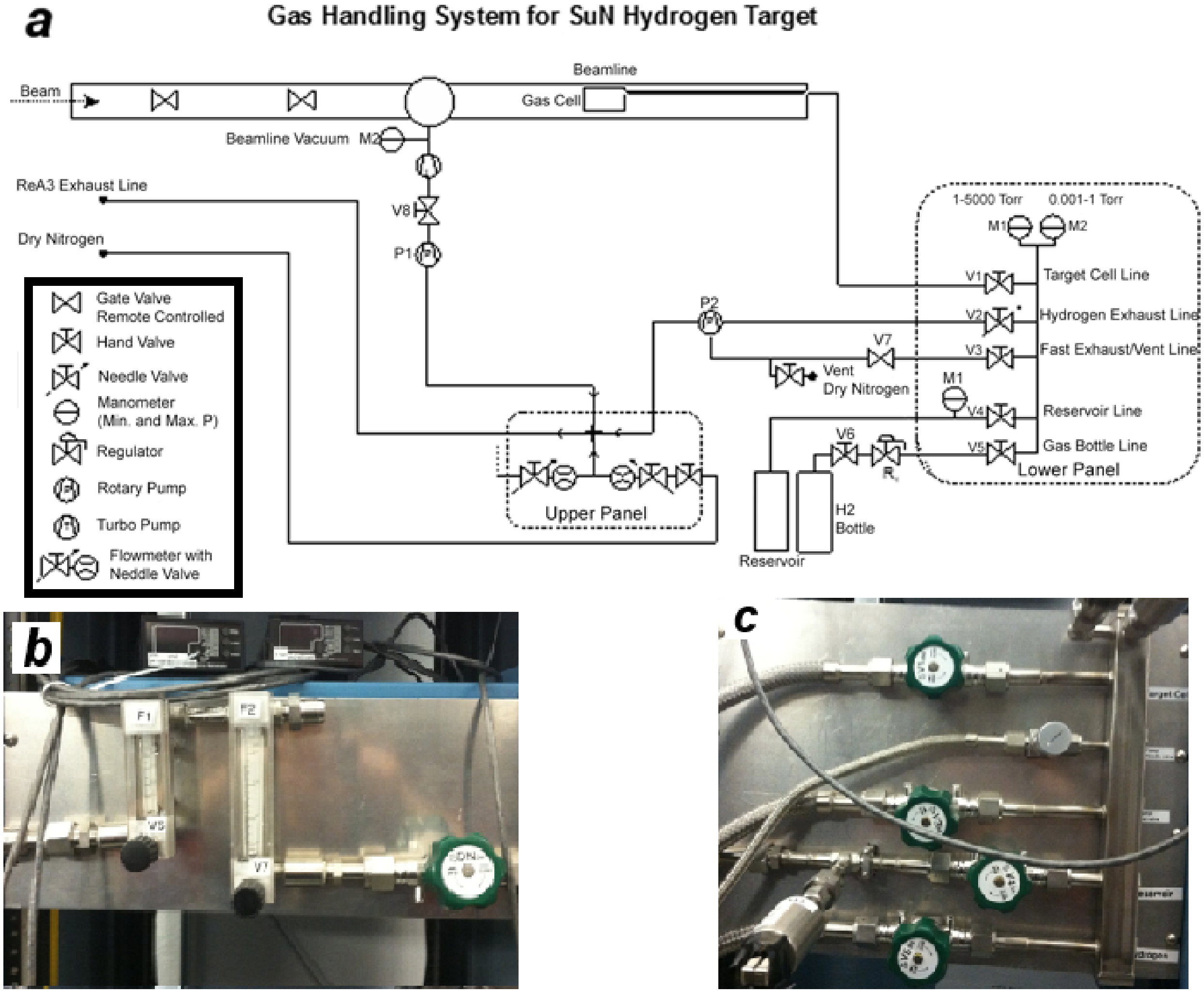

Figure 3.6: Shows (a) a schematic overview of the gas handling system for the SuN hydrogen gas target, (b) the upper panel and (c) lower panel of the gas handling system.

foils. Once the beam line and the cell are at vacuum, the gas cell is filled with hydrogen and monitored remotely with a manometer signal read through an EPICS channel controlled by a dual-channel PDR200 unit. The upper panel, (b) in Figure 3.6, shows the flowmeters monitoring the dry nitrogen and the hydrogen gas bottle. These should only change when filling the reservoir or venting with dry nitrogen.

3.2 Summing Technique

SuN uses the γ-summing technique for direct cross section reaction measurements [51] [42]. Once the beam and the target interact a compound nucleus is formed in an excited state. This excited state has an entry state energy as seen in Figure 3.7 at the center of mass energy plus the Q-value for the reaction, $E_{es} = Q + E_{cm}$. The center of mass energy is as follows:

$$E_{cm} = E_b \frac{m_t}{m_b + m_t} \tag{3.1}$$

where E_b is the beam energy in MeV, m_b is the beam mass and m_t is the target mass. For this experiment the correction is slight since the target is hydrogen with a mass of one making the mass fraction term close to one as well. When the compound nucleus is created in this excited state it will emit γ-rays or particles at high enough energies until the nucleus reaches its ground state or a long lived isomeric state. If this target is then surrounded by a γ-ray summing detector it is possible to measure the emitted γ-rays and determine how many times this nucleus was created or how often this reaction of interest occurred.

For the summing technique, the γ-rays from the reaction are measured by a large volume summing detector, like SuN, which almost has a 4π coverage around the target. On an event by event basis, the γ-rays are summed into a total absorption spectra (TAS) which creates a single sum peak corresponding to the entry state energy. This is shown in a cartoon in Figure 3.7. The top half of the right side of the Figure 3.7 corresponds to using a small sized γ-ray detector and the bottom half corresponds to using a large volume detector like SuN. Smaller detectors can also be used to measure single γ-rays from a cascade instead of summing. If information is known about the nucleus and its decay it is possible to measure specific γ-rays in a cascade and still determine how much of the compound nucleus was created.

For example, if the $\gamma_{(2,1)}$ γ-ray in Figure 3.7 was known to be a dominant transition then measuring this γ-ray would also be a good estimate for calculating how many times this reaction took place [52].

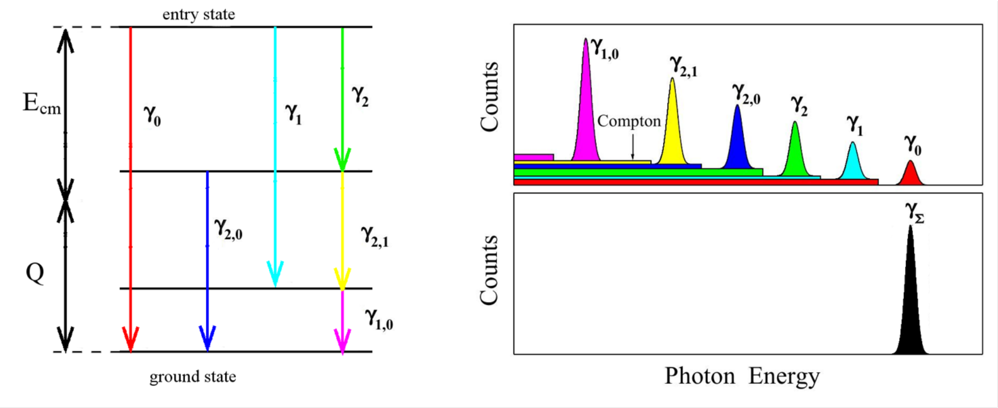

Figure 3.7: A cartoon example of the γ-summing technique. A compound nucleus will be excited to the entry state level and de-excite via γ-ray emissions to the ground state or long lived isomeric state. The summing technique will sum the γ-rays from each cascade into the sum peak, at the entry state energy, shown in black.

The Q-value for the ^{84}Kr$(p,\gamma)^{85}$Rb reaction is 7.016 MeV. For a beam energy of 3.7 MeV/u and using the cartoon in Figure 3.7, the entry state energy would then be 10.7 MeV. The excited ^{85}Rb compound nucleus would then decay from the 10.7 MeV energy state. The γ-summing technique will show this energy level as a single sum peak, the bottom half of the figure, when looking at a TAS spectrum. Since SuN has optically isolated segments, it is also possible to look at the individual γ-rays in the cascade in a spectrum called the Sum of Segments (SoS), the top half of the figure and similar to having a small size detector. The most important part and the most difficult part to this analysis is estimating the summing efficiency of the detector used and this process will be discussed in Chapter 5

3.3 Inverse Kinematics

Most of the previous p-process measurements have been done in forward kinematics. For forward kinematics there is a light beam impinging on a heavy target. If this work was done in forward kinematics there would have been an ^{84}Kr target with a proton beam. However, most of the p process reactions in the p process reaction networks are on radioactive isotopes. Techniques using forward kinematics with proton, neutron, α and γ beams are limited to reactions on long lived isotopes that can be fabricated into a target. Experiments with radioactive targets can be impossible to perform depending on the half life of the target. While running in inverse kinematics provides different challenges, it allows radioactive isotope measurements to be performed. A cartoon example of an inverse kinematics experiment is shown in Figure 3.8. This experiment provided a secondary bonus of creating a benchmark with this new experimental technique with a stable beam before applying it to radioactive beams. SuN has been previously used for inverse kinematics experiments without the hydrogen gas cell with good agreement to previous measurements [48].

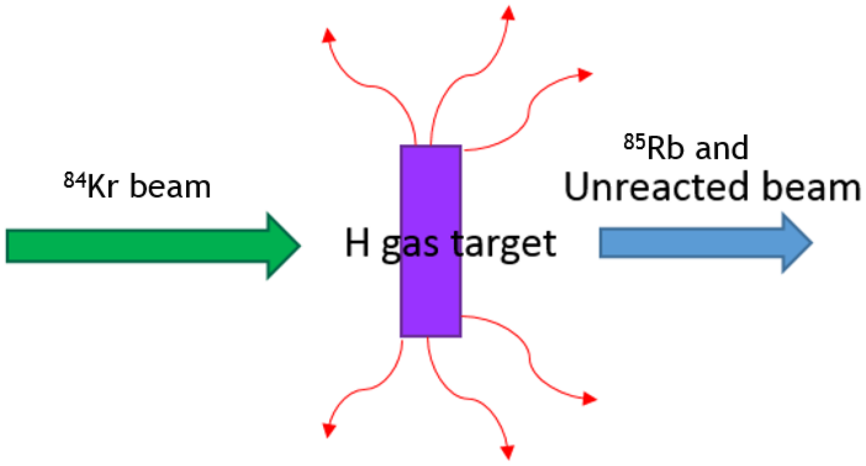

Figure 3.8: Shows a cartoon of an inverse kinematics setup where a heavy beam, ^{84}Kr, impinges a light hydrogen gas target.The red lines represent the γ-rays from the de-excitation of the compound nucleus.

Inverse kinematics techniques have previously been used with recoil mass separators with arrays like DRAGON at TRIUMF [53]. A heavy isotope beam impinges on a light target, usually hydrogen or helium gas, and the reaction products and unreacted beam pass through a series of magnets and electric fields to separate them. Measuring heavier isotopes with this technique is harder because separation is more difficult. This technique has been used to successfully measure (p,γ) and (α, γ) cross section reactions. Storage rings, like ESR at GSI, can also be used to measure reactions in inverse kinematics [54]. For this technique, a heavy isotope beam is injected into a large ring where the nuclei orbit. Within the ring, there is a target chamber with a hydrogen or helium target where the beam interacts. The reaction products will have different mass and charge to the original beam and can be detected.

This thesis work uses the inverse kinematics technique but has a hydrogen gas target placed at the center of SuN where the heavy beam interacts. This provides a new analysis complication in the detection of the γ-rays: the Doppler effect. In forward kinematics the beam is much lighter than the target so the products are created and decaying at a stationary point without a recoil velocity. In inverse kinematics the beam has enough velocity that after interacting with the light target the products do not stop. The products will have a recoil velocity and thus the emitted γ-rays are being emitted from a moving source. Because the γ-rays are coming from a moving sources, the γ-rays detected in the forward direction will appear higher in energy than if emitted at rest and γ-rays in the backwards direction will appear lower in energy than is emitted at rest. A Doppler correction must then be applied to every γ-ray that is measured. This correction will be discussed in more detail in Section 4.2.

Chapter 4

Calibrations and Background Subtraction

4.1 Gain Matching and Calibrations

First part of the analysis process is gain matching the PMTs in the SuN and SuNSCREEN detectors. SuN is gain matched with the background radiation peak from potassium-40, ^{40}K. Figure 4.1 shows the fitting of the ^{40}K background peak for the bottom segment PMTs of SuN. Background radiation is used for gain matching because it interacts with each of the segments from the outside of the detector. This eliminates the position dependence of the light collected by the three PMTs in each segment. If the gain matching is not done well it will affect the energy resolution of the summed spectra because the centroids of the background PMT peaks are slightly offset. After summation, the peaks which aren't properly aligned will create an artificially wider sum peak which worsens the detector's energy resolution. Once an hour long background run is taken the spectra are fit with a Gaussian to find the centroid of the ^{40}K background peak in each PMT, as shown in Figure 4.1. The centroid from a center PMT is chosen arbitrarily as the ”correct” channel and multiplicative factors are calculated to adjust the high voltages applied to each PMT. This allows for an initial correction in the hardware to align the ^{40}K background peak with the high voltages and a more accurate correction is applied later in the software.

Once the gain matching is completed with the high voltage adjustments for each PMT, the thresholds must also be adjusted. A ^{241}Am source is used for this purpose because it emits a strong low energy γ-ray at 59.6 keV. The source is placed at the center of each segment and statistics are collected until a clear peak can be seen sitting on top of the low energy background. No fitting is required for the thresholds and they are raised or lowered in the hardware for each PMT in order to ensure that the entire shape of the ^{241}Am γ-ray can be seen above the background. If the thresholds are too low the data acquisition system can get overwhelmed with low energy background and if the thresholds are too high it will cut out real signals.

Everything prior to this point are adjustments made to the hardware. After those adjustments are made, the gain matching is redone through software and the calibrations are applied from source measurements. After the gain matching and thresholds are complete, the three PMTs from each segment are summed leaving eight summed segment spectra. The calibrations for SuN are applied on a segment by segment basis from source measurements taken from the center of the detector. Sources used for calibrations are ^{241}Am, ^{60}Co, ^{137}Cs and ^{228}Th. ^{137}Cs is used as a relatively low energy calibration point as it emits a single γ-ray at 661 keV. ^{228}Th has multiple γ-rays over a larger energy range which is useful for having a better overall calibration. Lastly, ^{60}Co is doubly helpful since it emits two simultaneous γ-rays at 1173 keV and 1332 keV. This source can also be used to check the coincidence window within SuN to be confident that the summation is working correctly. Each source is placed in the center of SuN for a half hour to accumulate statistics. The gamma peaks are fit with Gaussians to find the channel centroids. The channel number is then compared

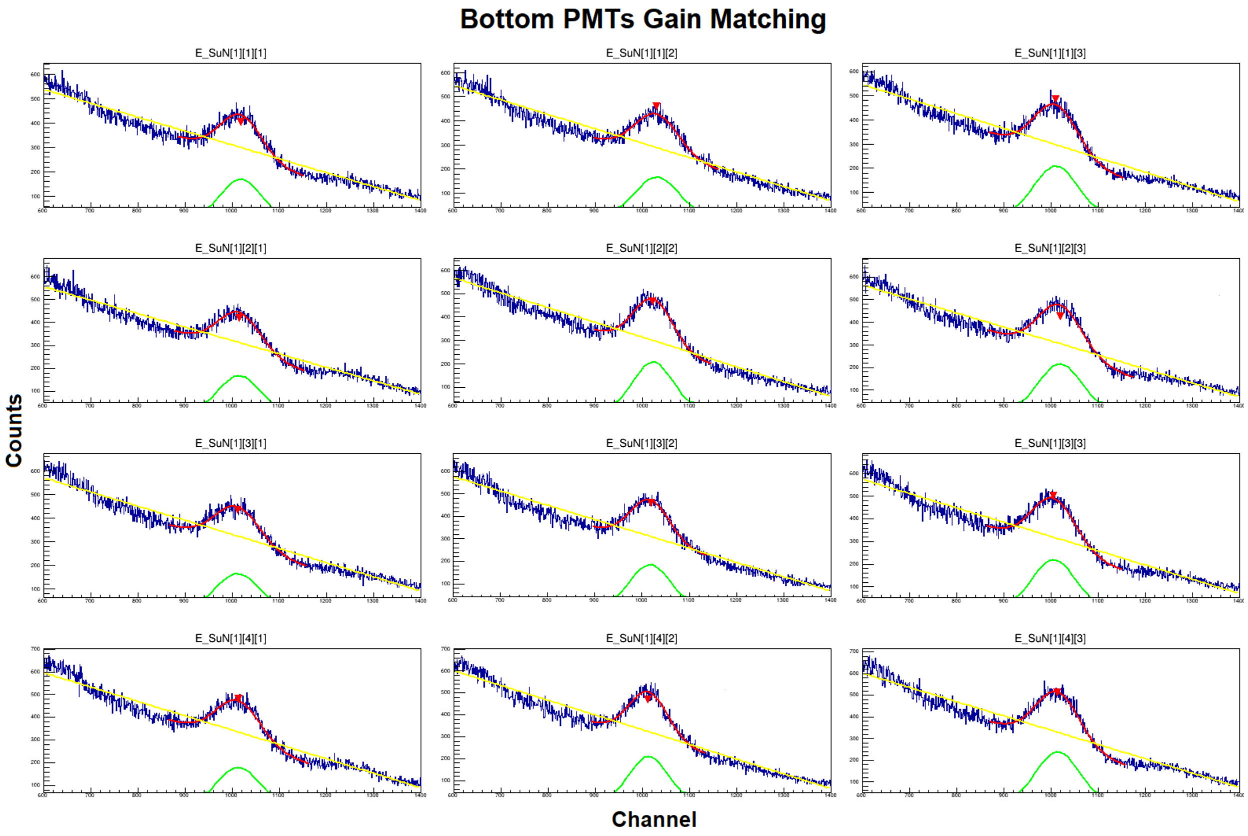

Figure 4.1: Shows the bottom segment PMTs of SuN and their gain match fitting. Gaussians are fit on the centroid of the ^{40}K background peak for each PMT. The centroid of a center PMT is chosen and multiplicative factors are calculated to shift the other PMT centroids to the same channel. E[0][1][1] refers to a specific PMT. The first bracket is top or bottom half, the second bracket is the segment and the last is the PMT within that segment.

to the actual energy values of each gamma ray. An example for the ^{60}Co source spectra is shown in Figure 4.2. It is important to get sources that can span a wide energy range. With more energy points the calibration will be more accurate. For this data a quadratic energy calibration was used from the ^{241}Am, ^{60}Co, ^{137}Cs and ^{228}Th sources.

Once SuNSCREEN is lowered into position above SuN, SuNSCREEN also needs to be gain matched and thresholds need to be checked. In order to lower the noise from the PMTs and to reduce noise induced veto counts, the front PMT signals are gated on the back PMT signals. SuNSCREEN is left on for an hour to gather background statistics and the gain matching is applied on the low energy room background peaks.

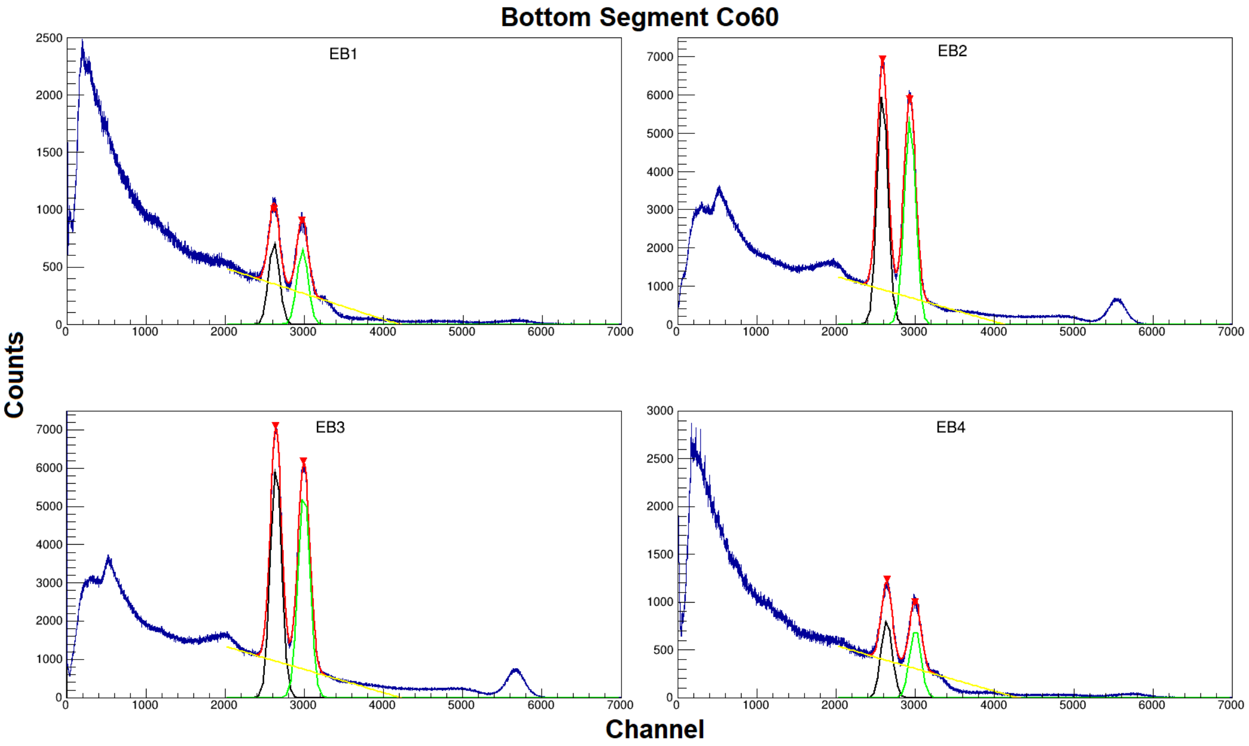

Figure 4.2: Shows the four bottom segment ^{60}Co source runs. The two lower peaks are the 1173 keV and 1332 keV γ-rays. The higher energy peak is the occasional instance where the two γ-rays are summed within the same crystal to see the 2505 keV γ-ray.

4.2 Sum Peak

When the beam, ^{84}Kr, and target, hydrogen gas, interact they populate an excited entry state within the compound nucleus, ^{85}Rb, before it decays by emitting γ-rays which are collected and measured by SuN. These γ-rays are summed event by event into a total absorption spectra (TAS). In the TAS a sum peak appears at the entry state energy of the compound nucleus. The sum peak energy and the entry state energy is the sum of the Q-value for the reaction and the center of mass beam energy. The Q-value for the $^{84}\mathrm{Kr}(p,\gamma)^{85}\mathrm{Rb}$ reaction is 7.0 MeV and the sum peak in this experiment was at an energy of 9 - 10 MeV depending on the beam energy. The number of counts in the sum peak is directly related to the cross section of the reaction since each count represents a γ-ray cascade from the excited

^{85}Rb nucleus. The number of counts corrected for the summing efficiency of the detector give how many times this reaction occurred.

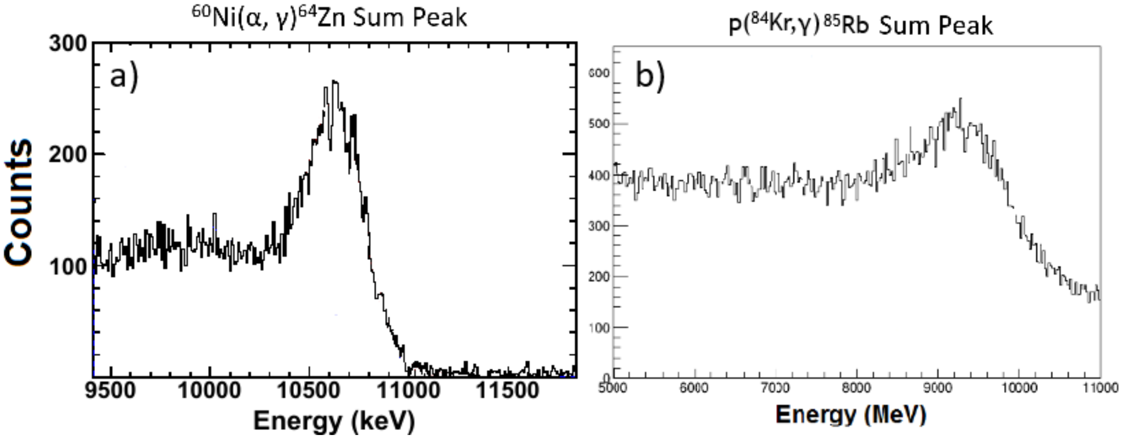

Figure 4.3: Shows a forward kinematics sum peak from the ^{60}Ni$(\alpha, \gamma)^{64}$Zn experiment and a reverse kinematics sum peak from the ^{84}Kr$(p, \gamma)^{85}$Rb experiment at 3.7 MeV.

The sum peak for the highest beam energy is shown in Figure 4.3 alongside the sum peak from a forward kinematics experiment of the ^{60}Ni$(\alpha, \gamma)^{64}$Zn reaction. Both peaks are asymmetrical at lower energies due to incomplete summation of the γ-rays during the γ-summing process and occurs for both forward and inverse kinematics experiments. In some cases, generally for higher energy γ-rays, some of the energy is not deposited into the NaI crystals and is instead scattered outside of the detector.

Because of the use of inverse kinematics in this thesis work, the sum peak for this experiment was much wider than a typical forward kinematics experiment. There are two main factors attributing to the shape of the peak: the Doppler correction and energy straggling through the gas cell.

In inverse kinematics the compound nucleus will have a recoil velocity since the beam is much more massive than the target. Because this compound nucleus is moving as it decays the resulting γ-rays from the decays are being emitted from a moving source. A moving γ-ray that is detected in the forward direction will appear to have more energy than if detected at

Beam Energy (MeV/u)	CoM Energy After Foil (MeV/u)	β
3.7	3.09	0.0810
3.4	2.79	0.0759
3.1	2.48	0.0719
2.8	2.18	0.0662

Table 4.1: Shows the calculated β values using Equation 4.1 for the Doppler correction for each beam energy and the calculated center of mass (CoM).

rest and a γ-ray that is detected in the backward direction will appear to have less energy than if detected at rest. This is known as the Doppler effect and must be corrected for in the analysis. This correction is applied on a segment by segment basis to the deposited energy before summing. The shift in energy is dependent on both the initial beam energies and the angle of the γ-ray emission. Table 4.1 shows the calculated center of mass energy of the beam and target as well as the associated β values. β is calculated in the typical way

$$\beta = \sqrt{1 - \frac{1}{\gamma^2}} \tag{4.1}$$

where γ is the center of mass energy shown in 4.1 and is calculated with Equation 3.1.

Once the original value for β is calculated it also needs to be corrected for the angle of the incoming γ-ray. The angles used for this analysis were taken from Steven Quinn's thesis [17]. A set of GEANT4 simulations were performed to determine the average emission angle for the γ-rays that deposit energy into each NaI crystal and these angles are used for the Doppler correction. The angles for each segment are input into Equation 4.2 for each beam energy

$$\gamma' = \gamma(1 - \beta cos(\theta)) \tag{4.2}$$

where γ' is the Doppler corrected energy, γ is the original energy, β is calculated depending on the beam energy, γ from Equation 4.1 and θ depends on the segment with the values listed in Table 4.2. The "Correction Factors" listed in Table 4.2 refers to the $1 - \beta cos(\theta)$ factor from Equation 4.2 which changes for each segment based on the angle. These angles were calculated by Steve Quinn per segment and those results are listed in 4.2 [17]. Multiplying the original γ-ray energy by this correction factor gives the final Doppler corrected energy.

Segment	Angle (°)	Correction Factors
1	2.559	1.0711
2	2.024	1.0388
3	1.118	0.9677
4	0.592	0.9358

Table 4.2: Shows the angles used in the Doppler correction from Steve Quinn's thesis for each segment of the SuN detector [17]. It also shows the correction values for each segment for the highest beam energy, 3.7 MeV/u with $\beta = 0.0810$.

After applying the correction for the Doppler shift the sum peak is still wider than a typical forward kinematics experiment because of the gas cell target. For astrophysics experiments, the beam energies that correspond to the Gamow Window are quite low which causes the beam to lose more energy through the gas cell window and the gas within the cell. Figure 4.4 shows the experimental target used for this experiment which has a thick tantalum washer on the face to stop the beam before it can interact with the plastic cell behind the ring. The beam must go through the thin molybdenum foil and then through the gas of the cell which was at a pressure of 650 Torr. As the beam moves through the foil it loses energy and as it moves through the gas it will continue to lose energy. Depending on where in the cell the reaction occurs, the entry state energy will change which causes the sum peak to widen.

Looking back to Figure 3.7, the sum peak appears at the entry state energy of the compound nucleus which is the beam energy plus the Q-value. The Q-value remains constant but depending on where the beam interacts within the cell the beam energy is changing.

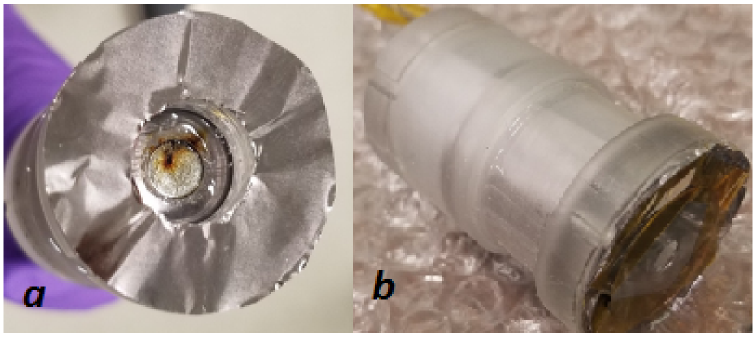

Figure 4.4: Two different views of the gas cell target that was filled with hydrogen gas at the center of SuN. (a) shows the front face of the cell and (b) shows the side of the cell.

Beam Energy (MeV)	After Foil (MeV)	After Half Cell (MeV)	CoM (MeV)
3.7	3.096	2.815	2.782
3.4	2.791	2.513	2.484
3.1	2.487	2.206	2.180
2.8	2.088	1.990	1.967

Table 4.3: Shows the energy loss of the beam through different sections of the gas cell: the molybdenum foil window and half of the gas within the gas cell. The energy loss is directly related to the width of the sum peak. There is also energy straggling of approximately 0.003 MeV.

Instead of populating a single entry state multiple entry states are being populated which leads to the wider sum peak. Table 4.3 shows the beam energies at various points through the gas cell. The majority of the energy loss occurs when the beam passes through the thin molybdenum foil. A 2 μm foil was chosen because it was thick enough to hold the desired 650 Torr pressure but also thin enough to reduce the energy loss. As the energy of the incoming beam decreases the expected cross section for the reaction decreases exponentially so it is imperative to reduce the energy as much as possible while still being able to hold pressure within the cell. The wide shape of the sum peak for this experiment posed a new problem for the analysis. A new analysis technique for this setup was designed and validated with previous SuN data and will be discussed in Chapter 5.

4.3 Background Subtraction

Background subtraction was a very important part of the analysis. For future experiments with radioactive beams this will be even more important as beam rates and are much lower than the rates seen for this experiment. This analysis had two types of backgrounds to eliminate: room background or cosmic rays and beam induced background from the gas cell. By using SuNSCREEN, a pulsed beam and running with the gas cell full and empty both types of background could be isolated and subtracted.

SuNSCREEN is a form of active shielding for SuN developed at Hope College [43]. A cosmic ray with enough energy will hit SuNSCREEN, escape, and hit SuN. If these two events occur in coincidence then the event in SuN can be ignored as a cosmic ray event. This technique reduces the overall room background by a factor of six.

The beam was pulsed for this experiment using the EBIT charge buncher [44]. Using a pulsed beam, it is possible to isolate almost all of the room background that remains after removing the vetoed events from SuNSCREEN. A cartoon of the beam time structure and the gates is shown in Figure 4.5.

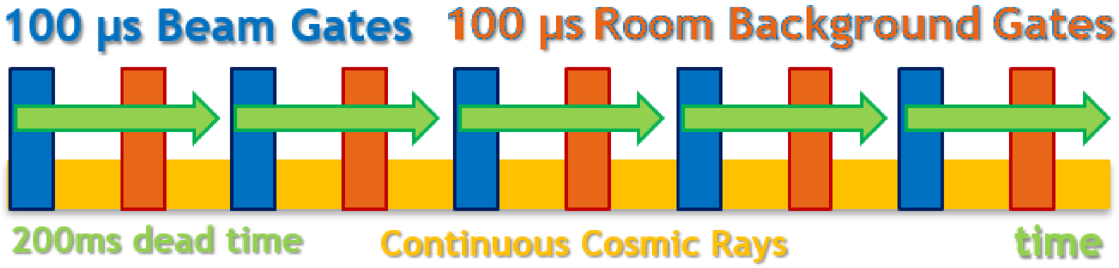

Figure 4.5: A cartoon of the beam time structure and the time gates to isolate cosmic background. With time going from left to right, yellow represents the continuous cosmic ray background, the green arrows represent the 200 ms of dead time between each blue 100 μs beam gate. The orange boxes are the same 100 μs gates shifted in time by 100 ms which should only be room background.

The beam was pulsed in 100 μs pulses separated by 200 ms of dead time. In Figure 4.5, the blue rectangles are the 100 μs beam pulse gates, the green arrows are the 200 ms of dead time, the orange rectangles are 100 μs room background gates also separated by 200 ms. The orange room background gates are the same length as the beam pulse gates but are offset by 100 ms to ensure that they only capture room background counts and no beam events. For every pulse cycle, represented by the green arrows, there will be two sets of 100 μs of data collected. The blue pulses collect all the good events for the reaction with a small amount of room background and the orange gates collect an equivalent time's worth of room background. Having each pulse be the same length of time ensures that the cosmic background accumulated in each pulse should be the same magnitude. The background counts collected in the orange time pulses are then subtracted from the counts in the blue time pulses leaving the spectra with only the good events and beam induce background with the gas cell.

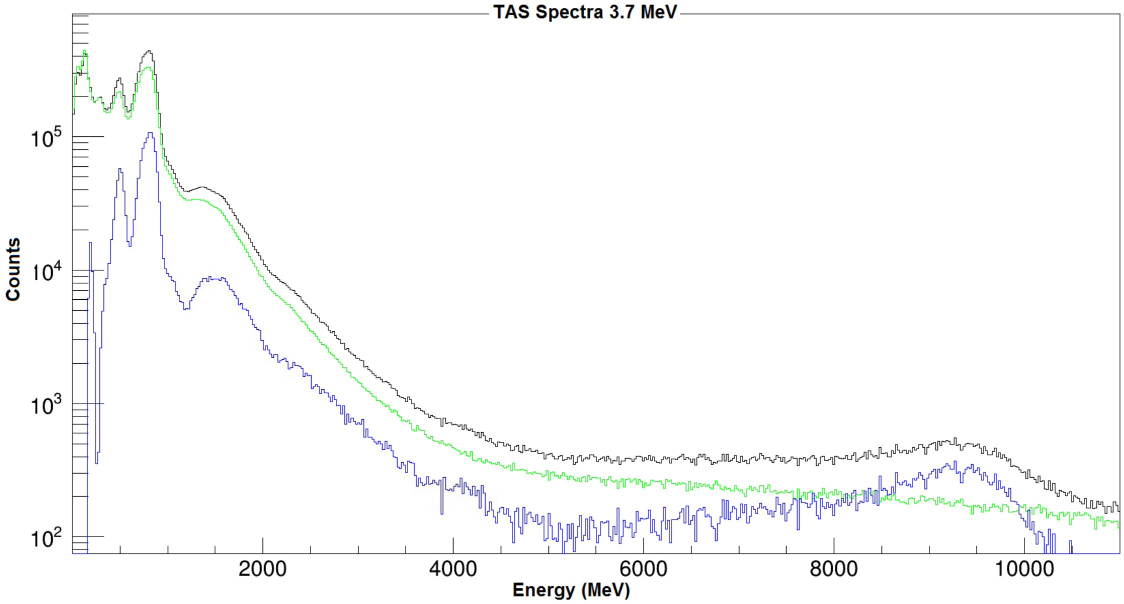

Figure 4.6: Shows the 3.7 MeV sum peaks before and after background subtraction. The black line is the original sum peak, green are the scaled empty cell runs and blue is the fully subtracted spectra.

In order to isolate the remaining beam induced background from the gas cell two sets of runs were taken for each energy: full cell runs and empty cell runs. Data was taken with the cell full of hydrogen gas and empty of hydrogen gas. All of the data for the full and empty cell runs at each energy are summed together and then the empty cell data is scaled based on the total amount of beam charge deposited for the full and empty runs. The beam current was monitored for the duration of the experiment for both full and empty runs. Once the scaling was complete the empty cell runs are subtracted from the full cell runs.

Figure 4.6 shows the spectra for the highest beam energy, 3.7 MeV. Black is the original room background subtracted spectra with the SuNSCREEN vetos and the background gates applied, green is the scaled empty cell runs and blue is the final subtracted spectra. When the beam interacts with the plastic or the glue in the cell it creates a large amount of background from fusion evaporation reactions that can hide the sum peak. After the subtraction the shape and definition of the sum peak become more obvious.

At the low energies there are still counts present in the fully background subtracted peak. After scaling, the two spectra are subtracted with up to as many as 10^6 counts per bin. Statistical fluctuations would allow for up to 1000 counts per bin within uncertainties but there could be other reasons for background counts. When the gas cell is empty the energy straggling of the beam through the front foil and how the beam interacts with the cell and the back foil will be different than when the gas cell is full. The beam will not be losing energy through the gas and will have more energy when interacting with the cell and back foil which will create slightly different spectra. Another possibility is that some background is still coming in coincidence adding lower energy counts. However, in the energy region of the sum peak the subtraction is quite good.

All of the data for each energy was analyzed with these background subtraction techniques. The data for each energy for the full and empty cell runs were summed into a single spectra after applying the SuNSCREEN veto and the background gate subtractions. The empty cell runs were scaled based on the total deposited beam current and then subtracted from the full cell runs to give the final spectra for each energy. The blue line in Figure 4.6 is the fully Doppler corrected and fully subtracted sum peak for the 3.7 MeV beam energy. The next step of the analysis process is replicating this sum peak with simulations using RAINIER and GEANT4 in order to extract the summing efficiency of SuN for each beam energy.

Chapter 5

Analysis

When the compound nucleus, ^{85}Rb, decays from its excited state it will emit a γ-ray cascade whose energy sums to the excited entry state. These cascades can have different multiplicities with γ-rays of various energies but they will always sum to the entry state energy. Each γ-ray will have a different efficiency of being detected by SuN based on the energy and the number of segments of SuN that fired and recorded the event. This relationship is not known for this new experimental setup but is very well known for the typical SuN experimental setup. Since it is not well known for this experimental setup a new simulation method was developed and validated with previously published data to calculate SuN's efficiency.

5.1 Efficiency Validation

In order to validate this new analysis technique, it was first performed on a previously published data set, the ^{90}Zr(p,γ)^{91}Nb cross section. This data was measured with SuN and analyzed with the traditional efficiency technique [46]. To accurately simulate the efficiency of SuN a two step simulation process is proposed. Using both the RAINIER and GEANT4 codes, simulations are matched to the experimental data and the efficiency is extracted from the simulations. RAINIER accounts for the physics of the decaying compound nucleus and GEANT4 accounts for the detector response [55] [56].

5.1.1 RAINIER

The first step of the simulation process is understanding the γ-ray cascades from the excited compound nucleus as these cascades define the γ-ray multiplicity which subsequently impacts the summing efficiency of SuN. RAINIER is a statistical model code that simulates the γ-ray cascades from an excitation energy of the compound nucleus [55]. The resulting energies and multiplicities of the γ-ray cascades are very important as SuN's efficiency is dependent on both. Figure 5.1 shows a cartoon example of various possible cascades from a compound nucleus at an entry state energy, E_{es}. RAINIER must be run at the specific excitation energy, E_{es}, that corresponds to the energy of the sum peak. The cascades depend on the choice of nuclear level density and γ-ray strength function and for this reason a systematic investigation of both parameters is required. The level densities and γ-ray strength functions will be discussed in more detail in Sections 5.1.1.1 and 5.1.1.2.

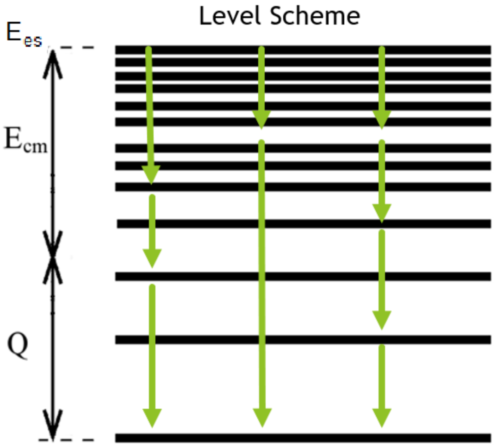

Figure 5.1: Shows a cartoon example of the γ-ray cascades from an excited compound nucleus. The energy and multiplicity of the cascades will change depending on the input parameters used in RAINIER.

The first step of the new analysis technique is testing multiple input parameters in RAINIER to find the best match for the experimental data. The most important parameters to change were the level density (LD) and γ-ray strength function (GSF) parameters for these particular reactions. The next sections will briefly go over the various models and their inputs.

5.1.1.1 Level Densities

The LD is a measure of how many levels there are in the compound nucleus in a certain energy range and at a certain excitation energy. As the excitation energies increase the level density goes from a discrete set of levels to a continuum where the levels begin to overlap. Having an incorrect level density in the simulations would alter the multiplicities and could change the overall shape of the sum of segments spectra. If the level density is too low there would be more higher energy γ-rays with a lower multiplicity and if the level density is too high there would be more lower energy γ-rays with a higher multiplicity.

There are two different models in RAINIER that can be chosen: the Constant Temperature Model (CTM) or the Back-Shifted Fermi Gas Model (BSFG) [57] [58]. The simpler of the two is the CTM which has the form

$$\rho_{CTM} = \frac{\rho_0}{T} e^{E/T} \tag{5.1}$$

where $\rho_0 = (1/T)e^{E_0/T}$, E is the energy and T is the temperature [59]. The temperature and E_0 can be altered to change the level density to better match experimental data for certain nuclei. The BSFG model has the form

$$\rho_{BSFG} = \frac{e^{2\sqrt{a(E-E_0)}}}{12\sqrt{2}a^{1/4}(E-E_0)^{5/4}} \tag{5.2}$$

where a and E_0 are free parameters that can be altered to help match experimental data. Both of these models were examined in this work for the simulation process.

5.1.1.2 γ-ray Strength Functions

The γ-ray strength functions determine the probability of the compound nucleus decaying via specific γ-rays. Having an incorrect strength function will also alter the multiplicity and energy of the γ-rays in the simulation. In RAINIER the user can select different γ-ray strength functions: E1, M1 and E2. These transitions arise from selection rules where E_i are electric transitions and M1 is a magnetic transition. For this reaction the E2 transitions do not have a large effect for these reactions and were not altered from the default. E1 can be either the Standard Lorentzian [60] [61], General Lorentzian [62], the Kadmenskij Markushev Furman model (KMF) [63] or the Kopecky Chrien model (KOP). M1 emissions are typically described as a Standard Lorentzian with or without an upbend. Figure 5.2 shows an example of a nucleus which has an upbend in the γ-ray strength function. This was data taken with the SuN detector and there is a clear upward trend in the γ-ray strength function at lower energies [64]. It is currently unknown if the upbend corresponds to an E1 or M1 transition but in RAINIER it is assumed to be M1.

The Brink-Axel standard Lorentzian is written as a giant dipole resonance shape:

$$f_{\chi l}(E_\gamma) = K_{\chi l} \frac{\sigma_{\chi l} E_\gamma \Gamma_{\chi l}^2}{(E_\gamma^2 - E_{\chi l}^2)^2 + E_\gamma^2 \Gamma_{\chi l}^2} \tag{5.3}$$

where $\sigma_{\chi l}$ is the strength, $E_{\chi l}$ is the energy and $\Gamma_{\chi l}$ is the width of the giant resonance and where

$$K_{\chi l} = \frac{1}{(2l+1)\pi^2 \hbar^2 c^2}. \tag{5.4}$$

For the γ-ray strength functions it is important to have the correct parameters for the strength, energy and width of the giant resonance for the compound nucleus being simulated.

These resonances can be used for both the E1 or M1 transition but the M1 may also have an upbend correction.

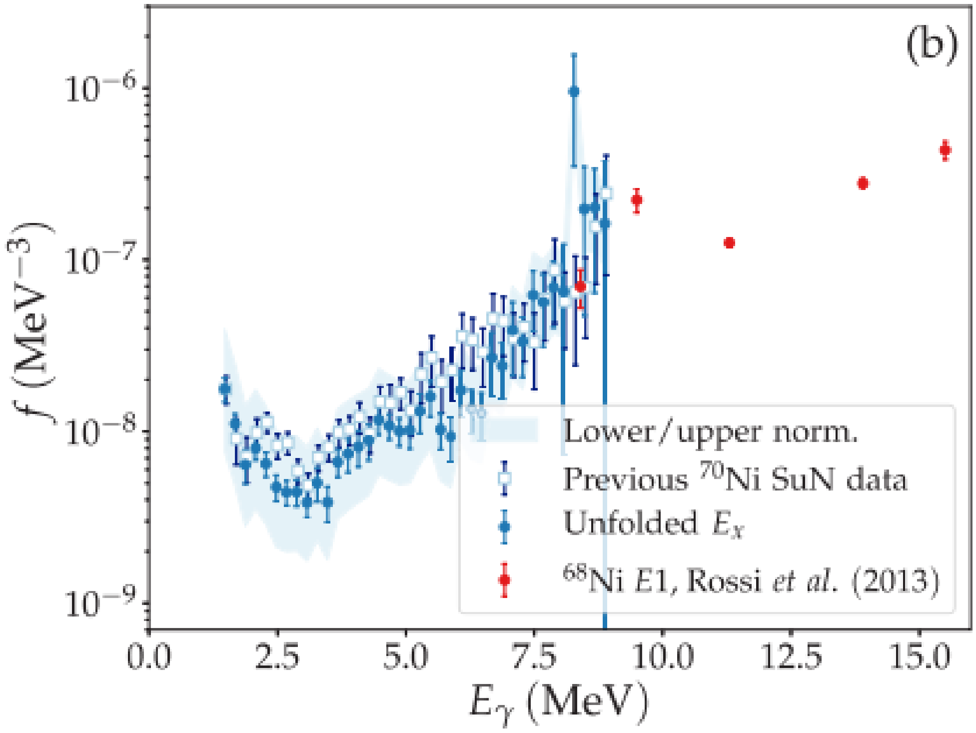

Figure 5.2: Shows the ^{70}Ni γ-ray strength function [64]. Notice at lower energies there is an upward trend or an upbend.

5.1.2 ^{90}Zr(p,γ)^{91}Nb Comparison

In Figures 5.3 and 5.4, various simulation inputs from RAINIER are shown compared to the experimental data, in black, for the ^{90}Zr(p,γ)^{91}Nb cross section.

Color	Level Density	E1 Model	M1 Model
Red	BSFG	KOP	no Upbend
Light Blue	CTM	KOP	no Upbend
Yellow	BSFG	KOP	Upbend
Dark Blue	BSFG	Standard Lorentzian	no Upbend
Pink	CTM	KMF	no Upbend

Table 5.1: Lists the input parameters for the various colors in Figures 5.3 and 5.4.

Table 5.1 shows the input parameters used in the various colors found in Figures 5.3 and 5.4. The red line has a "default" set of simulation parameters: BSFG level density, E1 is the KOP model and M1 has no upbend. The others are all changing one thing to show a handful of the different options. These are not all the different inputs that were looked at but gives a sample of the simulations.

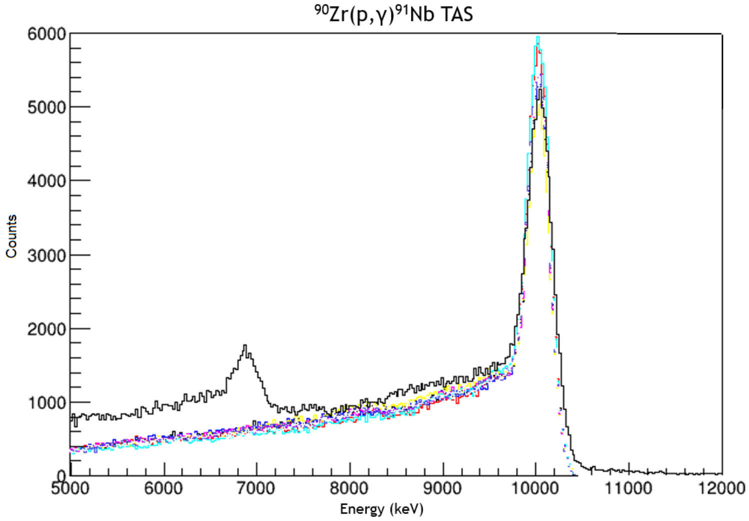

Figure 5.3: Shows the ^{90}Zr(p,γ)^{91}Nb sum peak from a previously published data set with SuN. Black is the experimental data and the colors are various input parameters with RAINIER changing the level densities and gamma ray strength functions.

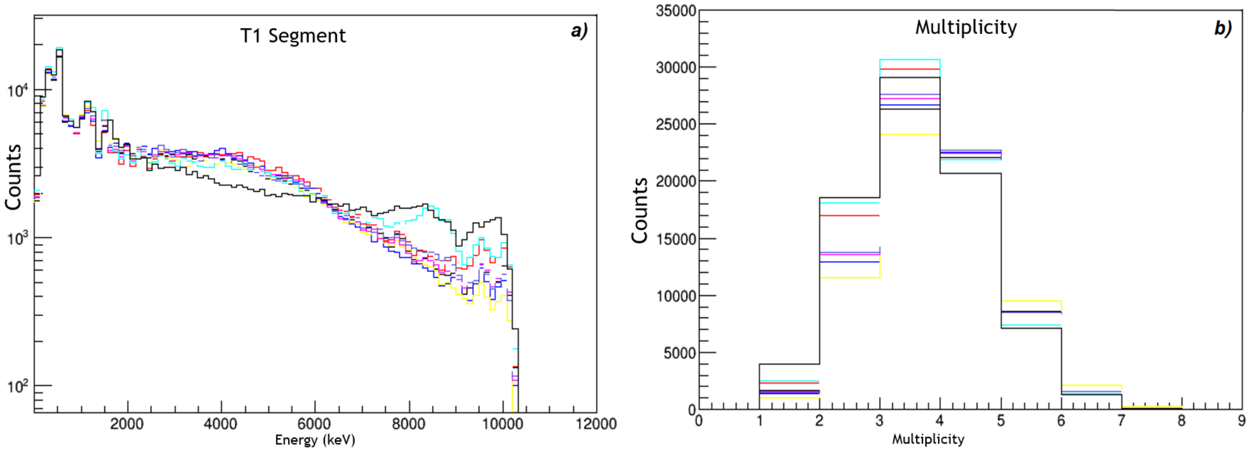

Figure 5.4: Shows the ^{90}Zr(p,γ)^{91}Nb sum of segments, (b), and multiplicity, (c), gated on the sum peak in Figure 5.3 with the same colors.

For the validation process the default parameters for each model were not altered but for the ^{84}Kr(p,γ)^{85}Rb analysis they were altered and considered in more detail. The TAS spectra shown in Figure 5.3 shows the experimental data for the ^{90}Zr(p,γ)^{91}Nb reaction in black and various combinations of the previously listed simulation inputs. The peak at approximately 7 MeV is from a background reaction with the proton beam and fluorine. It is not relevant to the simulations as the segments and multiplicity are gated on the energy range of the sum peak. The Sum of Segments (SoS) spectra shown in (a) of Figure 5.4 and the multiplicity spectra in (b) are more sensitive to the level density and γ-ray strength function. Notice in these example parameters, the simulations are too low at the higher energies and too high around 4 MeV. This is most likely due to the simulations having a level density that is too high. This would create more lower energy γ-rays with a higher multiplicity than higher energy γ-rays.

The final cross sections were calculated to validate the new analysis technique and compared to the previously published SuN data. The area under the TAS sum peak is calculated for the simulation from Figure 5.3 and compared to the number of events run in the simulation. This ratio gives the simulated efficiency of the SuN detector which is plugged into the cross section calculations. The cross section equation used in this work is

$$\sigma = \frac{A}{N\xi}\frac{1}{N_b}\frac{I}{\epsilon} \tag{5.5}$$

where A is the target mass, N is Avogadro's number, ξ is the target thickness, N_b are the beam particles, I is the number of times the reaction occurs and ϵ is the detector efficiency. In this case the simulated cross sections are used instead of the typical technique used by SuN described in the original ^{90}Zr(p,γ)^{91}Nb publication [46].

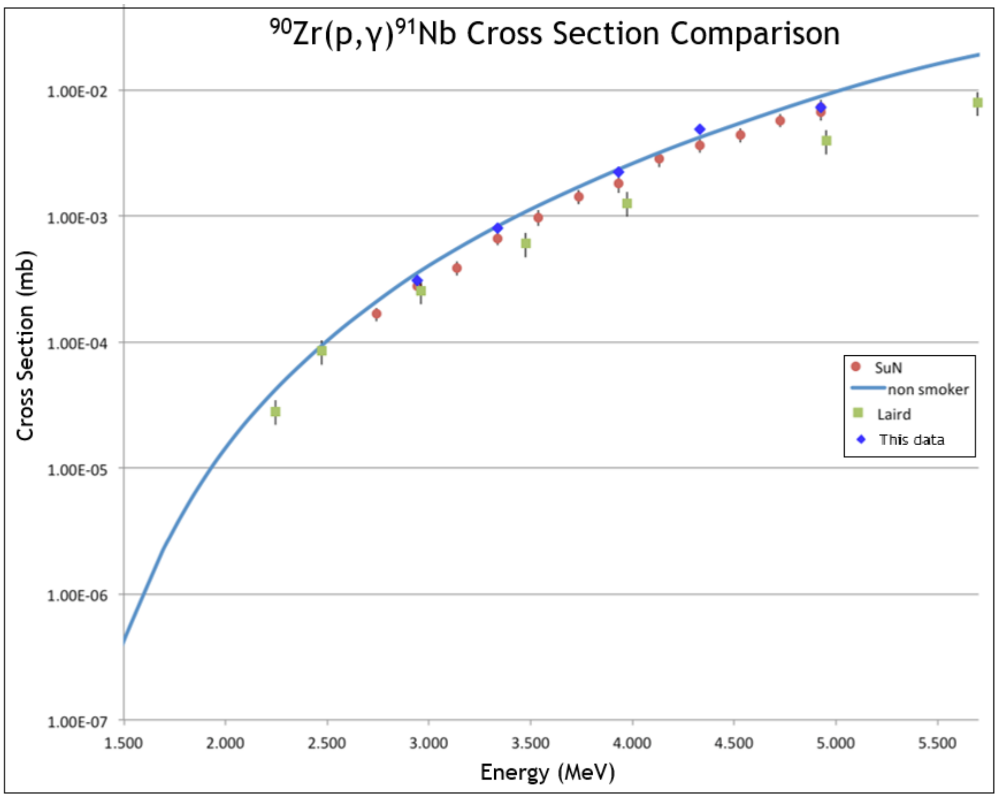

Figure 5.5: Shows the ^{90}Zr(p,γ)^{91}Nb cross section from the new analysis technique, dark blue diamonds, previously published SuN data, orange circles, previously published data from Laird, green squares, and the theoretical NON-SMOKER values [65].

Using the new cross sections, a comparison is made with the previously measured data and the NON-SMOKER theoretical values shown in Figure 5.5 [46]. The new cross section values from this technique are shown in dark blue diamonds, the previous SuN data is shown in orange circles and the NON-SMOKER values are the light blue line. The cross section values match well with each other and with the theoretical cross section values providing evidence that the new analysis technique works well.

5.2 GEANT4 Simulations

After validating the technique changes must be made to the GEANT4 SuN geometry to add the new hydrogen gas cell target into the center of the simulation. The code was also altered so that events were fired randomly from the entire volume of the gas cell instead of the center of SuN since the beam can react anywhere within the cell. The energy loss through the cell was accounted for through an additional analysis step which is outlined in Section 5.3.

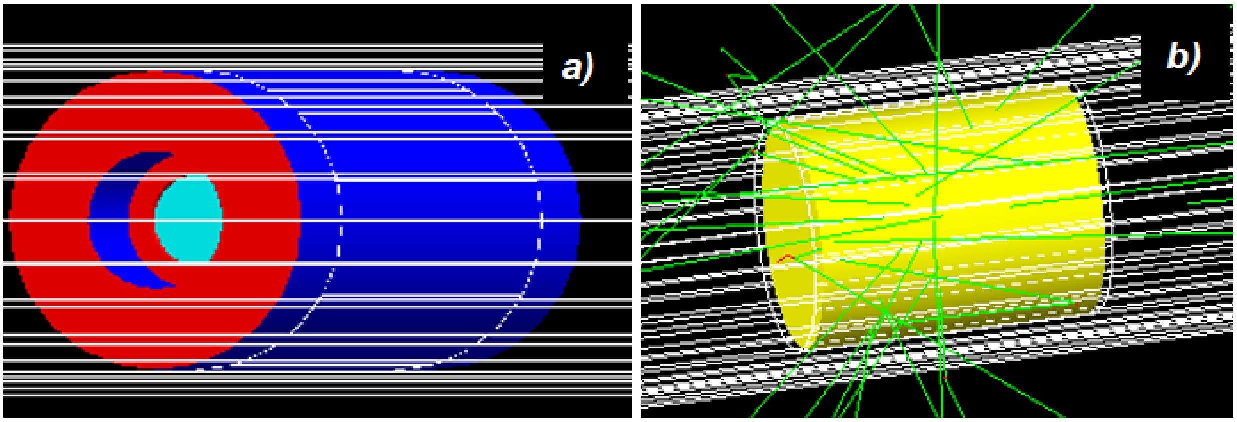

Figure 5.6: Shows the updated GEANT4 geometry of the gas cell placed in the center of the SuN detector. (a) shows the outside of the cell and (b) shows the inside of the cell.

Figure 5.6 shows the updated gas cell in GEANT4. (a) shows the outside of the cell with light blue being the thin molybdenum foil, red being the tantalum washer, and dark blue being the plastic. (b) shows the inside of the cell where yellow is the hydrogen gas and the green lines are the events being initiated from the entire volume of the gas cell. In order to lower the beam induced background, the inside of the cell is also coated with a thicker tantalum foil so that the beam is shielded from the plastic and unreacted beam cannot escape the gas cell as easily. That layer is not visible in Figure 5.6.

Lastly, the simulations were Doppler shifted since the experiment was run in inverse kinematics. Because the beam is heavier than the target the γ-rays will hit the lighter hydrogen nuclei and continue moving causing the γ-rays to be emitted by a moving source. The Doppler shift is applied in the GEANT4 simulations which also helps to broaden the simulated peaks and can be seen in (b) of Figure 5.7. (a) shows the original simulations from

GEANT4 which produces a much thinner sum peak. Figure 5.7 are only a single RAINIER parameter set at a single energy.

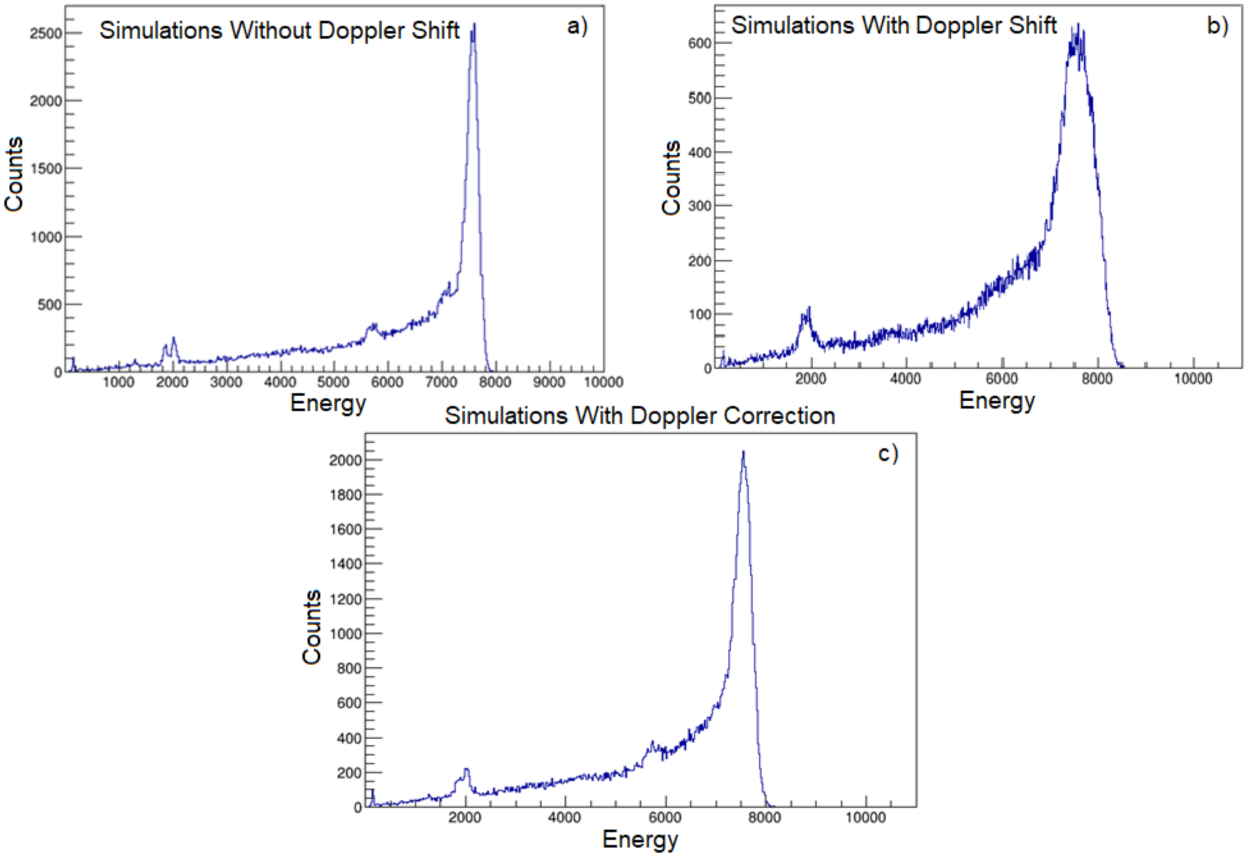

Figure 5.7: Shows the simulations (a) before the Doppler shift is applied, (b) with the Doppler shift and (c) after it is corrected. Notice that the final simulation in (c) is wider than the original since the correction process is not perfect.

The GEANT4 outputs shown in (b) of Figure 5.7 are then Doppler corrected in an identical calculation as the experimental data. This process is outlined in Section 4.2. The correction is only applied on a segment by segment basis and will not completely correct the Doppler effect. Part (c) of Figure 5.7 shows the final corrected simulation spectra. It is wider than the original simulated peak in (a) that was no Doppler shifted and corrected. This step helps to identify how much of the peak width can be attributed to the Doppler shift.

5.3 Chi Squared Fitting

As the beam passes through the molybdenum foil it loses a large amount of energy. The sum peak for this experiment is quite wide due to the energy loss in the target window, hydrogen gas and the Doppler shift. The expected energy loss at various points in the gas cell is given in Table 4.3. In order to account for the energy loss through the foil and gas in the simulations another step is added to the analysis process for the ^{84}Kr(p,γ)^{85}Rb cross section before extracting the detector efficiencies.

The initial RAINIER simulations were run at a specific entry state energy, $E_{es} = E_{beam} + Q$. Because there is a wide range of entry state energies due to the energy loss in the gas cell, RAINIER inputs were run at 15 different energies incrementing by 0.1 MeV over the expected energy loss range given in Table 4.3. All of these energy outputs are then run through a χ^2 minimization which simultaneously fits the TAS, SoS and multiplicity spectra. The results shows how much each entry state energy feeds into the total spectra which defines the simulated efficiency and recreates the wide sum peak.

Figure 5.8 shows an example of the χ^2 fitting results for one set of RAINIER inputs for the highest beam energy, 3.7 MeV. The red are the simulations and the black is the experimental data. Notice that the TAS is zoomed in closely around the sum peak in order to help constrain the fitting and since this is the only region of interest in this spectra. The SoS and multiplicity spectra are gated around the same energy range shown in the TAS spectra. This set of RAINIER parameters is the constant temperature model for the level density and the Kadmenskij Markushev Furman model for the E1 γ-ray strength function. Notice that this simulation has slightly too many counts in the higher energy range of the sum of segments spectra but overall is a good fit.

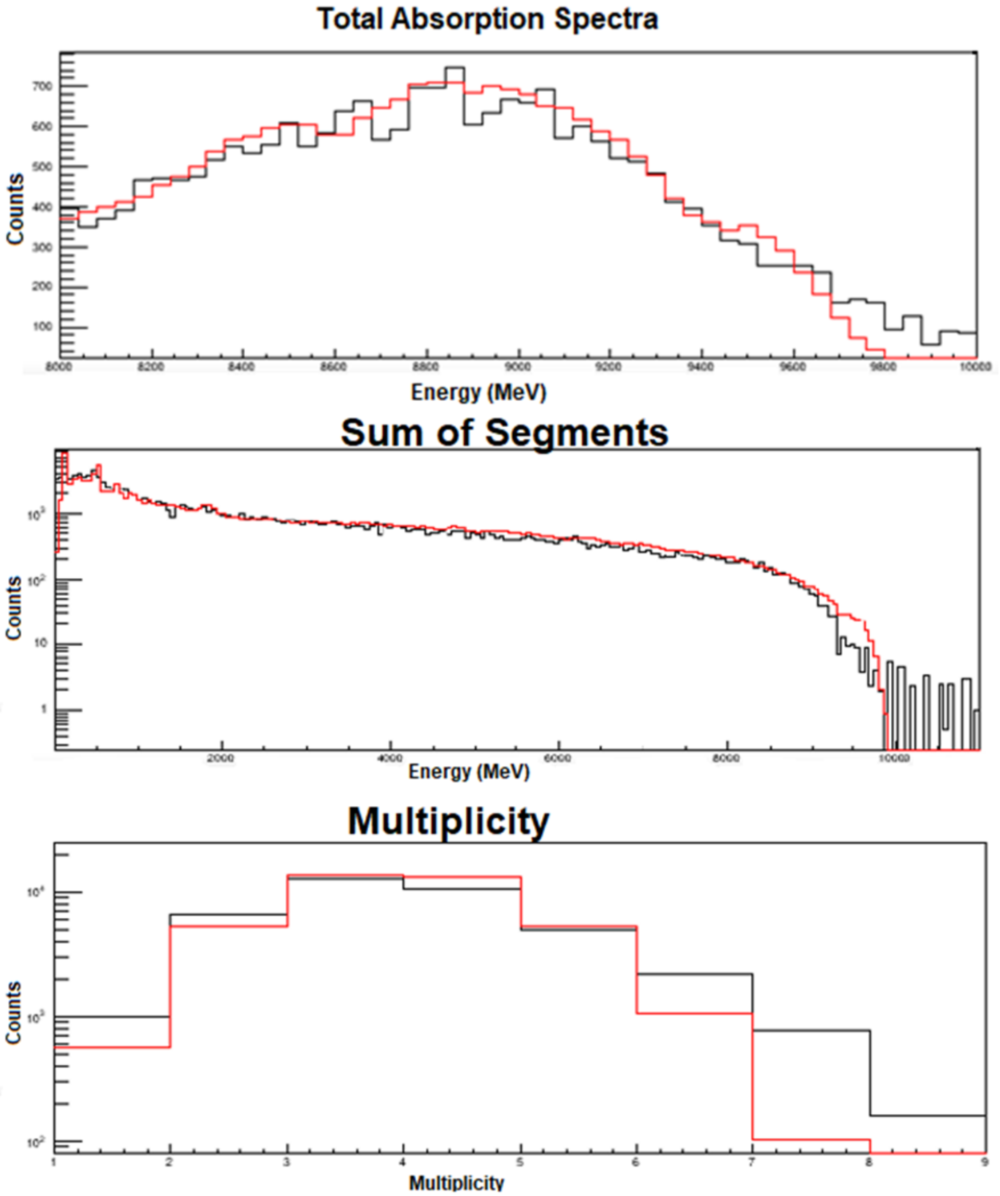

Figure 5.8: Shows the fitted TAS spectra centered around the sum peak, the fitted sum of segments gated on the sum peak and the multiplicity gated on the sum peak. Red are simulations and black is the experimental data for the highest beam energy 3.7 MeV.

To create these fits, all the entry state energies are summed and the TAS, SoS and multiplicities are fit simultaneously. The amount each of the entry state energies feeds into these spectra is called the feeding ratio. The feeding ratios for this fit and their uncertainty are shown in Figure 5.9. These feeding ratios are summed and multiplied by the number of

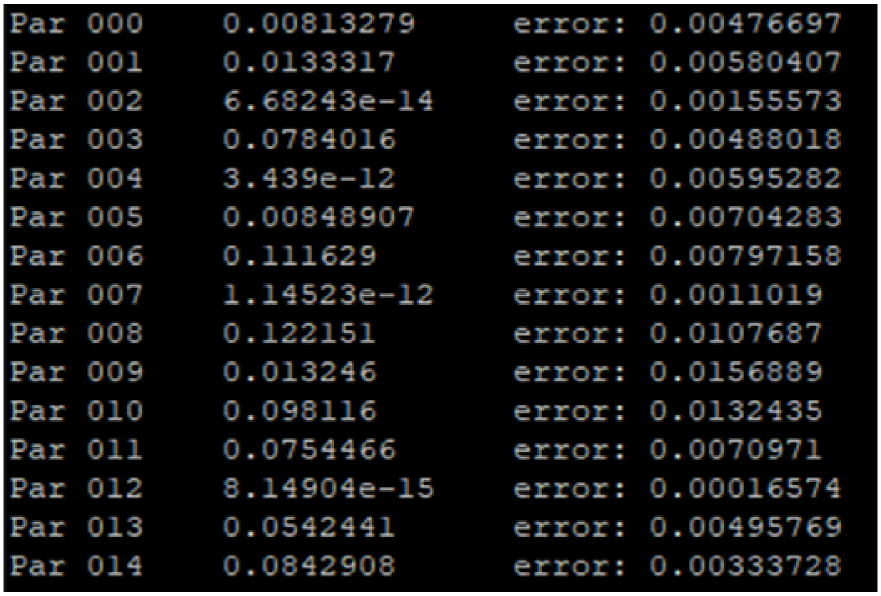

```
Par 000    0.00813279     error: 0.00476697
Par 001    0.0133317      error: 0.00580407
Par 002    6.68243e-14    error: 0.00155573
Par 003    0.0784016      error: 0.00488018
Par 004    3.439e-12      error: 0.00595282
Par 005    0.00848907     error: 0.00704283
Par 006    0.111629       error: 0.00797158
Par 007    1.14523e-12    error: 0.0011019
Par 008    0.122151       error: 0.0107687
Par 009    0.013246       error: 0.0156889
Par 010    0.098116       error: 0.0132435
Par 011    0.0754466      error: 0.0070971
Par 012    8.14904e-15    error: 0.00016574
Par 013    0.0542441      error: 0.00495769
Par 014    0.0842908      error: 0.00333728
```

Figure 5.9: Shows the feeding ratios for each of the entry state energies used in the simulation. There is one feeding ratio for each of the initial entry state energies used which are all summed to form the final spectra shown in Figure 5.8.

events in the simulation to get the simulated detector efficiency. This is the efficiency used to calculate the final values of this cross section measurement.

5.4 Uncertainties

The calculations for the efficiency and energy uncertainties are outlined in more detail in the following sections as they are more complex. Other uncertainties in the measurement come from the current measurements and the gas cell pressure whose uncertainties were defined by the detectors. The ammeter being used for this experiment has an uncertainty of 10^{-12}A and the experimental currents measured were on the order of 10^{-7}A making the beam current measurement uncertainties 0.001%. However, there are other systematic uncertainties from the beam current subtraction which is discussed in greater detail in Section 5.5. The noise in the ammeter was on the order a $10^{-15}A$. The pressure in the hydrogen gas cell was measured using a Baratron capacitance manometer with an accuracy of 0.5%. The measurement at an atmosphere for the pressure was approximately 10 Torr off from 760 Torr making the actual uncertainty around 1.5%.

Energy	Good Counts	Error	Empty Counts	Error	Sub Counts	Statistical Error
3.7	39416	198	17299	131	22116	238
3.4	9639	98	4242	65	5396	117
3.1	12973	113	7102	84	5870	141
2.8	4936	70	1841	42	2797	82

Table 5.2: Lists the statistical uncertainties from subtracting the spectra. The Good Counts are counts in the sum peak energy range, the empty counts are the same energy range for the gas cell without hydrogen gas and sub counts are the remaining statistics.

The statistical uncertainties are outlined in Table 5.2. The "Good Counts" are the number of counts in the sum peak energy range for each energy when the gas cell was full of hydrogen gas. The "Empty Counts" are the number of counts in the same energy range for the empty cell spectra. Those errors are $\sqrt{N}$ where N is the number of counts. The statistical error for the subtracted spectra are given by $\sqrt{(N_1^2 + N_2^2)}$ where N_i is the number of counts in the sum peak and the empty sum peak energy range, respectively.

5.4.1 Efficiency Uncertainty

The fitting procedure outlined in Section 5.3 was completed for each energy level and each level had twelve RAINIER input variations. Similar to the various inputs used with the ^{90}Zr$(p,\gamma)^{91}$Nb cross section, multiple inputs were considered for this calculation in order to gauge the uncertainty in the simulation process. The final input parameters used for the ^{84}Kr$(p,\gamma)^{85}$Rb reaction simulations are listed in Table 5.3.

The twelve different simulations for each energy were analyzed identically. χ^2 fits were performed for each and the feeding ratios are summed to calculate the simulated efficiency

Set Number	Level Density	E1 Model	Spin Cutoff
1	CTM	Standard Lorentzian	Single Particle
2	CTM	Standard Lorentzian	Rigid Sphere
3	CTM	KMF	Single Particle
4	CTM	KMF	Rigid Sphere
5	CTM	KOP	Single Particle
6	CTM	KOP	Rigid Sphere
7	BSFG	Standard Lorentzian	Single Particle
8	BSFG	Standard Lorentzian	Rigid Sphere
9	BSFG	KMF	Single Particle
10	BSFG	KMF	Rigid Sphere
11	BSFG	KOP	Single Particle
12	BSFG	KOP	Rigid Sphere

Table 5.3: Lists the RAINIER input parameters used for the simulations to calculate the efficiency of SuN and quantify the uncertainty in the simulation process.

of SuN for each input. The efficiency was calculated by taking the feeding ratio sum and multiplying by the number of events in the simulation. This efficiency was then used to calculate the cross sections with equation 5.5 for each set of inputs and averaged to find an uncertainty in the simulation and fitting processes. The average change in the final cross section was 2%.

An example for the 3.1 MeV beam energy is shown in Table 5.4. The simulations listed here correspond to the inputs shown in Table 5.3. Using the previously outlined procedure, each input is fit and the cross section calculated. The percent different is shown in the last column and comparing each to simulation 11. This input was chosen because it had the smallest χ^2 fit for the energy. The average percent difference for this energy is less than 1% and the largest percent difference for all of the fits was 5%.

Simulation	χ^2	Cross Section (mb)	Percent Difference
1	29	0.5600	1.28
2	27	0.5612	1.05
3	25	0.5544	2.27
4	23	0.5648	0.22
5	26	0.5590	1.45
6	21	0.5644	0.48
7	26	0.5631	0.72
8	26	0.5588	1.48
9	22	0.5711	0.69
10	22	0.5725	0.93
11	20	0.5672	0.00
12	20	0.5654	0.31
Average	24	0.5638	0.91

Table 5.4: Show the χ^2 and associated cross sections values for the 3.1 MeV energy for each RAINIER input listed in Table 5.3. The average for each value is also listed showing a percent difference calculated compared to Simulation 11 since it has the lowest χ^2 value.

5.4.2 Effective Energy

The energy uncertainty is based on the energy loss through the molybdenum foil, the energy straggling through the foil and the energy smearing from the Doppler shift although the former is the dominant factor. The cross section measurement calculated in this experiment has a range of entry state energies which are physically possible that correspond to the energy loss within the gas cell. Within this range the probability that the measured cross section came from a higher entry state energy is higher than measuring the reaction at a lower entry state energy because the cross section increases rapidly with increasing beam energy.

As the beam moves through the hydrogen gas target it is losing energy. Assuming a constant stopping power within the gas cell but with a varying cross section, the yield of the reaction is given by

$$Y(E_0) = \frac{1}{\epsilon(E_0)} \int_{E_0-\Delta E}^{E_0} \sigma(E) dE \tag{5.6}$$

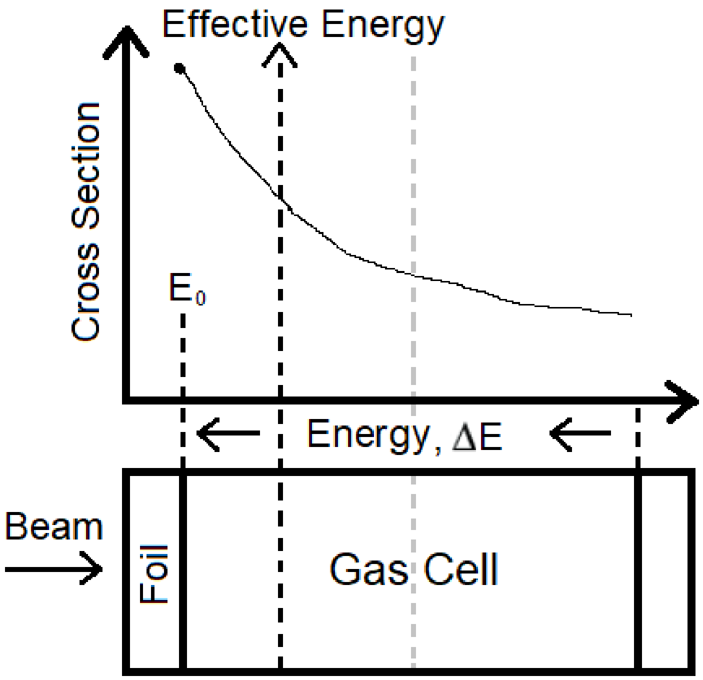

Figure 5.10: Shows a cartoon example of the beam energy loss and decreasing cross section. As the beam moves through the gas cell the energy is decreasing with the cross section. The effective energy is the point where the yield above and below that energy is the same.

where $Y(E_0)$ is the energy dependent yield, $\epsilon(E)$ is the energy dependent stopping power, E_0 is the initial beam energy and ΔE is the energy loss in the target. For instances where the cross section varies linearly in the energy range the previous equation can be rewritten as

$$Y(E_0) = \frac{\Delta E(E_0)}{\epsilon(E_0)}\sigma(E_{eff}) \tag{5.7}$$

where E_{eff} is the effective energy. The effective beam energy is the point at which the total yield is 50% the yield at E_0. Figure 5.10 shows a cartoon example of the cross section going through the gas cell. Moving from right to left, the energy begins at E_0 and decreases by a total of ΔE and the grey dashed line is the center of the gas cell. The effective energy is a good "average" energy to consider as the yield for this energy range above and below this point is the same. Notice that the effective energy is higher than the halfway through the gas cell but also lower than the initial energy E_0. This effective energy is calculated by

$$E_{eff} = E_0 - \Delta E + \Delta E \left[-\frac{\sigma_2}{\sigma_1 - \sigma_2} + \sqrt{\frac{\sigma_1^2 + \sigma_2^2}{2(\sigma_1 - \sigma_2)^2}} \right] \tag{5.8}$$

where $\sigma_1 = \sigma(E_0)$ and $\sigma_2 = \sigma(E_0 - \Delta E)$ [16].

Beam Energy (MeV)	After Foil (MeV)	After Cell (MeV)	ΔE (MeV)	E_{eff} (MeV)
3.7	3.096	2.529	0.567	2.895
3.4	2.791	2.231	0.560	2.597
3.1	2.487	1.921	0.566	2.295
2.8	2.288	1.653	0.565	2.054

Table 5.5: Shows the initial beam energy, the energy after the foil and gas cell, the energy loss and the effective energy. The measured cross section has a higher probability of coming from reactions at this calculated E_{eff}.

Table 5.5 shows the starting beam energy, the energy after the foil and after the gas cell, the total energy range of the gas cell and then the calculated effective energy using Equation 5.8. ΔE is the energy width of the gas cell and is linearly related to the position within the cell. The energy width of the gas cell ranges from the "After Foil" energy to the "After Gas Cell" energy and the beam could have interacted at any energy range within these limits. The effective energies listed in here are a low estimate for the energy where the yield is 50% of the "After Foil" energy. The cross section is varying linearly but it is a steep change for an energy range this wide. For this reason, the data is presented with the full energy range of the gas cell shown with the effective energy and the highest "After Foil" energies listed.

5.5 Results and Discussion

The final cross section results for the ^{84}Kr$(p,\gamma)^{85}$Rb reaction are shown in Figure 5.11. In blue are the TALYS calculations using the available nuclear level densities and γ-ray strength functions and the NON-SMOKER values are shown in brown. NON-SMOKER and TALYS are theoretical Hauser-Fesbach statistical model codes for cross sections and reaction rates [33] [59]. TALYS was run with every various level density and γ-ray strength function variation to create the theoretical uncertainty band for the cross section. At higher energies TALYS has an uncertainty of approximately a factor of 10.

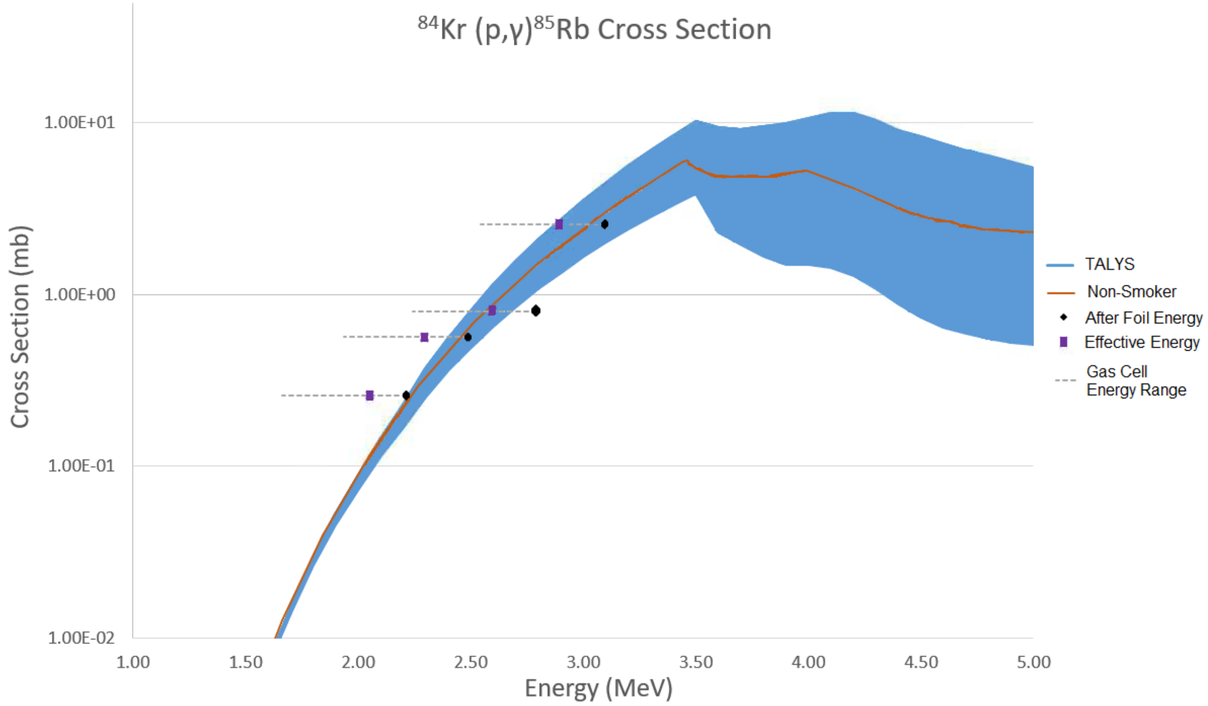

Figure 5.11: Shows the final cross sections and their uncertainties in black measured at the energy after the foil and the purple squares measured at the effective emergy compared to TALYS in blue and the NON-SMOKER theoretical values in brown [59].

The results of the present work are shown in black for the energy after going through the foil and the purple squares are the effective energies calculated in Section 5.4.2. The black line represents the energy width of the gas cell. The energy range lower than the effective energies consist of 50% of the expected yield for that beam energy. The measured cross sections in this work are higher than the theoretical predictions.

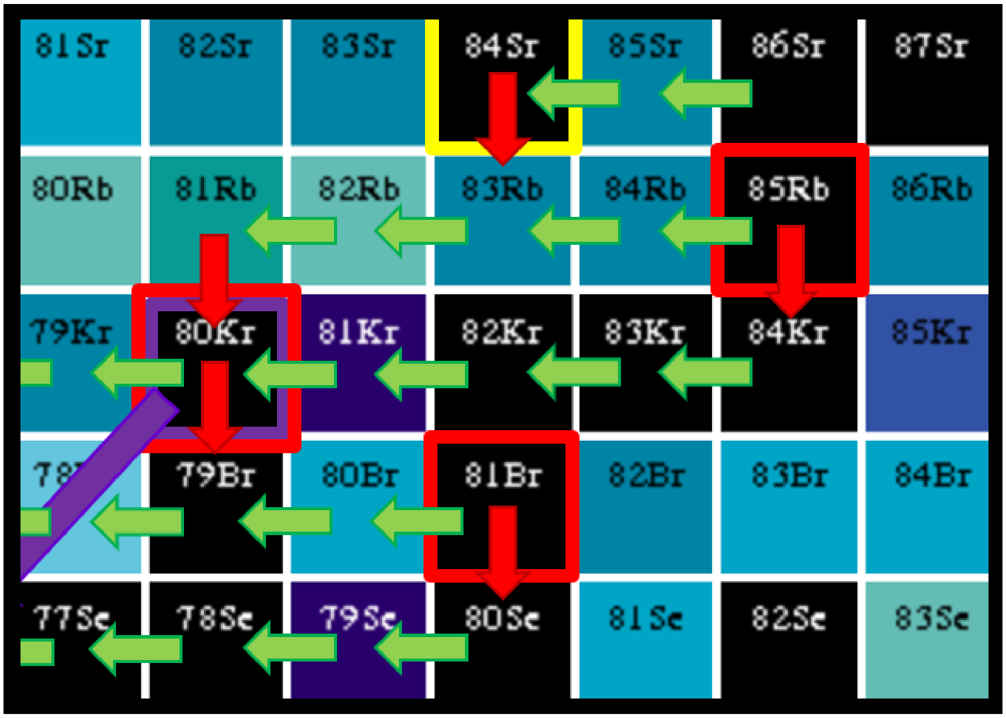

Figure 5.12: Examples for the p process reaction network with a series of (γ, n) (green arrows), (γ, p) (red arrows) and (γ, α) (purple arrow) reactions. The red boxes and purple boxes and branching points, the yellow box is a p nuclei.

Looking back at the chart of the nuclei zoomed into this mass region, Figure 5.12 shows the reaction flow around the ^{84}Kr$(p, \gamma)^{85}$Rb reaction. The green arrows are the dominating (γ, n) reactions, the red arrows are the (γ, p) reactions and the purple arrow is a (γ, α) reaction. Recall that ^{85}Rb was marked as a branching point between the (γ, n) and (γ, p) reaction flow. If the cross sections for the ^{84}Kr$(p, \gamma)^{85}$Rb reaction are higher than theory, as is shown with this measurement, the reaction network would flow through the (γ, p) reaction instead of the (γ, n). Therefor the path to the p-nucleus, ^{78}Kr, should go through the krypton chain instead of the rubidium chain.

5.6 Conclusions and Future Plans

The ^{84}Kr$(p,\gamma)^{85}$Rb cross section was directly measured for the first time using the SuN detector in inverse kinematics. This reaction will help to constrain theory in the mass region and helps to define the direction of the reaction flow within this energy region for the p process. A new hydrogen gas cell target was designed and tested for this experiment as well as a new efficiency analysis technique. This technique was validated with the previously published ^{90}Zr$(p,\gamma)^{91}$Nb cross section measured with SuN [46]. The ^{82}Kr$(p,\gamma)^{83}$Rb data must also be analyzed in the future for a more comprehensive examination of this reaction chain which feeds the creation of the ^{78}Kr p nucleus.

A new experiment using this technique was proposed and accepted for the ReA PAC proposal to directly measure the ^{73}As$(p,\gamma)^{74}$Se cross section. This will be the first direct radioactive measurement for the p process and directly effects the abundance of the lightest p nuclei, ^{74}Se. Some updates to the current experimental setup would be useful before running the next experiment. Parameterizing the micro channel plate (MCP) detector designed at Notre Dame and using it to measure the beam current upstream from SuN will be important for a radioactive beam experiment with lower currents. It is a grid MCP designed for a high transmission rate and was tested during the initial phases of this work but not used for the current readings. The empty cell spectra are scaled based on the beam current deposited into the setup for the full cell runs. If this scaling is incorrect it would alter the final spectra. The beam readings could be taken at faster intervals which would reduce the need to average the measurements and the MCP would provide a continuous measurement of beam entering the setup.

The measurements here match well with theory but the data points measured are consistently higher than theory. This could suggests that there are systematic uncertainties that need to be addressed before running future experiments. Some of the systematic experimental uncertainties could be coming from the current measurement, the empty cell subtraction, how the beam interacts with the gas cell and how much of the beam makes it into the cell. Instead of running with the cell empty for these measurements using an inert gas should be considered. This will mimic the scattering of the beam off the gas within the cell but still produce no background within the sum peak energy range of interest. The beam will not react the same in an empty cell as with a cell filled with gas and it should be explored more in order to quantify this.

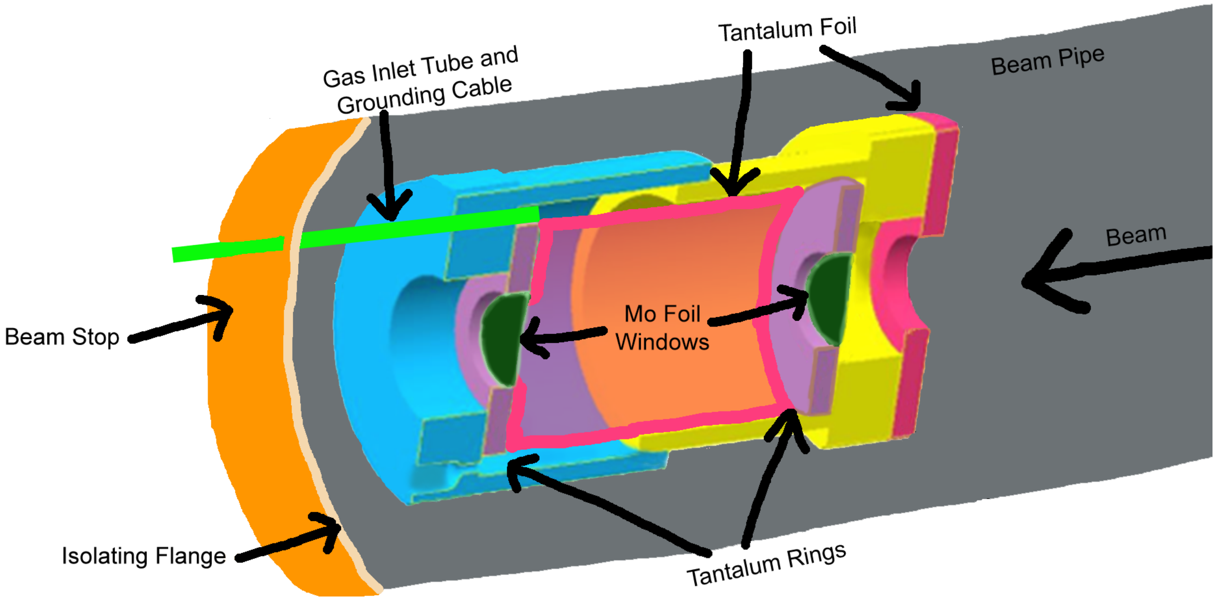

Figure 5.13: Figure shows the inside of the gas cell and the beam pipe in more detail to highlight the electrical connections. Gray is the beam pipe, orange is the back beam stop, light orange is the isolating flange, light green is the gas inlet tube and the grounding cable, blue and yellow are the plastic cell halves, purple are the Ta rings, dark green are the Mo foil windows and pink is the Ta foil.

Figure 5.13 shows a schematic of the inside of the gas cell and the beam-current integration. There were current readings on the beam stop, shown in orange, and directly from the beam pipe, shown in grey. The beam pipe and the back flange were electrically isolated from each other with the gas inlet tube, shown in light green, connecting the inside of the gas cell and the beam stop. The gas inlet tube was touching Ta foil inside of the gas cell, shown in pink, which connected the front and back Ta rings, shown in purple, and the Mo foil windows, shown in dark green. The Ta foil on the front face of the cell was touching the beam pipe and current hitting that foil would be recorded on the beam pipe readings. The front Ta foil is also the only part of the gas cell which will be read out on the beam pipe and any current hitting the Mo foil windows or the Ta rings will be measured off the beam stop. Therefor, current measured from the beam stop should have made it through the gas cell after interacting with the gas. However, if the beam drifted and hit the tantalum ring that the molybdenum foil was glued to those beam particles would not make it into the gas cell. This could prove to be a systematic uncertainty for this measurement. Even though there was a collimator upstream of SuN which should keep the beam alligned, there is still a chance it could drift onto the Ta rings.

Updating the gas cell design would be useful to help both with the current and beam transmission but also with the large energy width of the cell. Using a thinner gas cell would provide a lower density of interacting particles but would have a thinner energy window. However, if the molybdenum foil window diameter was reduced the same foil thickness should be able to hold more pressure allowing for a thinner cell with the same density of interacting particles. When redesigning a new cell, finding a way to read current off of the front face of the cell independently of the beam pipe or back flange would be very useful for identifying when the beam drifts and is not going through the foil window. This could allow for more accurate beam measurements and subsequently a more accurate background subtraction. A gas cell made of a different material other than plastic could also be useful. Aluminum was considered as an alternate option originally, however the thicker material can lead to a lower transmission of γ-rays into SuN which would negatively effect the efficiency.

BIBLIOGRAPHY

BIBLIOGRAPHY

[1] https://www.nasa.gov/, “National aeronautics and space administration.”

[2] E. Jochen and N. Birge and M. Kortelainen and et al., “The limits of the nuclear landscape,” *Nature*, vol. 486, p. 509, 2012.

[3] http://www.nndc.bnl.gov/, “National nuclear data center.”

[4] M. Goeppert-Mayer, “On closed shells in nuclei. ii,” *Physical Review*, vol. 75, p. 1969, 1949.

[5] C. Illiadis, *Nuclear Physics of Stars.* Wiley-VCH Verlag GmbH and Co., 2007.

[6] K.J.R. Rosman and P.D.P. Taylor, “Isotopic compositions of the elements 1997,” *Pure and Applied Chemistry*, vol. 70, pp. 217–235, 1998.

[7] K. Lodders, “Solar system abundances and codensation temperatures of the elements,” *The Astrophysical Journal*, vol. 591, pp. 1220–1247.

[8] E. Vangioni-Flem, M. Casse, and J. Audouze, “Lithium-beryllium-boron: Origin and evolution,” *Physical Reports*, vol. 333, pp. 365–387, 2000.

[9] E. M. Burbidge, G. R. Burbidge, W. A. Fowler, and F. Hoyle, “Synthesis of the elements in stars,” *Reviews of Modern Physics*, vol. 29, pp. 547–650, 1957.

[10] A.G.W. Cameron, “Nuclear reactions in stars and nucleogenesis,” *The Astronomical Society of the Pacific*, vol. 69, p. 201, 1957.

[11] M. Arnould and S. Goriely, “The p-process of stellar nucleosynthesis: Astrophysics and nuclear physics status,” *Physics Reports*, vol. 384, pp. 1–84, 2003.

[12] C.F. von Weizsäcker *Phys. Z.*, vol. 38, p. 176, 1937.

[13] R. A. Alpher, H. A. Bethe, and G. Gamow, “The origin of chemical elements,” *Phys. Rev.*, vol. 73, p. 803, 1948.

[14] G. Steigman, “Primordial nucleosynthesis in the precision cosmology era,” *Annual Review of Nuclear and Particle Science*, vol. 57, pp. 463–491, 2007.

[15] P.D. Parker and J.N. Bahcall and W.A. Fowler, “Termination of the proton-proton chain in stellar interiors,” *Astrophysical Journal*, vol. 139, p. 602, 1964.

[16] C. E. Rolfs and W. S. Rodney, *Cauldrons in the Cosmos: Nuclear Astrophysics.* The University of Chicago Press, 1988.

[17] S. Quinn, *Capture Cross Sections For The Astrophysical P Process.* PhD thesis, Michigan State University, 2015.

[18] F. Käppeler and R. Gallino and S. Bisterzo and W. Aoki, "The s process: Nuclear physics, stellar models, and observations," *Rev. Mod. Phys.*, vol. 83, p. 157, 2011.

[19] M. Arnould, S.Goriely, and K. Takahashi, "The r-process of stellar nucleosynthesis: Astrophysics and nuclear physics achievements and mysteries," *Physics Reports*, vol. 450, pp. 97–213, 2007.

[20] D. Kasen and B. Metzger and J. Barnes and E. Quataert and E. Ramirez-Ruiz, "Origin of the heavy elements in binary neutron-star mergers from a gravitational wave event," *Nature*, vol. 551, p. 80, 2017.

[21] J.J. Cowan and W.K. Rose, "Production of ^{14}c and neutrons in red giants," *Astrophysical Journal*, vol. 212, pp. 149–158, 1977.

[22] C. Travaglio and F. K. Röpke and R. Gallino and W. Hillebrandt, "Type ia supernovae as sites of p-process: Two-dimensional models coupled to nucleosynthesis," *The Astrophysical Journal*, vol. 739, 2011.

[23] S. Woosley, "The p-process in supernovae," *The Astrophysical Journal Supplement Series*, vol. 36, p. 20, 1978.

[24] T. Rauscher, A. Heger, R. Hoffman, and S. Woosley, "Nucleosynthesis in massive stars with improved nuclear and stellar physics," *The Astrophysical Journal*, vol. 576, pp. 323–348, 2002.

[25] C. Travaglio and F. K. Röpke and R. Gallino and W. Hillebrandt, "Testing the role of sne ia for galactic chemical evolution of p-nuclei with two-dimensional models and with s-process seeds at different metallicities," *The Astrophysical Journal*, vol. 799, 2015.

[26] M. Rayet, M. Arnould, M. Hashimoto, N. Prantzos, and K. Nomoto, "The p-process in type ii supernovae," *Astronomy and Astrophysics*, vol. 298, pp. 517–527, 1995.

[27] W. Rapp, J. Gorres, M. Wiescher, and et al., "Sensitivity of p-process nucleosynthesis to nuclear reaction rates in a 25m$ødot$ supernova model," *The Astrophysical Journal*, vol. 653, pp. 474–489, 2006.

[28] T. Rauscher, "Branchings in the γ process path revisited," *Physical Review C*, vol. 73, 2006.

[29] F. W. Aston, "Isotopes and atomic weights," *Nature*, vol. 105, p. 617, 1920.

[30] A. Einstein *Annalen der Physik*, vol. 323, p. 639, 1905.

[31] M. Wang, G. Audi, A. Wapstra, and et al., "The ame2012 atomic mass evaluation," *Chinese Physics C*, vol. 36, p. 1603, 2012.

[32] C. Angulo, M. Arnould, M. Rayet, and et. al., "A compilation of charged-particle induced thermonuclear reaction rates," *Nuclear Physics A*, vol. 656, pp. 3–183, 1999.

[33] T. Rauscher and F. Thielemann, "Astrophysical reaction rates from statistical model calculations," *Atomic Data and Nuclear Data Tables*, vol. 75, pp. 1–351, 2000.

[34] N. Nohr, "Neutron capture and nuclear constitution," *Nature*, pp. 137–344, 1936.

[35] T. Rauscher, *Essentials of Nucleosynthesis and Theoretical Nuclear Astrophysics.* IOP Publishing, Bristol, UK, 2020.

[36] W. Hauser and H. Feshbach, "The inelastic scattering of neutrons," *Physical Review*, vol. 87, p. 366, 1952.

[37] H. Utsunomiya, P. Mohr, A. Zilges, and M. Rayet, "Direct determination of photodisintegration cross sections and the p-process," *Nuclear Physics A*, vol. 777, pp. 459–478.

[38] J. Blatt and V. Weisskopf, *Theoretical Nuclear Physics.* Wiley, New York, 1952.

[39] A. Messiah, *Quantum Mechanics.* New York, 1999.

[40] R.A. Ward and W.A. Fowler *Astrophysics J*, vol. 238, p. 266, 1980.

[41] T. Rauscher, "The path to improved reaction rates for astrophysics," *International Journal of Modern Physics E*, vol. 20, pp. 0–11, 2011.

[42] A. Simon and S.J. Quinn and A. Spyrou and et. al., "Sun: Summing nai(ti) gamma-ray detector for capture reaction measurements," *Nuclear Instruments and Methods in Physics Research A*, vol. 703, pp. 16–21, 2013.

[43] E. Klopfer and J. Brett and P.A. DeYoung and et al., "Sunscreen: A cosmic-ray veto detector for capture-reaction measurements," *Nuclear Instruments and Methods in Physics Research A*, vol. 788, pp. 5–8, 2015.

[44] A. Lapierre, S. Schwarz, and et. al., "Commissioning results of the rea ebit charge breeder at the nscl: First reacceleration of stable-isotope beams," *Nuclear Instruments and Methods in Physics Research Section B: Beam Interactions with Materials and Atoms*, vol. 317, pp. 399–401, 2013.

[45] F. Naqvi, S. Quinn, A. Spyrou, and et al., “Proton capture cross section of ^{72}ge and astrophysical implications,” *Phys. Rev. C*, vol. 92, p. 025804, 2015.

[46] A. Spyrou, S. Quinn, A. Simon, T. Rauscher, and et al., “Measurement of the ^{90,92}zr$(p,\gamma)^{91,93}$nb reactions for the nucleosynthesis of elements near $a = 90$,” *Phys. Rev. C*, vol. 88, p. 045802, 2013.

[47] A. Dombos, D. Fang, A. Spyrou, and et al., “Total absorption spectroscopy of the β decay of ^{76}ga,” *Phys. Rev. C*, vol. 93, p. 064317, 2016.

[48] S.J. Quinn and A.Spyrou and et. al., “First application of the γ-summing technique in inverse kinematics,” *Nuclear Instruments and Methods in Physics Research A*, vol. 757, pp. 62–66, 2014.

[49] A. Simon, M. Beard, A. Spyrou, and et al., “Systematic study of (α,γ) reactions for stable nickel isotopes,” *Phys. Rev. C*, vol. 92, p. 025806, 2015.

[50] A. Spyrou, S. Liddick, A. Larson, and et al., “Novel technique for constraining r-process (n,γ) reaction rates,” *Physical Review Letters*, vol. 113, p. 232502, 2014.

[51] A. Spyrou, J. Becker, and et al., “Cross-section measurements of capture reactions relevant to the p process using a 4π γ-summing method,” *Phys. Rev. C*, vol. 76, p. 015802, 2007.

[52] S. Harissopulos, E. Skreti, P. Tsagari, and et. al., “Cross section measurements of the ^{93}Nb$(p,\gamma)^{94}$Mo reaction at $E_p = 1.4 - -4.9$MeV relevant to the nucleosynthetic p process,” *Phys. Rev. C*, vol. 64, p. 055804, 2001.

[53] A. Simon, J. Fallis, A. Spyrou, and et. al., “Radiative capture reactions with heavy beams: extending the capabilities of dragon,” *The European Physics Journal A*, pp. 49–60, 2013.

[54] B. Mei and et al., “First measurement of the ^{96}Ru$(p,\gamma)^{97}$Rh cross section for the p process with a storage ring,” *Phys. Rev. C*, vol. 92, p. 035803, 2015.

[55] L. Kirsch and L. Berstein, “Rainier: A simulation tool for distributions of excited nuclear states and cascade fluctuations,” *Nuclear Instruments and Methods in Physics Research Section A: Accelerators, Spectrometers, Detectors and Associated Equipment*, vol. 892, pp. 30–40, 2018.

[56] S. Agostinelli, J. Allison, and et al., “Geant4 — a simulation toolkit,” *Astronomy and Astrophysics*, vol. 506, pp. 250–303, 2003.

[57] A. Gilbert and A. Cameron, “A composite nuclear-level density formula with shell corrections,” *Canadian Journal of Physics*, vol. 43:8, 1965.

[58] W. Dilg, W. Schantl, H. Vonach, and M. Uhl, "Level density parameters for the back-shifted fermi gas model in the mass range 40 ¡ a ¡ 250," *Nuclear Physics A*, vol. 217, pp. 269–298, 1973.

[59] S. G. A. Koning, S. Hilaire, *TALYS-1.8: A nuclear reaction program*, 1st ed., 2015.

[60] D. Brink, "Individual particle and collective aspects of the nuclear photoeffect," *Nuclear Physics*, vol. 4, pp. 215–220, 1957.

[61] P. Axel, "Electric dipole ground-state transition width strength function and 7-mev photon interactions," *Phys. Rev.*, vol. 126, pp. 671–683, 1962.

[62] J. Kopecky and M. Uhl, "Test of gamma-ray strength functions in nuclear reaction model calculations," *Physical Review C*, vol. 41, pp. 1941–1955, 1990.

[63] V. F. S.G. Kadmenskij, V.P. Markushev, "Radiative widths of neutron resonances and giant dipole resonances," *Yad. Fiz.; (USSR)*, vol. 37:2, pp. 277–283, 1983.

[64] A. C. Larsen and et. al., "Enhanced low-energy γ-decay strength of ^{70}ni and its robustness within the shell model," *Physical Review C*, vol. 97, p. 054329, 2018.

[65] C. Laird, D. Flynn, R. Hershberger, and F. Gabbard, "Proton-90zr interaction at sub-coulomb proton energies," *Physical Review C*, vol. 35, p. 1265, 1987.